NON-PHOTONIC ELECTRON PRODUCTION IN PROTON-PROTON AND GOLD-GOLD COLLISIONS AT $\sqrt{s}$ = 200 GEV

A Dissertation

Submitted to the Faculty

of

Purdue University

by

Xin Li

In Partial Fulfillment of the

Requirements for the Degree

of

Doctor of Philosophy

May 2013

Purdue University

West Lafayette, Indiana

TABLE OF CONTENTS

LIST OF TABLES

Table Page

LIST OF FIGURES

Figure Page

Figure Page

Figure Page

Figure Page

Figure Page

Figure Page

Figure Page

ABSTRACT

Li, Xin. Ph.D., Purdue University, May 2013. Non-phototnic Electron Production in Proton-Proton and Gold-Gold Collisions at $\sqrt{s} = 200$ GeV . Major Professor: Wei Xie.

The focus of this thesis work is on studying the production of electrons from heavy flavor decays, i.e. non-photonic electrons, at both high p_T and low p_T in *p+p* collisions. The outcome of this work resolved the long standing discrepancy between STAR and PHENIX measurements and thus had a large impact in understanding the interactions between heavy quarks and the Quark Gluon Plasma produced in relativistic heavy-ion collisions.

Nuclear and particle physics aims to understand nature in terms of the most fundamental ingredients and interactions. The most fundamental ingredients, so called elementary particles, include spin 1/2 fermions, which are the constituents of matter, and spin 1 gauge bosons, which are the force carriers. Except gravity, the other three most fundamental interactions can be well understood by quantum field theories. Quantum Chromo-dynamics (QCD), based on the SU (3) group, is the theory of the strong interactions of colored quarks and gluons. At high temperature or high energy

density, the interaction between partons was expected to be significantly weakened enabling them to move around like a free gas and no longer confined inside the hadrons. This state of matter with de-confined partons is named as “Quark Gluon Plasma” (QGP) in analogy to the conventional plasma in atomic physics.

The Relativistic Heavy Ion Collider (RHIC) [1] was designed to collide all species of nucleus at high energy to produce QGP and study its property using a wide range of probes. Since it began operating in year 2000, RHIC has done systematic studies on a broad range of physics probes and discovered a new state of medium with unprecedented temperature and density. The properties of the new medium created at RHIC are more complicated than had been anticipated. It has very high density (~5GeV/fm^3) and very high temperature (150- 180MeV), which is well above the predicted QCD threshold for the occurrence of de-confinement. However, instead of behaving like a free gas, the observed large hadron elliptic flow suggests it is more like a “perfect fluid” with the ratio of viscosity to entropy close to the quantum limit [2] Clearly the goal of future RHIC physics programs should focus on the detailed studies of the hot and dense matter to clarify its properties.

Heavy quarks (charm and bottom) are rare probes and have not been studied in detail at RHIC. They are produced early in the collisions and interact with the medium very differently from light quarks because of their large mass. Therefore studying heavy quark production would provide crucial opportunities to reveal new properties of the

medium. Heavy flavor hadrons were thought to be less suppressed due to their heavy mass. However, it was found by both the PHENIX and STAR experiments in 2005 that the production rate of non-photonic electrons was as strongly suppressed as the light hadrons [3]. This observation posed a serious challenge to our theoretical understanding heavy quark energy loss in QGP and triggered concerted efforts in the field to investigate novel energy loss mechanisms. Although the STAR and PHENIX measurements of the non-photonic electron nuclear modification factor were consistent, the measured production rate by STAR was, however, twice that measured by PHENIX in both proton-proton (*p+p*) and gold-gold (Au+Au) collisions. This discrepancy had essentially halted further progress in the understanding of heavy flavor energy loss in QGP.

This thesis presents analysis details in identifying and measuring non-photonic electrons with data recorded during the 2008 and 2009 *p+p* runs at $\sqrt{s}$ = 200GeV. This work leads to the resolution of the STAR and PHENIX discrepancy and thus had a large impact in understanding the heavy quark production in QGP. The STAR non-photonic electron invariant cross sections in *p+p* collisions can be described by the Fixed-Order Next-to-Leading Logarithm (FONLL) perturbative QCD (pQCD) calculation [4] within its theoretical uncertainties. The measurement of the nuclear modification factor in Au+Au collisions shows a strong suppression in non-photonic electron production at high p_T and challenge the understanding of heavy quark energy loss mechanism in the field.

1. INTRODUCTION

1.1 Heavy Quark as Probes for Quark Gluon Plasma

Quarks are the fundamental building blocks of hadrons like protons and neutrons. There are six favors of quarks, namely up (u), down (d), charm(c), strange (s), bottom (b) and top (t) as listed in the left panel of Figure 1.1. Heavy quarks at RHIC are referred to the charm and bottom quarks. In the early 1980s, QCD calculations showed that the high temperature (T > Tc, where Tc=150MeV) or high energy density (E>1GeV/fm^3) environment would dramatically weaken the interaction between quarks and gluons enabling them to move around freely and no longer confined inside the hadrons. This state of matter with deconfined quarks and gluons is named as "Quark Gluon Plasma" (QGP). According to QCD prediction, when heavy ions collide in very high energy, QGP phase might be created. The QGP state can be reached in two ways as shown in the right panel of Figure 1.1. One is to increase the net baryon density. Neutron star is similar in this situation, and QGP might exist in the core of neutron stars. The other way is to increase the temperature to the level in our early universe when T > Tc.

The relativistic heavy-ion collider (RHIC) at Brookhaven national lab (BNL) can collides different species of heavy-ions with top energy at $\sqrt{s}$=200 GeV. In relativistic heavy ion

collisions at RHIC, a huge amount of energy is deposited into a small volume to create an energy density and temperature high enough to reach or go beyond the critical value, a new medium with more complicated properties than anticipated is created. It behaves more like a “perfect fluid” with extremely small ratio of viscosity over entropy that is close to the quantum limit. And many of the bound states, for example, the J/ψ, might still survive [5].

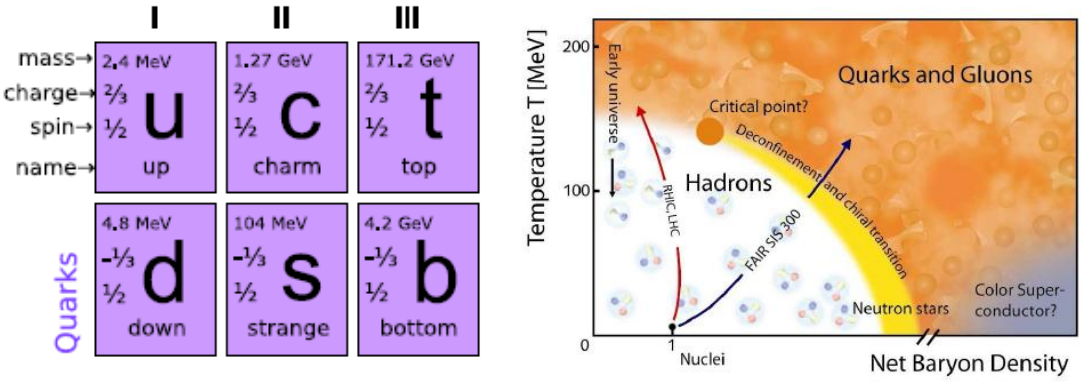

Figure 1.1 (left) Quarks and their properties. (right). Schematics of QCD phase diagram.

To study the hot and dense medium created at RHIC and clarify its properties, one major probe is heavy quark. Heavy quarks reveal themselves in two different forms: open heavy flavor mesons consisting of a heavy and light quark-antiquark pair, and heavy quarkonium consisting of a heavy quark and its antiquark. Many reasons make heavy flavor measurements unique. Because of their large mass, heavy quarks interact with the QGP medium very differently than the light quarks. Detailed and accurate studies of heavy flavor particles can offer information about the QGP that cannot be obtained by

studying the behavior of light quarks. The creation of heavy quarks requires much more energy compared to the creation of the nearly massless light quarks. For this reason, heavy quarks are produced at the earliest stage of the collision before the incident nuclei have passed each other and the light quarks and gluons are produced. Therefore, the production rate and distributions of heavy flavor particles reflect the properties of the QGP medium in the early stage of its evolution. Heavy quarks are expected to lose less energy compared to the light quarks when propagating through the QGP medium, so their abundance should be less suppressed at a given transverse momentum in comparison to light quarks. Heavy quarks are rarely produced compared to the copiously produced light quarks in heavy-ion collisions. The produced heavy quarks will most likely combine with light quarks to form open heavy flavor mesons. Hence, a large suppression of heavy quarkonium (doublet of a heavy quark and its antiquark) production, e.g. the J/ψ particle (a charm-anticharm pair), was considered as a "smoking gun" signal for the QGP formation [6]. Heavy quarks are not expected to flow together with the "perfect fluid" of light quarks. Observation of a large heavy flavor flow would be an indication of their strong interactions with the QGP. The richness of the heavy quark meson states allows their production in various mass and binding energy scales. Different states are expected to dissolve in the QGP at different temperatures, thus providing an experimental thermometer of the QGP.

Furthermore, in order to study the hot and dense QGP medium effect, we need to understand the heavy quark production in the elementary *p+p* collisions which serves as one of the critical references.

1.2 Early STAR Measurements of Heavy Quark Production at RHIC

Open heavy flavor production can be studied directly by reconstructing charm and bottom hadrons through their hadronic decays or indirectly by measuring leptons from charm and bottom hadron decays, i.e. non-photonic electrons. The lepton measurements, while providing only indirect access to the parent heavy quark kinematics, are more advantageous because of their higher branching ratio from heavy flavor decays and their capability for fast online triggers that extends the measurements to high transverse momentum (p_T). Currently at RHIC, the non-photonic electron is the major approach to study the heavy quark. The measurements from direct heavy flavor meson reconstruction suffer from the large background which can be significantly removed from rejecting small impact parameter tracks. It will become the main approach when the heavy flavor tracker silicon detector upgrade [7] is accomplished in 2014.

In heavy-ion collisions at RHIC, one of the critical observations to support the discovery of the new medium at RHIC is the strong suppression of high p_T hadron production [8]. This is understood to arise from the energy loss caused mainly by gluon bremsstrahlung

radiation during the propagation of light quarks in the dense medium. Theoretical calculations predicted that the energy loss of heavy quarks [9] is much smaller compared to that of light quarks, since its much larger mass leads to much smaller acceleration and therefore smaller radiation. However, the measurements on single electrons from non-photonic electron measurement in both PHENIX and STAR experiments observed strong suppression of high p_T heavy quark productions.

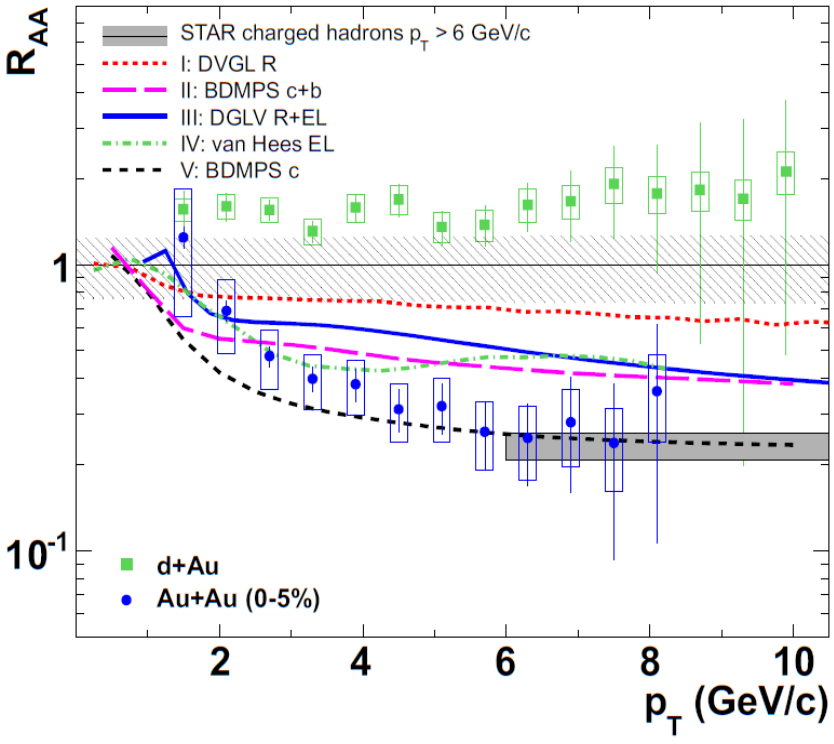

Figure 1.2 Early STAR measurements of non-photonic electron nuclear modification factor R_{AA} as a function of p_T in *d*+Au (green closed circles) and the most central 5% Au+Au collisions (blue closed circles) at 200 GeV using Run-2003 data. The error bars (boxes) are statistical (systematic) uncertainties. The shaded area at R_{AA}=1 represents the normalization uncertainty common to all data points. The band at R_{AA}~0.2 represents the STAR charged hadron measurement at p_T > 6 GeV/*c*. Various curves represent predictions from various models.

Figure 1.2 shows the STAR measurement of nuclear modification factor as a function of transverse momentum (p_T). RAA is defined as $R_{AA} = \frac{Yield\ (Au+Au)}{Ncoll \cdot yield(p+p)}$, where yield(Au+Au) and yield (*p+p*) is the yield in Au+Au and *p+p* collisions, respectively; Ncoll is the number of nucleon-nucleon collisions in a single Au+Au collisions. For hard probes, since nucleon-nucleon collisions are well separated from each other in space-time, if nothing interesting happens, RAA will be equal to one. On the other hand, if RAA is smaller or larger than one, it will provide information for interaction between the probes and the medium. The dotted line in the figure is the theory predictions based on only the radiative energy loss in the gluon density of 1000 [10] which can describe the light charged hadron modification factor very well. One can see it significantly underestimates the suppression. Results from the two experiments are consistent with each other. It is also interesting that the large suppression extends to very high p_T where contribution from bottom quark is expected to be dominant.

Although the STAR and PHENIX measurements of the non-photonic electron nuclear modification factor were consistent, the measured production rate by STAR was, however, twice that measured by PHENIX in both proton-proton (*p+p*) and gold-gold (Au+Au) collisions. The STAR *p+p* measurement was approximately two times the upper bound prediction of the fixed-order-next-to-leading-log (FONLL) perturbative QCD (pQCD) calculation while the PHENIX measurement is consistent with it as shown in Figure 1.3. This caused serious concerns whether or not pQCD can describe heavy quark

production in elementary *p+p* interactions at RHIC, and called the non-photonic electron suppression measurements into question. This discrepancy between STAR and PHENIX had been discussed in many conferences, had caused great confusion, and had essentially halted further progress in the understanding of heavy flavor energy loss in QGP as well as the interpretation of other important measurements such as those of heavy quarkonia production.

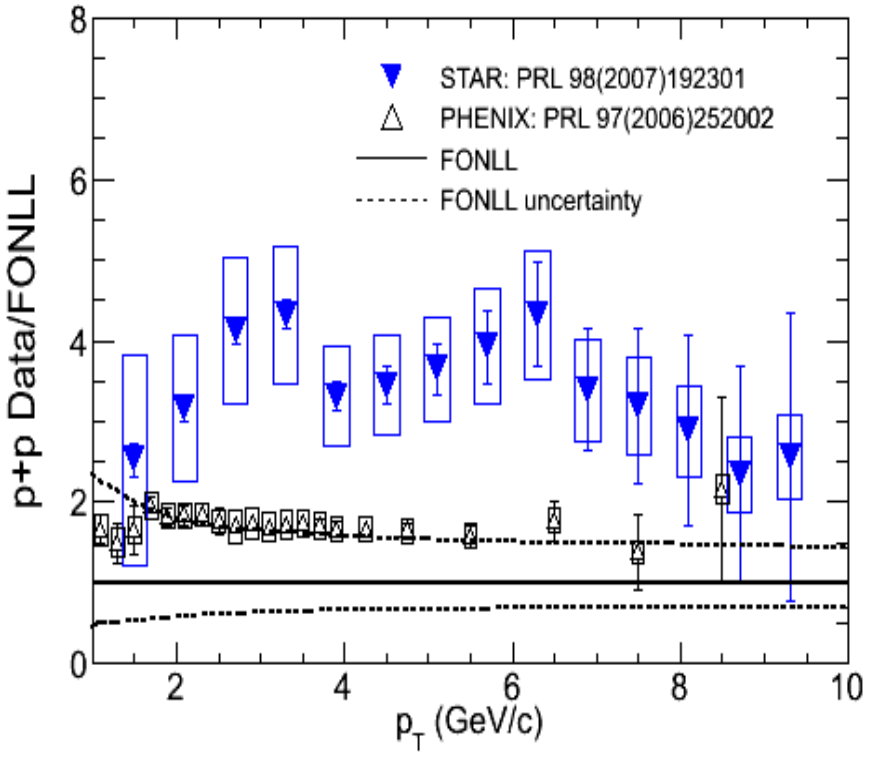

Figure 1.3 Ratio of the early STAR measurements of non-photonic electron production rate from Run-2003 data to pQCD fixed-order-next-to-leading-log (FONLL) prediction (dashed lines are theoretical uncertainties) as a function of p_T (blue triangles) together with the PHENIX results (black triangles). The error bars (boxes) are statistical (systematic) uncertainties.

In this thesis, we present the details of measuring non-photonic electron production in *p+p* collisions at √s=200 GeV using high quality new data recorded during Run2008 for

high p_T (p_T > 2 GeV/c) and run 2009 for low p_T in the STAR experiment at RHIC. The high p_T result is cross checked and later on combined with an independent measurement using Run2005 data for a publication in Physical Review D [11]. The major background of this analysis is from π^0 dalitz decay which has a branching ratio of ~1.2% and γ conversions which has a probability of 7/9*Radiation Length. The majority of the material budget was from the silicon drift detector in STAR detector system before Run2008. In order to significantly reduce the background to resolve the STAR and PHENIX discrepancy, STAR removed the silicon detector during Run2008. This leads to a reduction of material thickness of about a factor of ten and improves the signal-to-background ratio by about a factor of five for non-photonic electron measurements. Despite the large difference in background levels due to the different detector configurations, measured cross-sections from Run2008 and Run2005 are consistent with each other and can be described by the FONLL pQCD calculations.

This work also uncovered an error in the previously published STAR results in *p+p*, *d*+Au and Au+Au and thus completely resolved the long standing discrepancy between STAR and PHENIX measurements. This error overestimated the background finding efficiency by about 10% resulting in a factor two difference in the calculated cross section. The measured R_{AA} after correcting the error indicate a strong suppression of heavy quark of heavy quark production in Au+Au collisions at RHIC. An erratum summarizing these findings was published in Physical Review Letters [12].

2. THE STAR EXPERIMENT AT RHIC

The Relativistic Heavy Ion Collider (RHIC) at Brookhaven National Laboratory (BNL) is a world-class scientific research facility that began operation in 2000, following 10 years of development and construction. It can collide protons up to 500 GeV and various species of heavy ions up to 200 GeV in the center of mass system. The Solenoid Tracker at RHIC (STAR) is a detector system that consists of several subsystems. It is located at the 6 o'clock position on the RHIC ring as shown in Figure 2.1. It has 2π coverage in azimuthal angle and ± 1.5 in pseudorapidity coverage. In the analyses for this thesis, information from six major detectors is used: Time Projection Chamber (TPC), Barrel Electro-Magnetic Calorimeter (BEMC), Barrel Shower Maximum Detector (BSMD), Time of Flight detector (TOF), Beam-Beam Counter (BBC) and Vertex Position Detector (VPD).

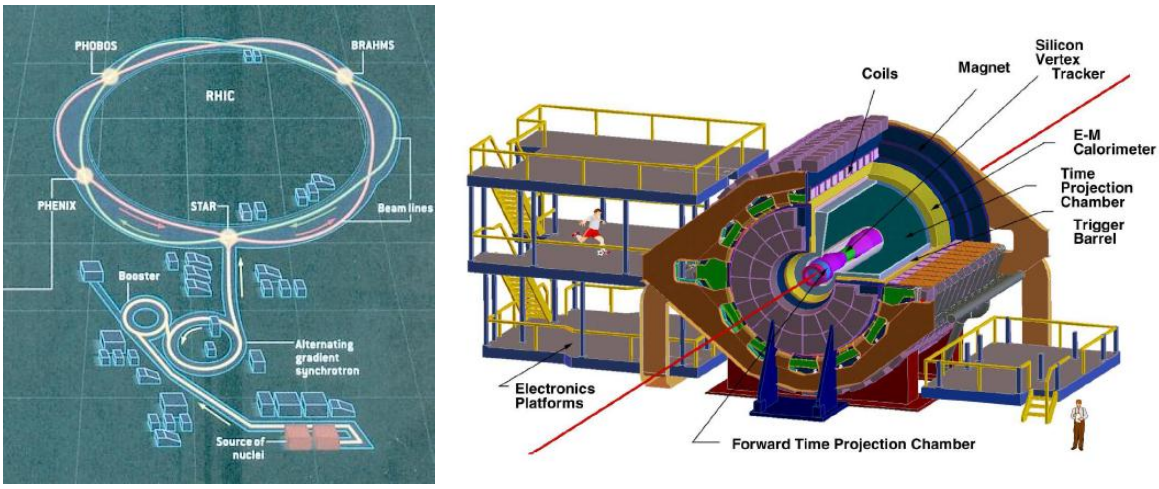

Figure 2.1 (left) Relativistic Heavy-ion Collider at Brookhaven National Lab. (right) The STAR experiment.

2.1 Time Projection Chamber

The TPC [13] is the main charged-particle tracking device in STAR. When a charged particle travels through a TPC chamber, it ionizes the TPC gas molecules along its path. The ionization energy loss (dE/dx) is different for different charged particle and can be used to identify electrons.

Figure 2.2 shows the TPC structure schematically. It is 4.2 m long along the beam line and 4 m in diameter, sits in the STAR solenoid magnet. It is an empty volume of gas in a well-defined, uniform, electric field of 135 V/cm. The paths of primary ionizing particles passing through the gas volume are reconstructed with high precision from the released secondary electrons which drift to the readout end caps at the ends of the chamber. The uniform electric field which is required to drift the electrons is defined by a thin conduction Central Membrane (CM) at the center of the TPC, concentric led-cage cylinders and the readout end caps. The gas the STAR TPC used is P10 gas (10% methane, 90% argon) which has long been used in TPCs, regulated at 2 mbar above atmospheric pressure.

The track of primary particle passing through the TPC is reconstructed by finding ionization clusters along the track. The clusters are found separately in transverse plane and on the direction of beam line. The position resolution depends on the drift length and the angle between the particle momentum and the drift direction and on the level

of mm. After finding and associating the clusters along the track, it is fitted to track models.

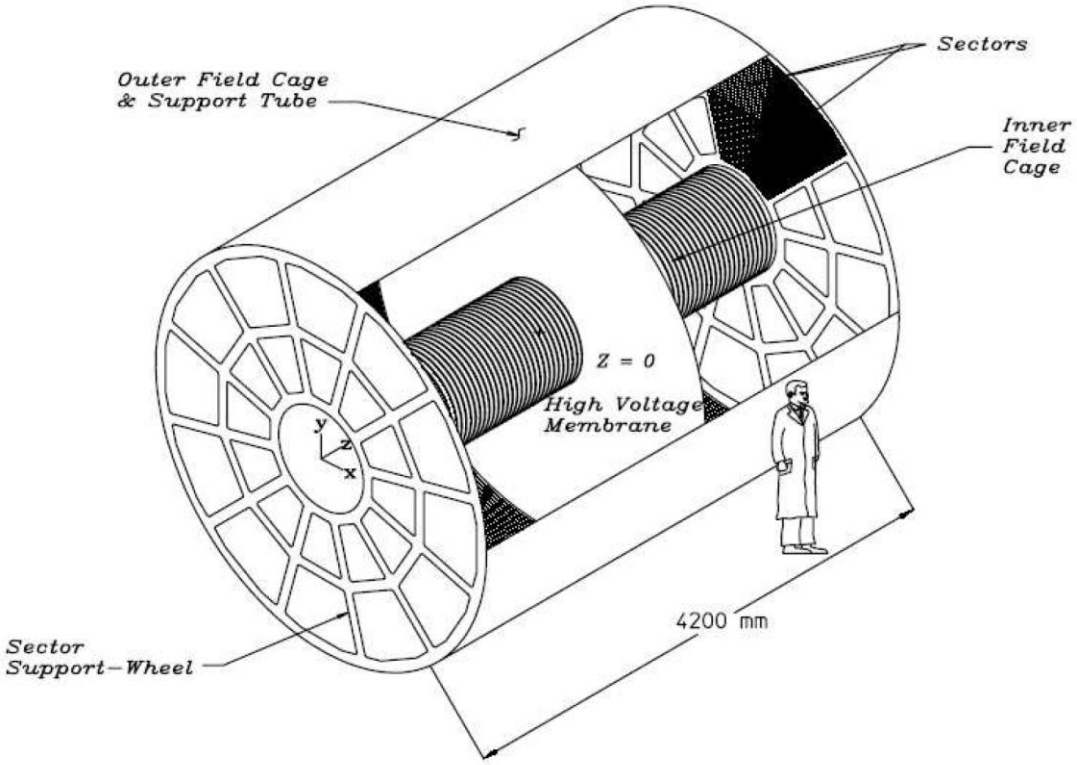

Figure 2.2 The schematics of the STAR Time Projection Chamber.

2.2 Barrel Electro-Magnetic Calorimeter

The BEMC [14] is used to measure the electromagnetic energies of particles. Electrons and photons will generate electro-magnetic showers and deposit most of their energies in the BEMC. The hadrons will mostly deposit a small fraction of their energy. Therefore, the ratio of momentum of energy is another important cut to identify electrons from

hadrons. BEMC towers are also used as a trigger where only events with at least one tower above a certain threshold will be recorded. The tower is single detecting channel in the BEMC detector. These trigger is called high-tower trigger (HT).

While the STAR TPC is nominally a slow detector with Data Ac Quisition (DAQ) rate less than 100 Hz. The STAR BEMC is a fast detector, allows STAR to trigger on and study rare, high p_T processes (jets, leading hadrons, direct photons, heavy quarks) and provides large acceptance in *p+p* and Au+Au collisions. The BEMC is located inside the aluminum coil of the STAR solenoid, between the TPC and the magnet coils, and covers $|\eta| \leq 1$ and 2π azimuthally, matching the acceptance for full TPC tracking. The inner surface of the BEMC has a radius of about 220 cm and parallel to the beam axis.

The design for the BEMC includes a total of 120 calorimeter modules, each subtending 6± in ΔΦ(~ 1 rad) and 1.0 unit in Δη. These modules are mounted 60 in Φ and 2 in η. Each module is roughly 26 cm wide by 293 cm long with an active depth of 23.5 cm plus ~6.6 cm in structural plates (of which ~1.9 cm lies in front of the detector). The modules are further segmented into 40 towers, 2 in Φ and 20 in η, with each tower subtending 0.05 in ΔΦ by 0.05 in Δη. The full BEMC is thus physically segmented into a total of 4800 towers. Each of these towers is in projective and points back to the center of the TPC. Figure 2.3 shows a schematic side view of a module illustrating the projective nature of the towers in the η direction.

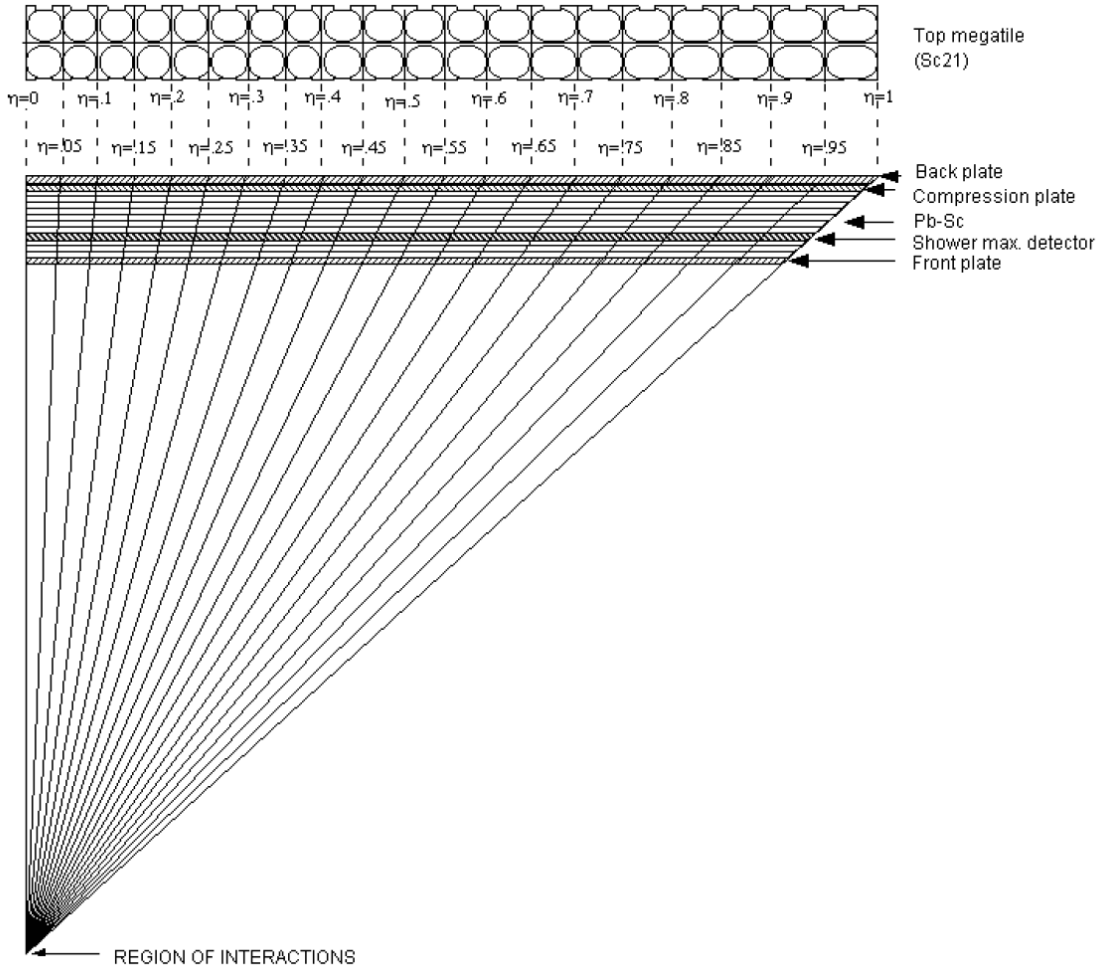

Figure 2.3 Side view of a calorimeter module.

2.3 Barrel Shower Maximum Detector

The STAR BEMC has segmentation (towers) significantly larger than an electromagnetic shower size. Each of its 4800 towers span $\Delta\phi \times \Delta\eta = 0.05 \times 0.05$ which at the radius of the inner face of the detector correspond to tower size ~10×10 cm^2 at η = 0 increasing towards η = 1. Its provides precise energy measurement for isolated electromagnetic

showers but its spatial resolution is not fine enough to measure the shower shape and shower size to distinguish direct γ and π^0. The BSMD with high spatial resolution is embedded in the BEMC to satisfy this requirement.

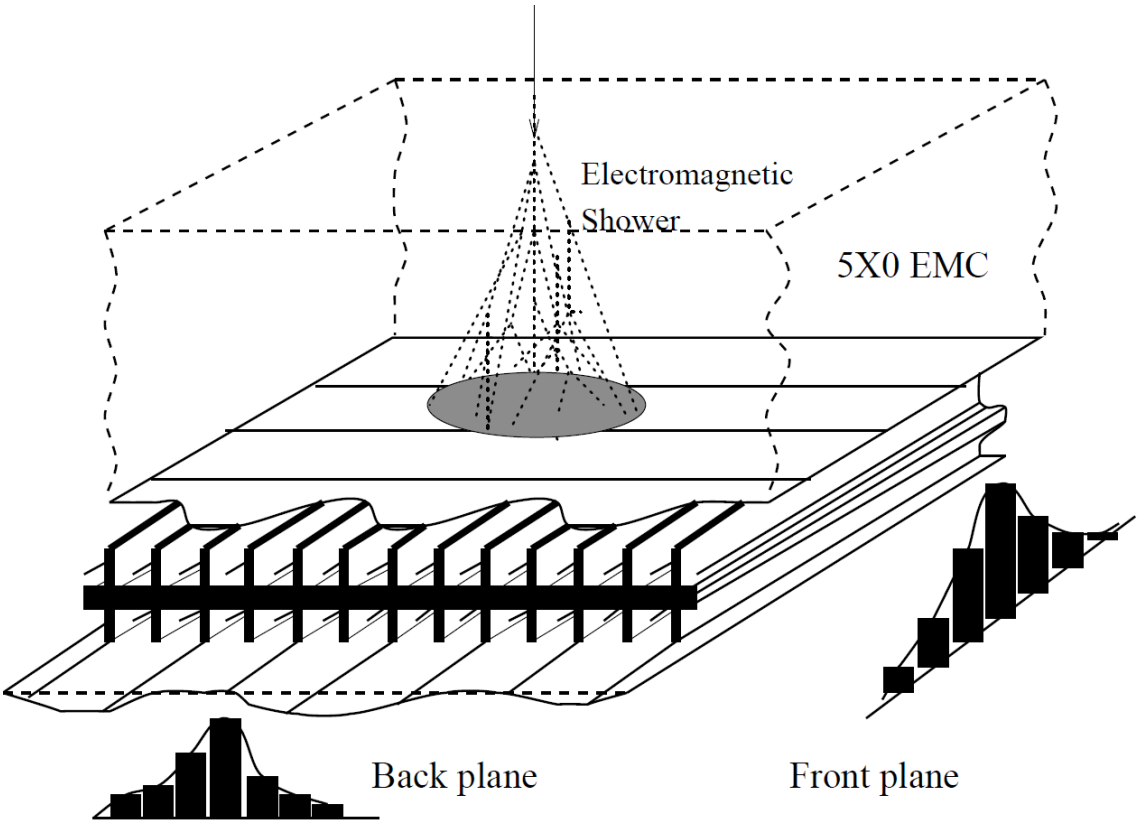

Figure 2.4 Schematic illustration of the double layer STAR BSMD. Two independent wire layers, separated by an aluminum extrusion, image electromagnetic showers on corresponding pad layers.

The conceptual design of the SMD is shown in Figure 2.4. The BSMD is located at about 5 radiation length depth in the calorimeter modules, at η = 0, including all material immediately in front of the calorimeter. A unique feature of the STAR SMD is its double layer design. A two sided aluminum extrusion provides ground channels for two independent planes of proportional wires. Independent PC Board cathode planes with

strips etched in the η and ϕ directions, respectively, allowing reconstruction of a two dimensional image of the shower. The SMD is a wire proportional counter-strip readout detector using gas amplification. The basic structure of the detector is an aluminum extrusion with 5.9 mm wide channels running in the η direction. There are 50 μm gold-plated tungsten wires in the center of the extrusion channels. The detector strips sense the induced charge from the charge amplification near the wire. One set of strips is perpendicular to the wires, making up one side of the channel around the wire outside the aluminum extrusion, and provide an image of the shower spatial distribution in the η direction. Each of these strips spans 30 channels (30 wires). They have size of 0.1 rad in ϕ (~23cm, i.e. the module width) and 0.0064 in η (~1:5 cm at low η). The other set of strips are parallel to the wire channels of the aluminum extrusion. These stripes are physically 1.33 cm wide and have lengths 0.1 units in ´, while the wires are 1.0 units in η. The BSMD has an approximately linear response versus energy, at the depth of $5X_0$ inside the EMC, in the energy range from 0.5 to 5 GeV. The ionization at the back plane of the BSMD is about 10% lower than the front plane.

2.4 STAR TOF Detector

The STAR TOF [15] is built with the Multi-gap Resistive Plate Chamber (MRPC) technology and is capable of d high detection efficiency (>95%) with high timing resolution for minimum ionizing particles. An MRPC basically consists a stack of resistive plates, spaced one from the other with equal sized spacers (such as fish line) creating a

series of gas gaps. It works in avalanche mode. Electrodes are connected to the outer surfaces of the stack of resistive plates while all the internal plates are left electrically floating. Initially the voltage on these internal plates is given by electrostatics, but they are kept at the correct voltage due to the flow of electrons and ions created in the avalanches. There are six read-out strips on each module in this design.

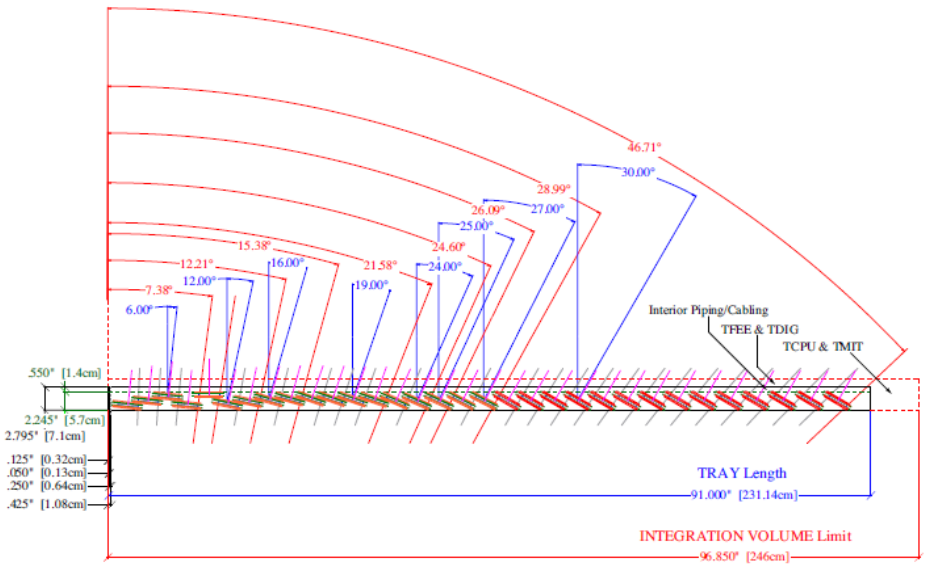

Figure 2.5 A dimensioned side view of the TOF tray

The STAR MRPC TOF is a full-acceptance time-of-flight system matching the acceptance of the TPC, and BEMC. Coverage of the entire sixty square meter area of STAR will be accomplished by placing approximately 3800 MRPC modules in an overlapping geometry within 120 aluminum trays that fit inside the integration envelope of the present STAR Central Trigger Barrel, as shown in Figure 2.5. Each MRPC module has 6 pairs of copper pick-up pads, thus the envisioned detector would comprise approximately 23,000 channels, each having an active area of 3.3 cm × 6.1 cm.

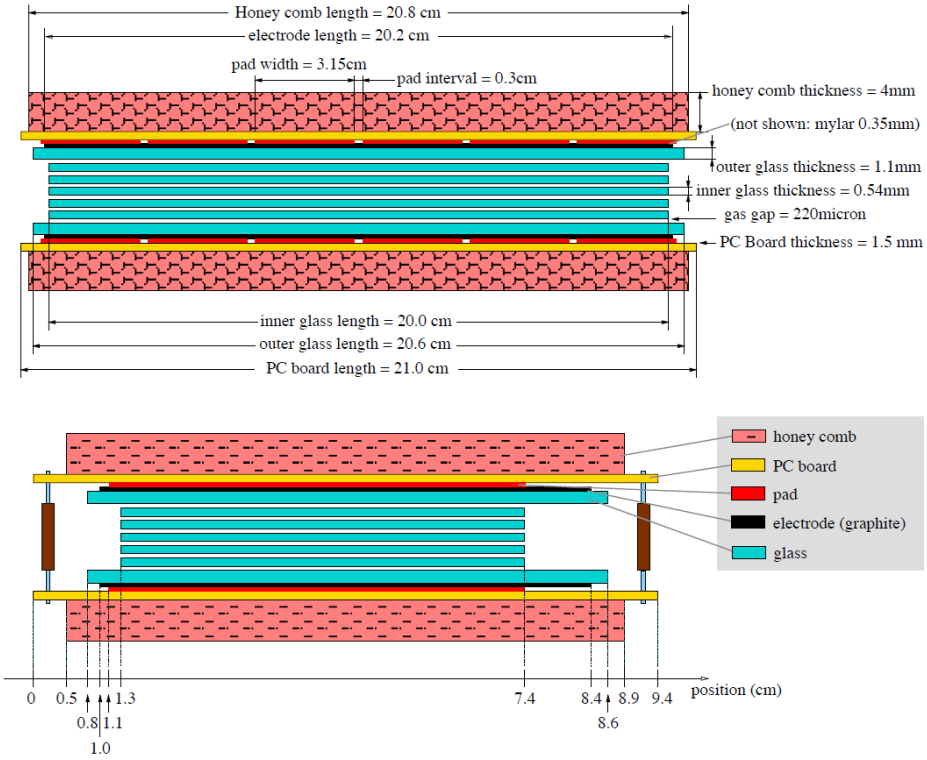

Figure 2.6 Two-side view of a MRPC module

Figure 2.6 shows the two side views (long edge view on top and short edge view on bottom) of an MRPC module appropriate for STAR. With this degree of granularity, the expected occupancy and multiple hit percentage is approximately 12% and 1% respectively for a central Au+Au collision at $\sqrt{s_{NN}}$ = 200 GeV. The full barrel TOF detector extends STAR's present capability for kaon separation from ~0.6 to ~1.7 GeV/c; the range for proton separation would be increased from approximately ~1 GeV/c to ~3.0 GeV/c.

2.5 STAR Minimum-bias Trigger Detectors

The STAR BBC [16] are two identical counters located on each side of the interaction region covering the full azimuth and $2.1 < |\eta| < 5.0$. Each detector consists of sets of small and large hexagonal scintillator tiles grouped into a ring and mounted around the beam pipe at a distance of 3.7 m from the interaction point. In both Run2008 and Run2005, the BBC served as a minimum-bias trigger to record the integrated luminosity by requiring a coincidence of signals in at least one of the small tiles ($3.3 < |\eta| < 5.0$) on each side of the interaction region. The cross-section sampled with the BBC trigger is 26.1 ± 0.2(stat.) ± 1.8(syst.) mb [24] for *p+p* collisions. The timing signal recorded by the two BBC counters can be used to reconstruct the collision vertex along the beam direction with an accuracy of about 40 cm.

During Run2009, a pair of Vertex Position Detectors (VPD) [17] was used to select events. Each VPD consists of 19 lead converters plus plastic scintillators with photomultiplier-tube readout that are positioned very close to the beam pipe on each side of STAR. Each VPD is approximately 5.7 m from the interaction point and covers the pseudo-rapidity interval $4.24 < |\eta| < 5.1$. The VPD trigger condition is similar to that of the BBC trigger except that the VPD has much better timing resolution, enabling the selected events to be constrained to a smaller range (±30) around the interaction point.

3. HIGH P_T NON-PHOTONIC ELECTRON PRODUCTION IN *P+P* COLLISIONS

3.1 Analysis Principle

The main goal of this analysis is to identify statistically the non-photonic electrons from heavy flavor hadrons and photonic electron background, then calculate non-photonic electron invariant cross section. With different detector and trigger setup, RHIC-STAR Run2008 and Run2009 cover different p_T region for non-photonic electron measurement. Run2008 covers p_T > 2GeV/c, while Run2009 covers both 0.2 GeV/c < p_T < 2GeV/c and p_T > 2GeV/c.). Both measurements follow similar analysis principle but rely on different detectors for electron identification.

First use information from TPC, EMC and TOF to identify electrons from hadron background. After that, there are primarily two types of photonic-electron background: one is from photon conversion ($\gamma \rightarrow e^+ + e^-$) and the other is from scalar meson Dalitz decay. The electrons from scalar meson Dalitz decay include electrons from π^0 Dalitz decays ($\pi^0 \rightarrow e^+e^-\gamma$), electrons from η Dalitz decays, etc. Among them, electrons from π^0 Dalitz decays dominate. The following procedure is applied to reject photonic electrons:

- Since all the non-photonic electrons come almost directly from the primary

vertex of the event while the photon conversion electrons come only from the conversion points where material exists, a 1.5cm cut on the track's Distance of the Closest Approach (DCA) to the event's primary vertex is applied to partially remove photon conversion electrons.

- A large fraction of remaining background electrons can be further identified by invariant mass cut. If an electron pair comes from a photon conversion or Dalitz decay, its invariant mass will peak in small value. Mass from non-correlated electron has a continuum shape and form the combinatorial background for the photonic electron reconstruction.

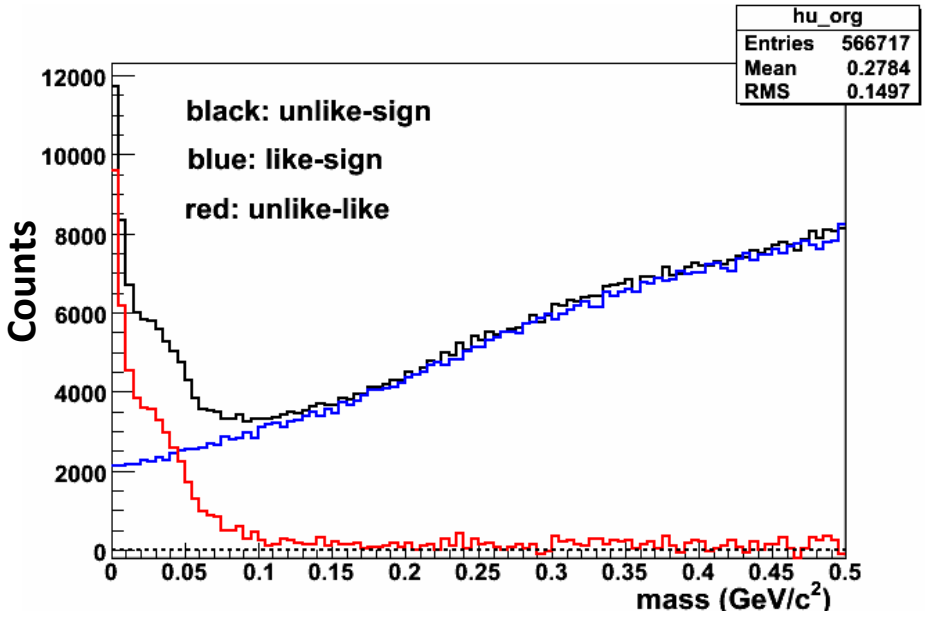

Figure 3.1 Invariant mass distribution from electron candidate pairs. The value of the p_T is from the global track of the primary electron. The black histogram is from unlike-sign pairs and the blue histogram is from the like-sign pairs. The red histogram is unlike-like pairs.

Figure 3.1 shows the reconstructed electron pair mass. The photonic electrons are reconstructed statistically through subtracting the same-charge-sign (like-sign) electron pairs mass from that of the opposite-charge-sign (unlike-sign) electron pairs. The unlike-sign pairs include the photonic electrons pairs plus those from non-correlated electrons which can be represented by the like-sign pairs, therefore subtracting like-sign pairs from unlike-sign pairs will statistically lead to the mass distribution from pure photonic electrons. The width of the mass distribution increases as a function of the primary electron p_T, i.e. p_T(prim) which is the p_T of electron candidate from primary tracks. A mass<0.24 GeV cut should keep all the photonic electrons that has a partner reconstructed in all p_T(prim) region. There are two peaks in the pure photonic electron mass distribution. The smaller one happens when the two electron helix do not intersect each other in X-Y plane where the reconstructed opening angle is small, the larger one happens when the two helix intersect each other in X-Y plane where the reconstructed opening angle is large than the actual one and lead to a larger mass.

A fraction of the electrons from the pairs cannot be tracked by TPC because of the low p_T or outside the acceptance. This inefficiency is taken into account by 1-ε where the ε is called photonic reconstruction efficiency which is obtained from embedding. So the non-photonic electron from heavy quark decay is equal to:

$$N(non-photonic-electron) = N(inclusive-electron)\cdot purity - N(photonic\_electron)/\varepsilon$$

Figure 3.1 shows that unlike-like Sign leads to the mass distribution of pure photonic electron. One can use the same technique to obtain any distribution from pure photonic electrons. Here the purity is the fraction of real electrons in the electron candidates.

3.2 Data sets and Triggers

There are 3 high tower triggers in Run2008.

1. HighTower#0 (HT0):

Trigger Id: 220500 BBC coinc. + BEMC HT at threshold 11(2.4 GeV)

Number of events after prescale : 4.65e+06

Number of event before prescale: 7.65e+07

Number of events after prescale at |Zvtx|<30cm : 1.76e+06

Number of event before prescale at |Zvtx|<30cm: 2.90e+07

Sampled BBC minimum-bias events: 6.44e+10

2. HighTower#1 (HT1):

Trigger Id: 220510 BBC coinc. + BEMC HT at threshold 15(3.4 GeV)

Number of events after prescale: 3.71e+06

Number of event before prescale: 1.19e+07

Number of events after prescale at |Zvtx|<30cm : 1.39e+06

Number of event before prescale at |Zvtx|<30cm: 4.48e+06

Sampled BBC Minimum-bias events: 6.58e+10

3. HighTower#2 (HT2):

Id: 220520 BBC coinc. + BEMC HT at threshold 18 (4.1 GeV)

Number of events after prescale: 3.74e+06

Number of event before prescale: 3.96e+06

Number of events after prescale at |Zvtx|<30cm : 1.41e+06

Number of event before prescale at |Zvtx|<30cm: 1.50e+06

Sampled BBC minimum-bias events: 6.58e+10

Note that the "sampled minimum-bias events" means the number of minimum-bias events sampled by a trigger.

3.3 Combination of the Cascaded High Tower triggers

The technique of combining all HT triggers for p_T spectrum is done through the following procedure:

TH1F* h0 = HT0 && !(HT1||HT2)&& ADC<16 × prescale_HT0

TH1F* h1 = HT1 && !HT2 && 16<=ADC<19 × prescale _HT1

TH1F* h2 = HT2 && ADC>=19 × prescale_HT2

TH1F* hcomb = h0+h1+h2,

where HT0, HT1 and HT2 means an event is marked as a HT0, HT1 and HT2 trigger events, respectively ; !(HT1||HT2) means an event fired neither HT1 and HT2 trigger; !HT2 means an event did not fire HT2 trigger; ADC is the adc value of a electron

obtained from trigger simulator; hcomb is the final combined spectrum. The number 16, 19 correspond to the HT1 and HT2 threshold. Note that in principle one can also use adc0 instead of ADC, but the combined spectrum is not perfect and there are small holes in the boundary between two trigger thresholds.

Here Figure 3.2 shows the high tower adc distribution for HT0, HT1, the combined spectrum and its different components. If one cut only on trigger bit, some of the electrons go beyond the trigger boundaries because some masked-out towers in the trigger show up offline. Therefore, when combining all HT triggers one need to cut out the grass according to the real trigger threshold.

Figure 3.3 shows the ratio of HT0, HT1 adc spectrum over the combined spectrum. If the combination technique works well, the ratio should be 1.0 which is very close to what are shown in the figure. A 5% systematic error will cover the difference.

3.4 Electron Identification Cuts

The following electron identification cuts are applied to identify electron candidates.

1. Track Quality cut:

Number of TPC point to fit the track, i.e. nfit>20

nfit/nmax>0.52, where nmax is the number of maximum point on a track

dcag <1.5cm, where dcag is the track global DCA distribution.

R(TPC 1st point) < 70 cm, where R(TPC 1st point) is the radial location of the first point of a TPC track. This cut can remove electrons reconstructed with low quality which are mainly photonic electrons produced at large radius.

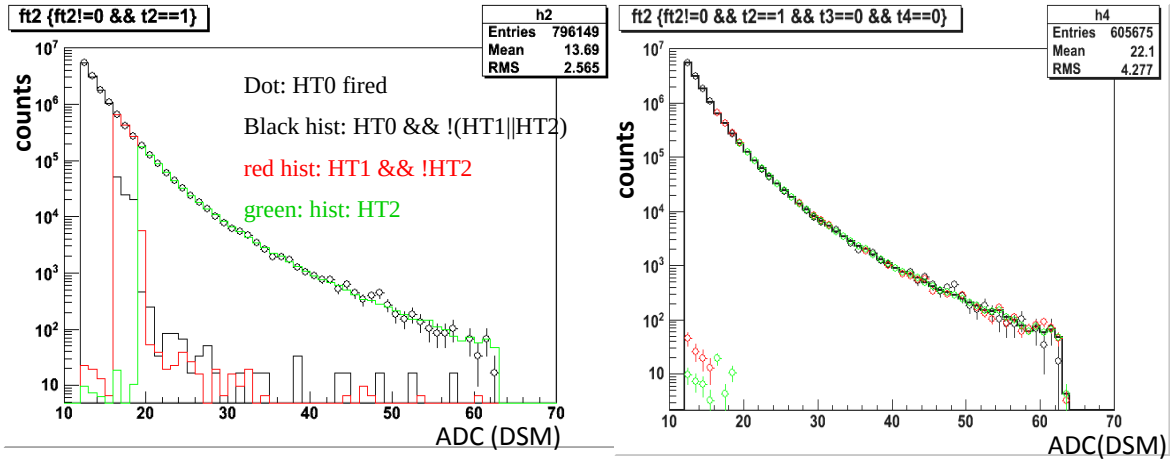

Figure 3.2 Left panel: open circles are adc distribution from HT0 trigger and each component of the combined spectrum; the black histogram is the combined spectrum. Right panel: same as left but the grass beyond the trigger threshold are removed.

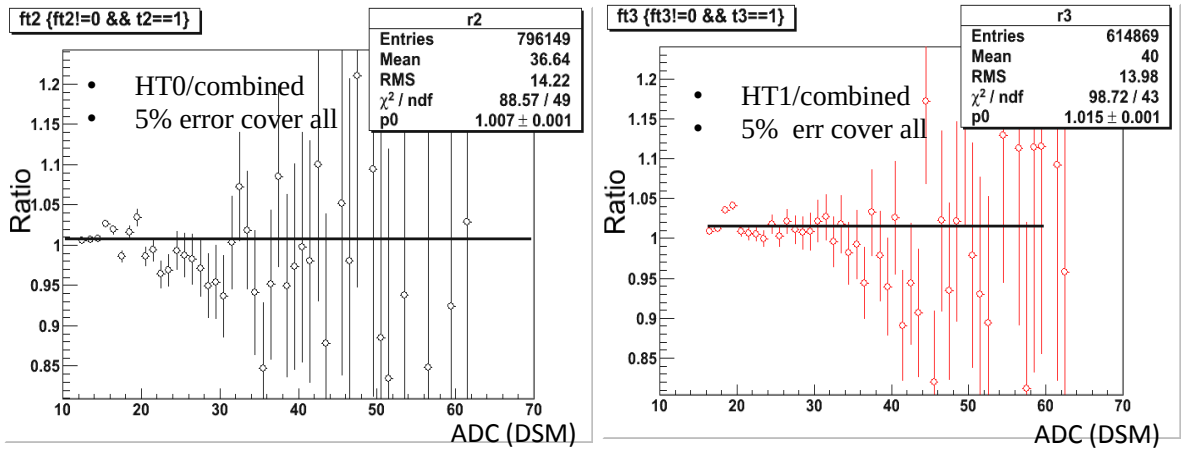

Figure 3.3 Left: the ratio of ADC from HT0 over the combined spectrum. Right: same as left panel but for HT1 trigger.

2. Electron Identification cut:

- $0 < p/E0 < 2$, where p is the track momentum and E0 is the energy of the most energetic tower in the track associated BEMC cluster. An electron will deposit almost all of its energy in the BEMC towers because the towers have 21 radiation lengths. So the ratio of P to E should be around 1 for electrons, while hadrons tend to have small small p/E value since the fraction of its energy deposited in BEMC is usually small.
- |btowdphi|<0.1 rad. && |btowdz|<20 cm, where btowdphi and btowdz are the track association window for BTOW cluster in R-phi planes and pseudo-rapidity direction, respectively.
- |bsmdedphi|<0.15 rad. && |bsmdedz|<15 cm, where bsmdedphi and bsmdedz are the track association window for BSMD(η) cluster in R-phi planes and pseudo-rapidity direction, respectively
- |bsmdpdphi|<0.15 rad. && |bsmdpdz|<20 cm, where bsmdpdphi and bsmdedz are the track association window for BSMD(Φ) cluster in R-phi planes and pseudo-rapidity direction, respectively
- $n\sigma_e > -1$. We used $n\sigma_e$ cut instead of dE/dx to identify electrons from hadrons. $n\sigma_e$ is a better quantify to use since it corrects the path length dependence of the dE/dx.

$$n\sigma_e = \log\left(\frac{\frac{dE}{dx}}{B_e}\right)/\sigma_e$$

where dE/dx is the measured energy loss in experiment and B_e is the parameterized form of the energy loss from Bethe-Bloch theory. Ionization energy loss dE/dx is measured by TPC. For a certain TPC gas mixture, dE/dx is a function of particle's momentum and different particles follow different function. From Bethe-Bloch theory, dE/dx is a function of the β and the charge of a particle: $dE/dx = Z^2 f(\beta)$. When a plot of dE/dx versus particle's momentum is made, there is a different curve for each different particle as shown in Figure 3.4.

- nbsmde>1 && nbsmdp>1, where nbsmde and nbsmdp are the number of fired strips in BSMD(η) and BSMD(Φ), respectively.

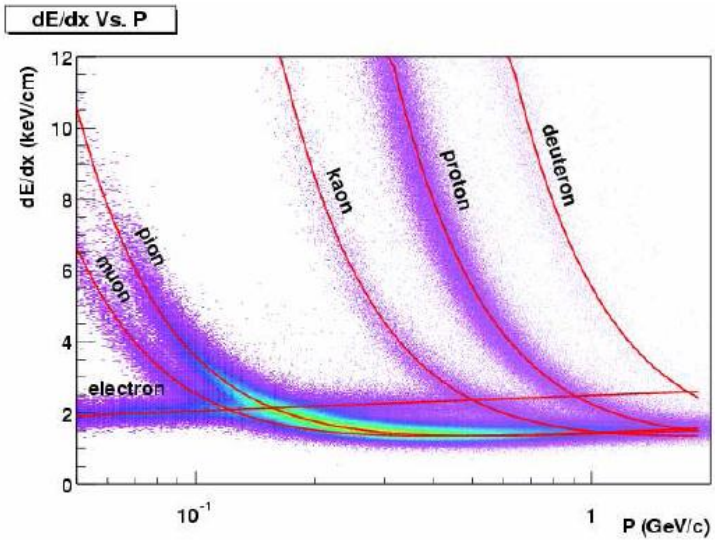

Figure 3.4 dE/dx vs. p measured by the STAR TPC for different particles

Other cuts:

- |Zvtx| < 30 cm, where Zvtx is the collision vertex along beam direction.

- $|\eta| < 0.5$, where η is track pseudorapidity.
- |pDCA|<1.0cm, where pDCA is the DCA between electrons helix in a pair
- The Global partner of the Primary track for a electron pairs:
    - 3.0e-6 < dE/dx < 5.0e-6, which including all true electrons.
    - p_T(partner) > 0.2 GeV or 0.3 GeV, where p_T(partner) is the partner electron p_T in a pairs. This cut is to ensure the photonic reconstruction efficiency can be correctly calculated through Monte Carlo simulation.
    - 3-D mass < 0.24GeV which minimize the impact of hadrons and other single electron and obtain pure photonic electrons.

When associating an electron with BEMC cluster, the association is done for BTOW, BSMD(η) and BSMD(η) separately. The associated cluster is picked as the one that has the closest 3-D distance from the electron. In high multiplicity environment like in Au+Au collisions, this will leads to random association but in *p+p* collision, the random association is very small and can be neglected.

Figure 3.5, Figure 3.6 and Figure 3.7 show the electron association window with BTOW, BSMD(η) and BSMD(Φ) cluster in R-phi and eta direction. The red histograms are pure electron distribution from unlike-like technique. The widths of these distributions are determined by the position resolution of the reconstructed clusters from each subsystem as well as the projection resolution of TPC tracks on the corresponding subsystem. For example, the reason that the bsmdedphi has a wide distribution than

bsmdedz is mainly due to the fact that the wires of BSMD(η) is aligned along beam direction leading to a worse position resolution azimuthally.

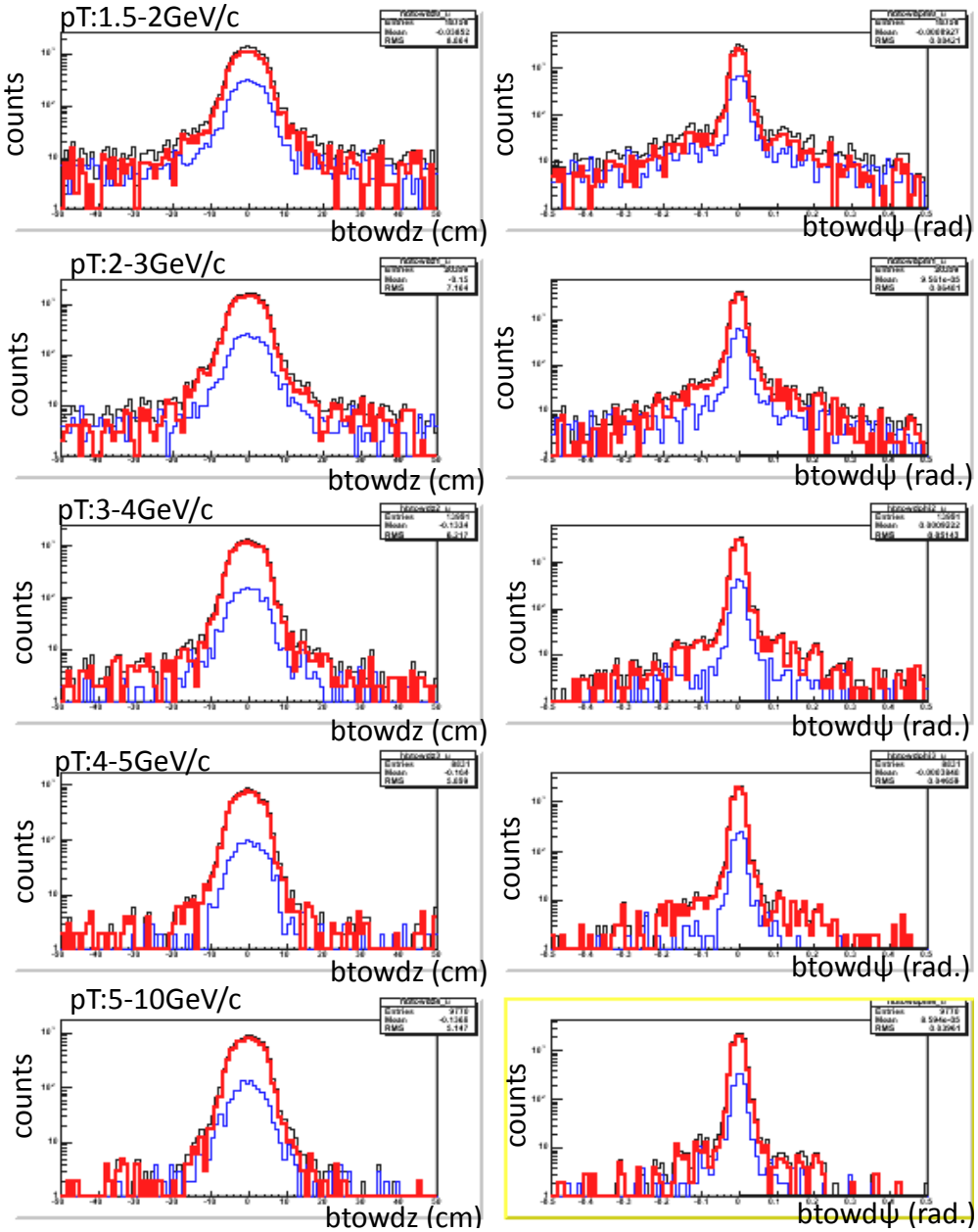

Figure 3.5 Electron association window with BTOW cluster in R-phi and eta direction in different primary electron p_T region. Black: unlike-sign pairs; blue: like-sign pairs; red: unlike-like.

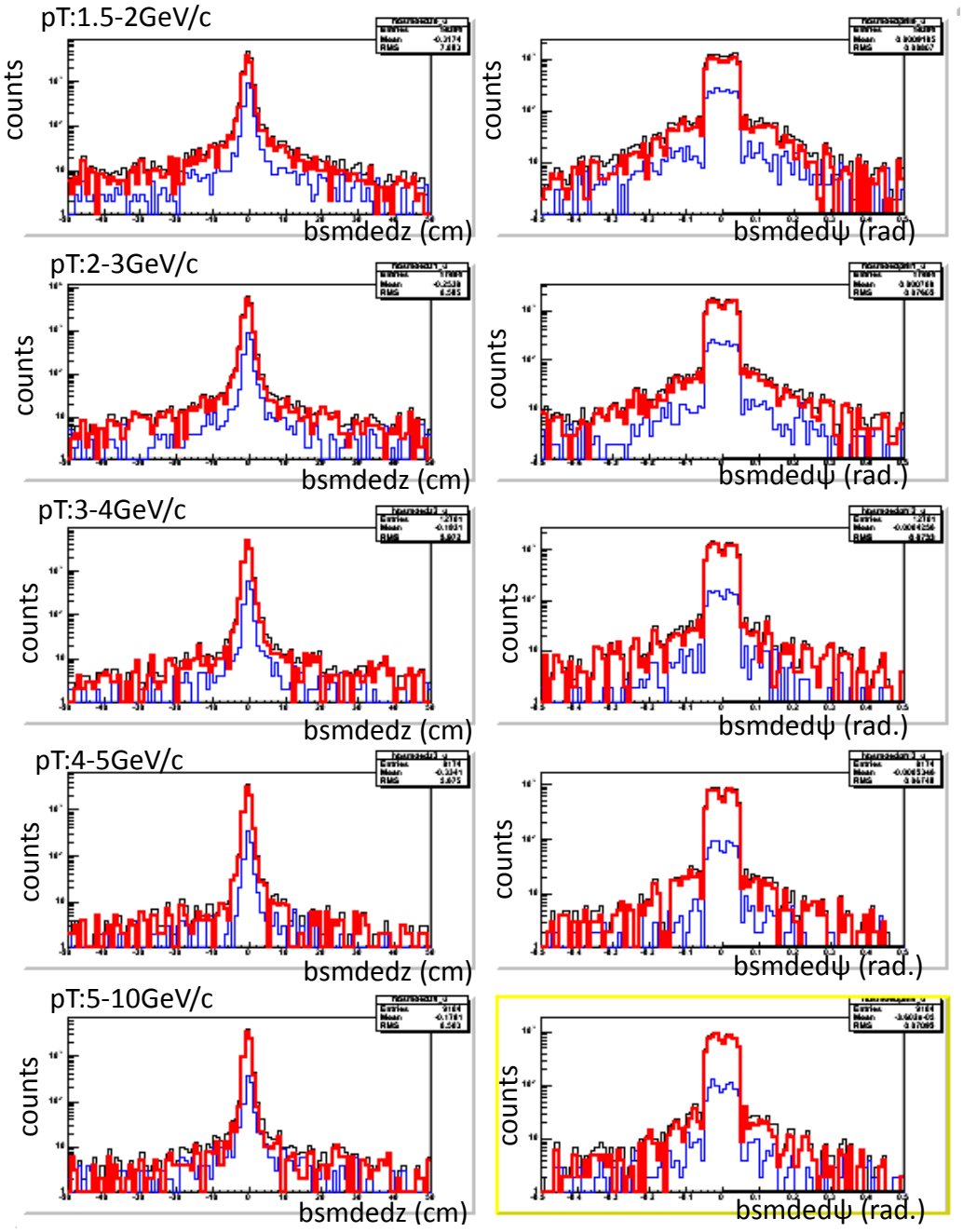

Figure 3.6 Electron association window with BSMD(η) cluster in R-phi and eta direction in different p_T(prim) region. Black: unlike-sign pairs; blue: like-sign pairs; red: unlike-like.

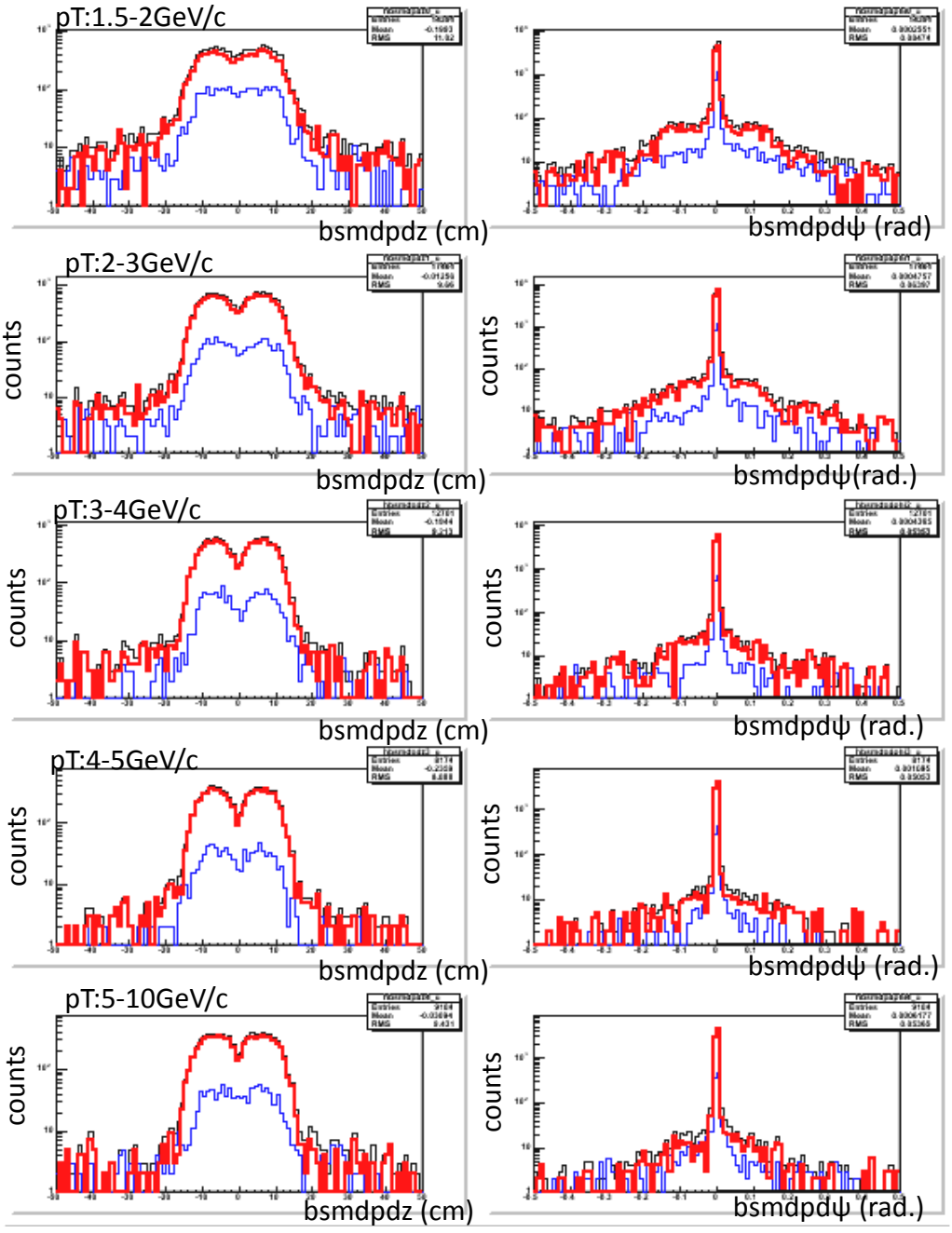

Figure 3.7 Electron association window with BSMD(Φ) cluster in R-phi and eta direction in different primary electron p_T region. Black: unlike-sign pairs; blue: like-sign pairs; red: unlike-like.

3.5 Purity Estimation for Inclusive Electron Candidates

After $n\sigma_e$ cut, there are still some hadrons combined in inclusive electron candidates. Use the shape of $n\sigma_e$ distribution for pure electron (one gaussian distribution) and pure hadron (two gaussian distributions for pion and kaon) to set up the three-gaussian fit the $n\sigma_e$ (constraint fit) for inclusive electrons, then we can estimate the purity of $n\sigma_e$ cut.

There are three steps in purity estimation. The first is to obtain the $n\sigma_e$ distribution from pure electron using unlike-like technique. The next step is to constrain the mean of the $n\sigma_e$ distribution from pion and kaon using Bischel function. Then we do a constraint fit on the $n\sigma_e$ distribution using 3-Gaussian function to obtain the purity.

Figure 3.8 shows the $n\sigma_e$ distribution from pure electrons using unlike-like technique in each p_T bin. All electron identification cuts except the $n\sigma_e$ cut have been applied in the plots. The distribution is well fitted with Gaussian function. If the calibration is perfect, the mean should be 0 and sigma should be 1.0. Figure 3.9 shows the pure electron mean and sigma of the fitting as a function of the p_T. One can see the mean and sigma is deviated from the ideal value. We fit the mean and sigma vs. p_T using pol2 function. The dotted line in the figure represent the one sigma deviation from the mean value and are obtained by moving all the data point up or down by 1-sigma and then fit with a pol2 function.

The mean and sigma of the pion and kaon are obtained from the B70M version of Bischel function. The width of the distribution is set to be around 1.0. The left panel of Figure 3.10 shows the different version dE/dx vs. βγ calculation in STAR. The B70M is used in the purity estimation. The right panel shows the prediction from Bischel function in pion, kaon dE/dx and its good comparison with the data.

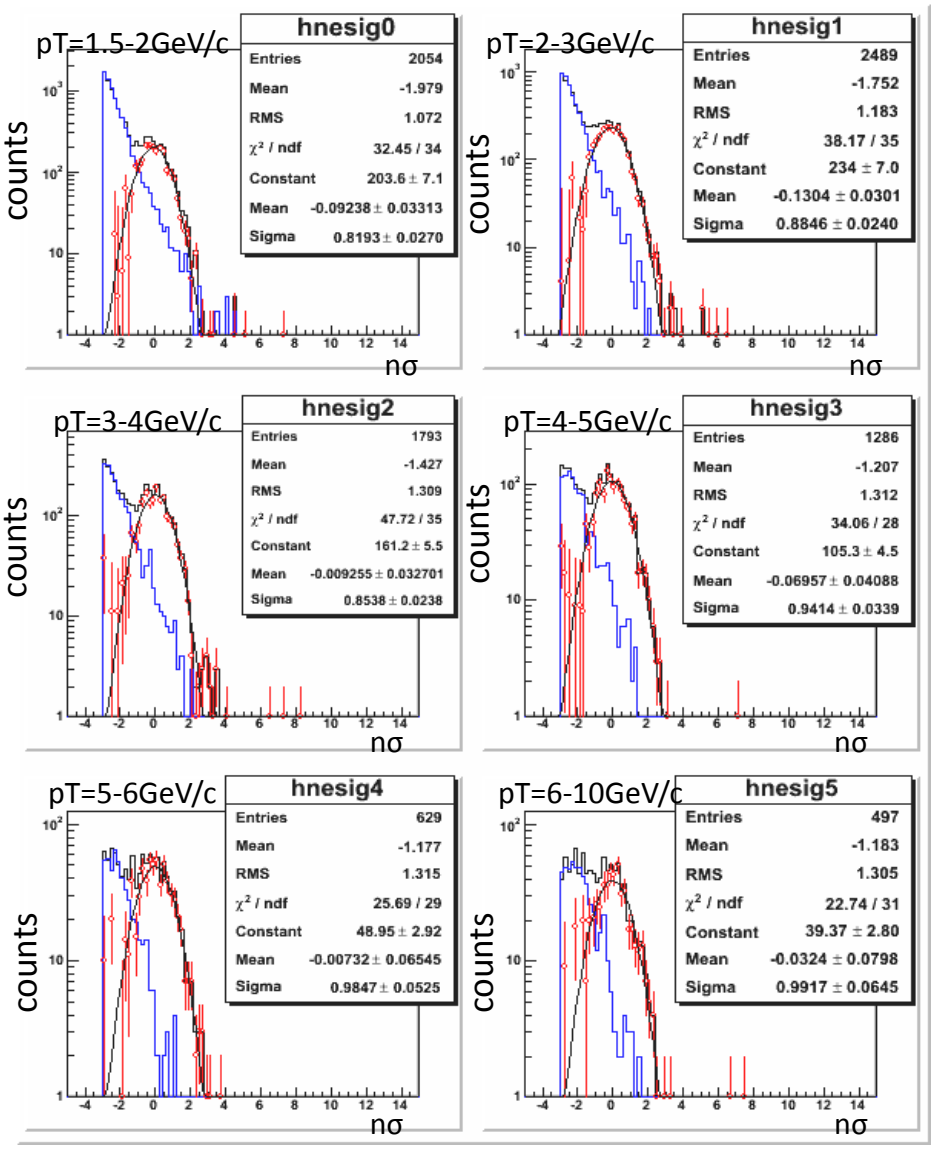

Figure 3.8 Pure electron $n\sigma_e$ distribution in different p_T(prim) bin. Black: unlike-sign; blue; like-sign; red: unlike-like

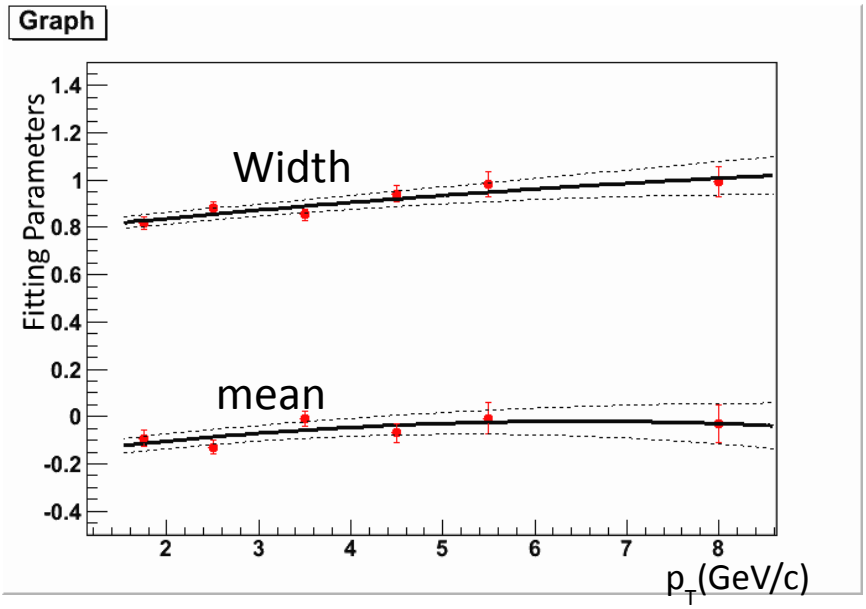

Figure 3.9 mean and sigma of the Gaussian fitting function for the pure electron $n\sigma_e$ distribution. The dotted line correspond to 1 sigma error.

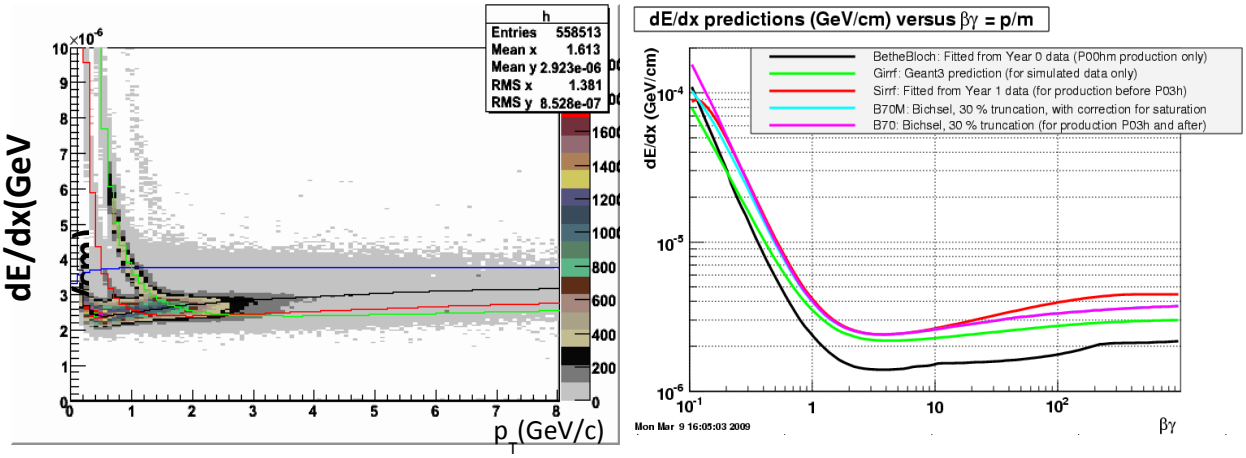

Figure 3.10 Left panel: different version of Bischel function used in STAR tracking. Right panel: The dE/dx vs. p_T for pion, kaon, proton from data and the prediction of B70M version of Bischel function.

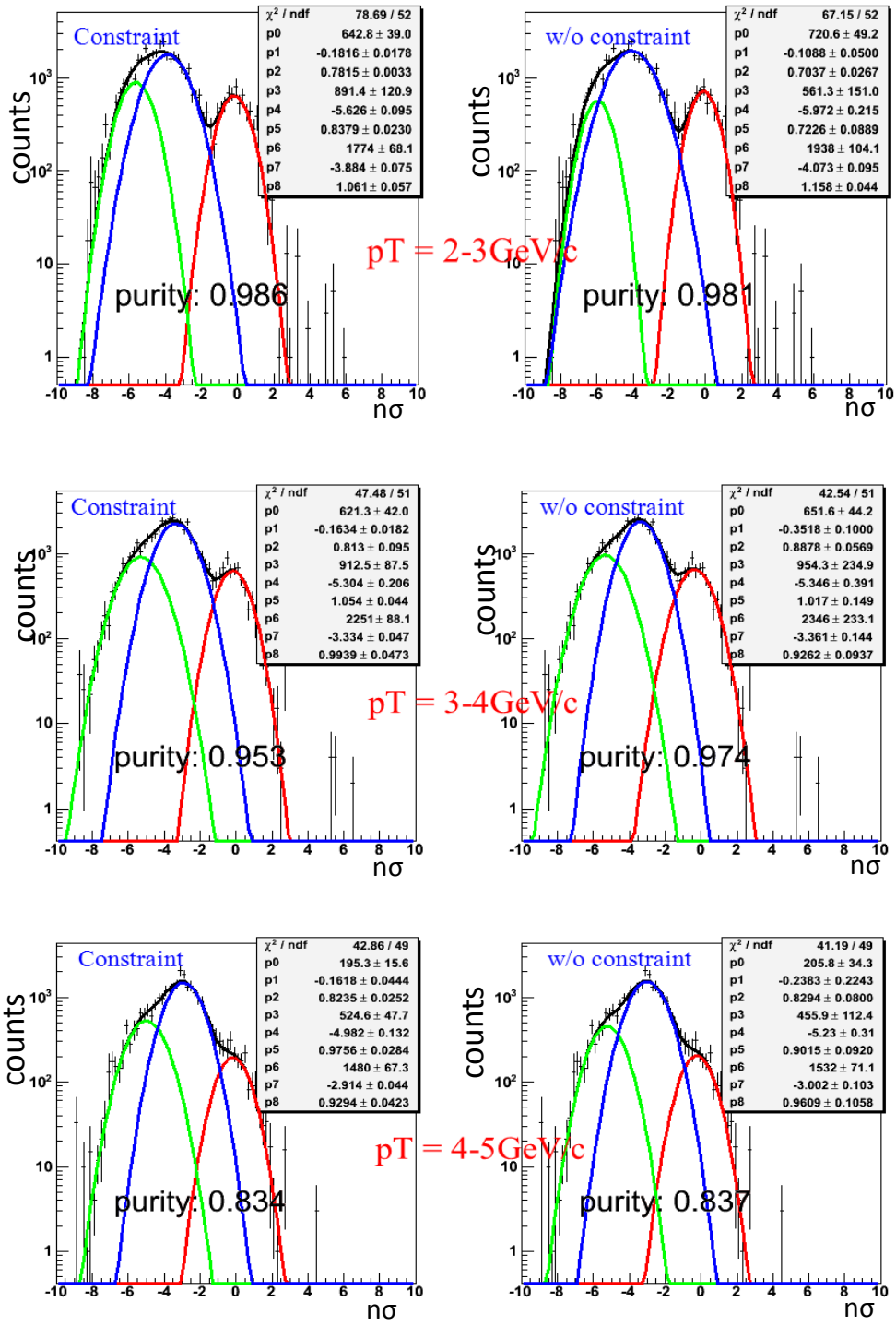

Figure 3.11 $n\sigma_e$ distribution for tracks passed through all electron identification cut except the $n\sigma_e$ cut in different p_T(prim) region including the 3-Gaussian fitting component from kaon+proton (green), pion (blue) and electron (red) with constraint (3-sigma) and without constraint on the electron peak shape for 2 GeV/c < p_T<5 GeV/c.

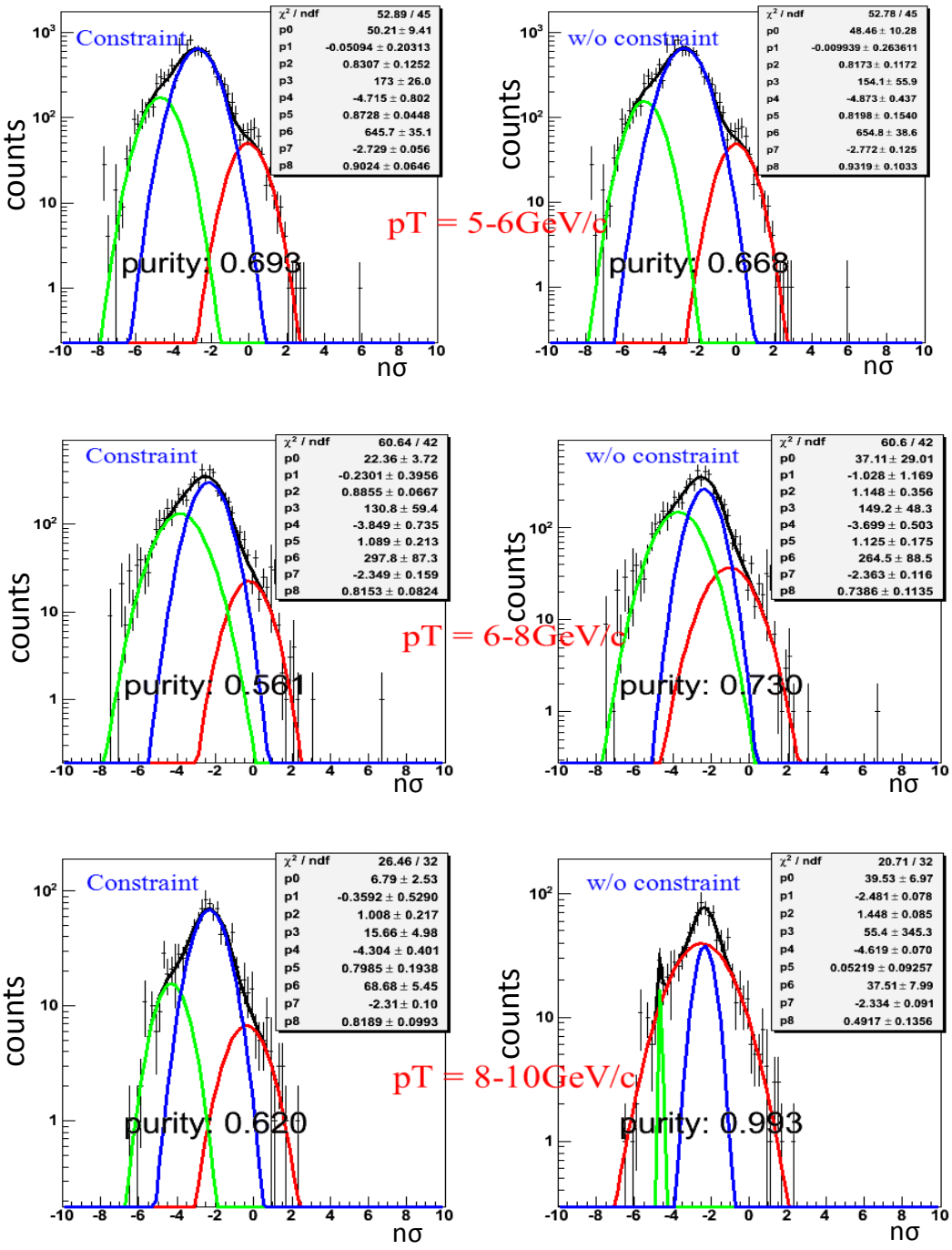

Figure 3.12 $n\sigma_e$ distribution for tracks passed through all electron identification cut except the $n\sigma_e$ cut in different p_T(prim) region including the 3-Gaussian fitting component from kaon+proton (green), pion (blue) and electron (red) with constraint (3-sigma) and without constraint on the electron peak shape for 5 GeV/c < p_T <10 GeV/c.

Figure 3.11 and Figure 3.12 shows the constraint 3-Gaussian fit on the $n\sigma_e$ distribution for tracks that passed all electron identification cut except the $n\sigma_e$ cut with and without constraint on the electron shape. In the constraint case, the mean and sigma of electron shape are allowed to vary by 3-sigma. In the unconstraint case, the parameter values from the constraint fit are used as the initial value. One can see, with or without constraints on electron shape, the purity changes little at p_T <6GeV/c, while at p_T >6GeV/c, the fit without constraint explode. This is expected since the statistics at this p_T region is small. Without any constraint, the fit turns to find the minimum chi2, leading to unreasonable result.

To estimate the 1-sigma statistical uncertainty of the purity, we randomly shift all data points in the $n\sigma_e$ distribution assuming each point follows a Gaussian distribution with sigma equal to the point error and do 3-Gaussian fit. We repeat this 1000 times and obtain purity distribution where the uncertainty is obtained. Figure 3.13 shows these purity distribution in different p_T bin. We fit each distribution with a Gaussian and obtain the uncertainty. To estimate the systematic uncertainty of the purity, we allow electron shape to vary up to 1, 2, 3 and 4 sigma. For each of the 4 constraints, we calculate a purity. The final purity is taken as the average of the 4 values. The systematic error is taken as the largest difference between the mean and the 4 values. The purity value for each of the constraint in each p_T bin can be found in Figure 3.14, Figure 3.15 and Figure 3.16. Figure 3.17 shows the purity vs. p_T for different $n\sigma_e$ cut. The error is the 1-sigma fitting error.

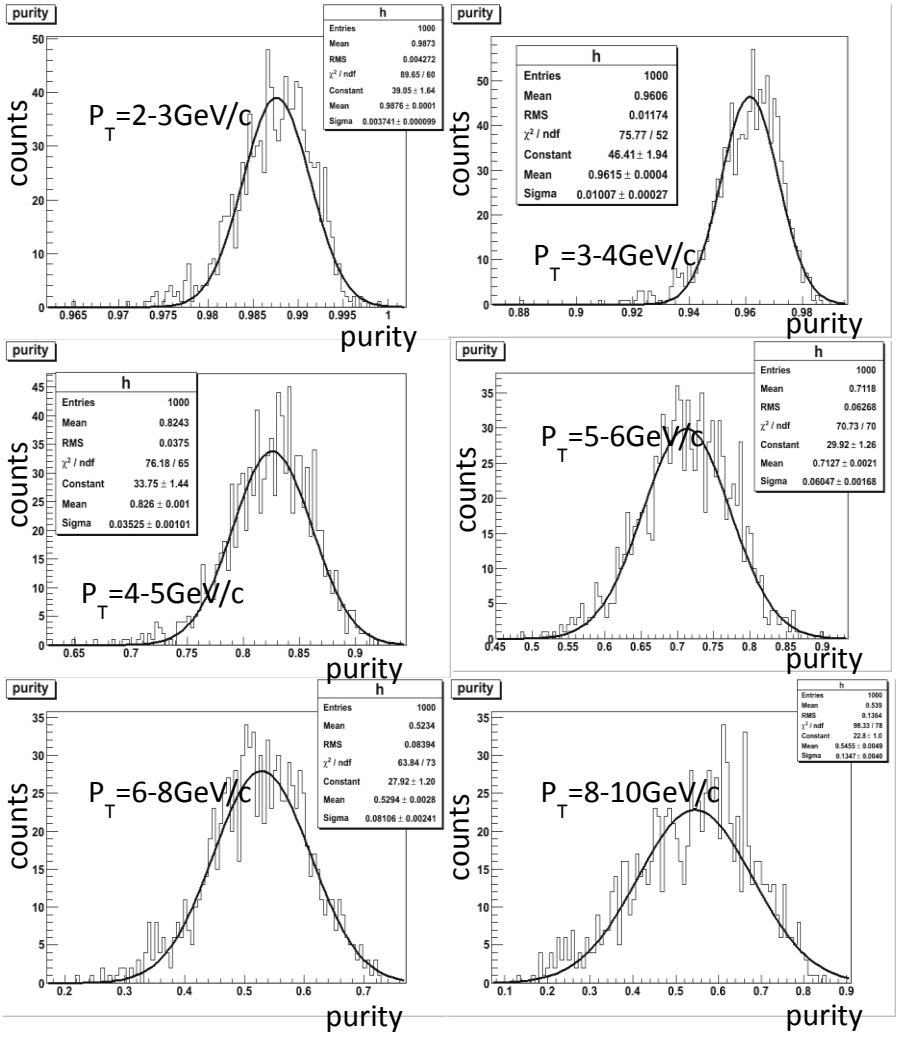

Figure 3.13 purity distributions for each p_T bin. See text for details.

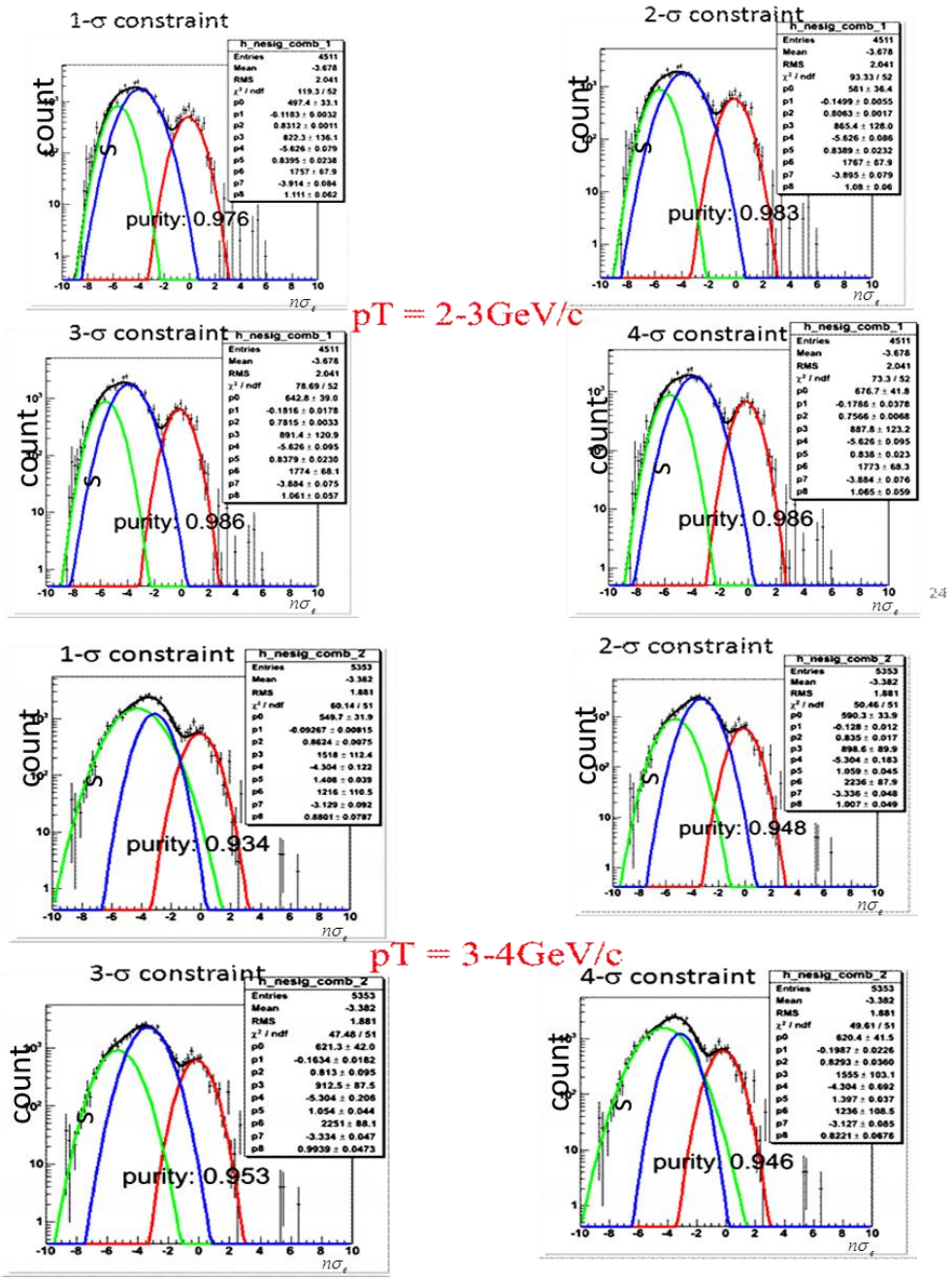

Figure 3.14 3-Gaussian fit with electron mean and width constrained to 1, 2, 3, 4 sigmas from their central value for 2 GeV/c < p_T<4 GeV/c.

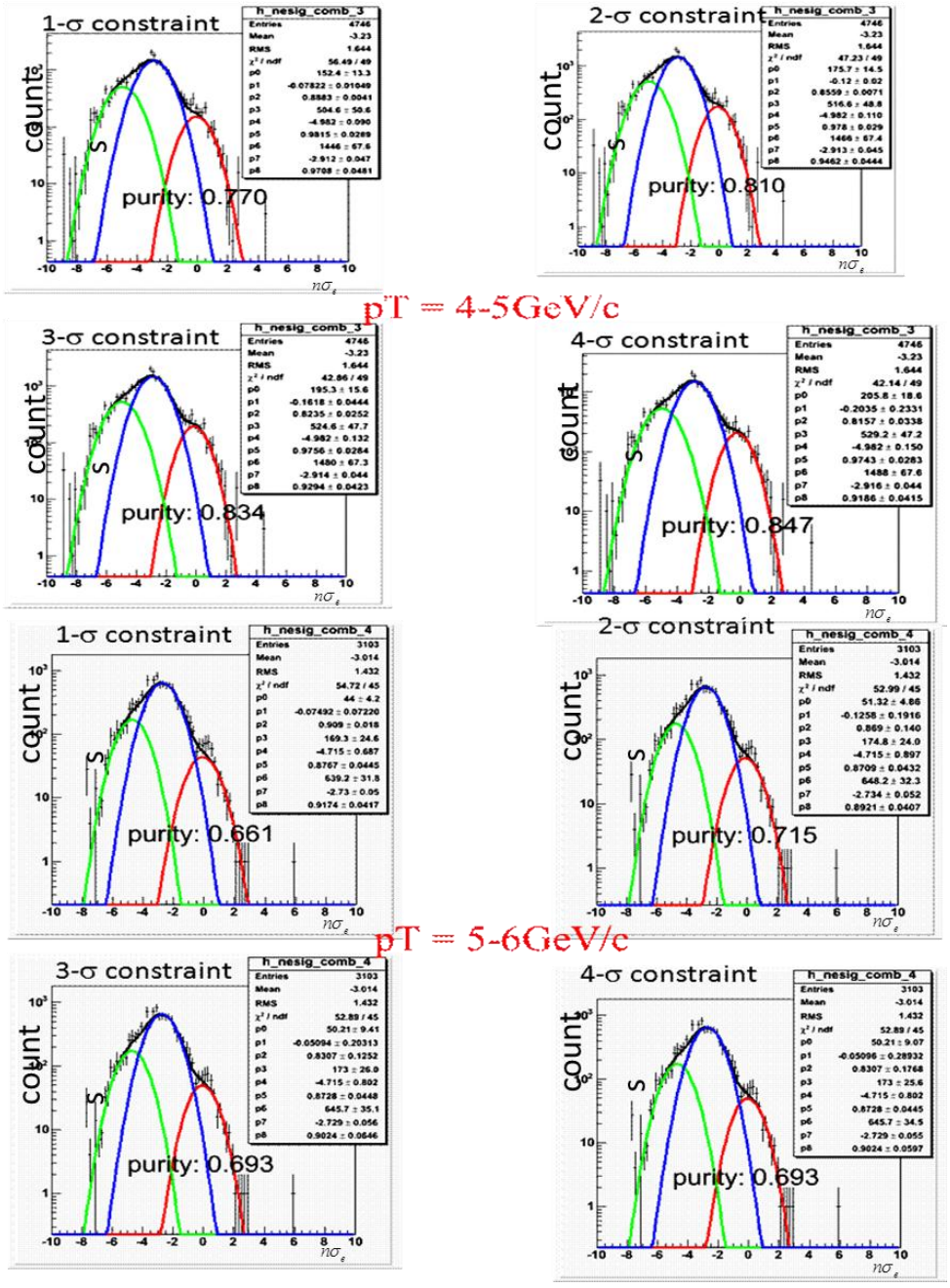

Figure 3.15 3-Gaussian fit with electron mean and width constrained to 1, 2, 3, 4 sigmas from their central value for 4 GeV/c < p_T<6 GeV/c.

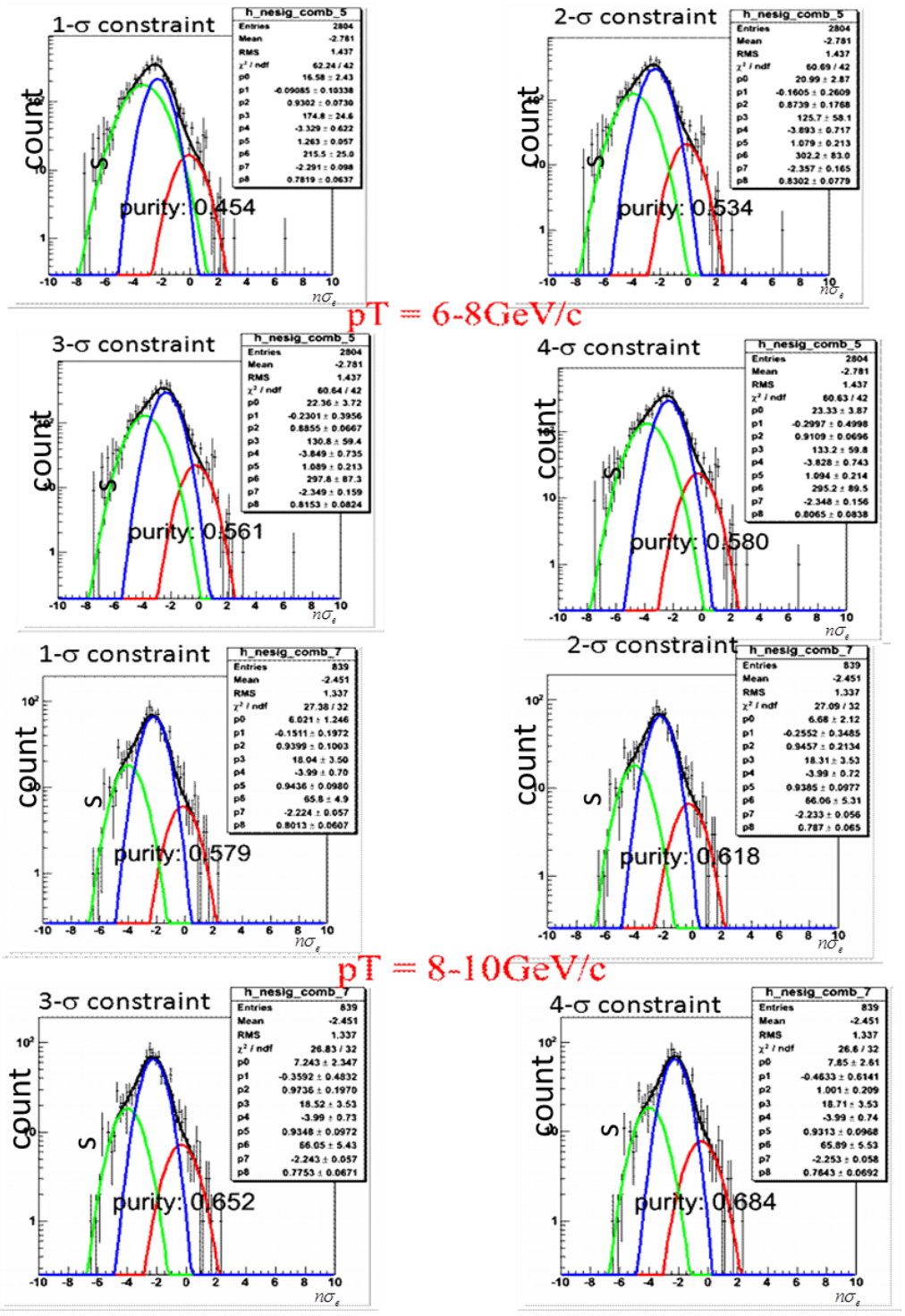

Figure 3.16 3-Gaussian fit with electron mean and width constrained to 1, 2, 3, 4 sigmas from their central value for 6 GeV/c < p_T<10 GeV/c

.

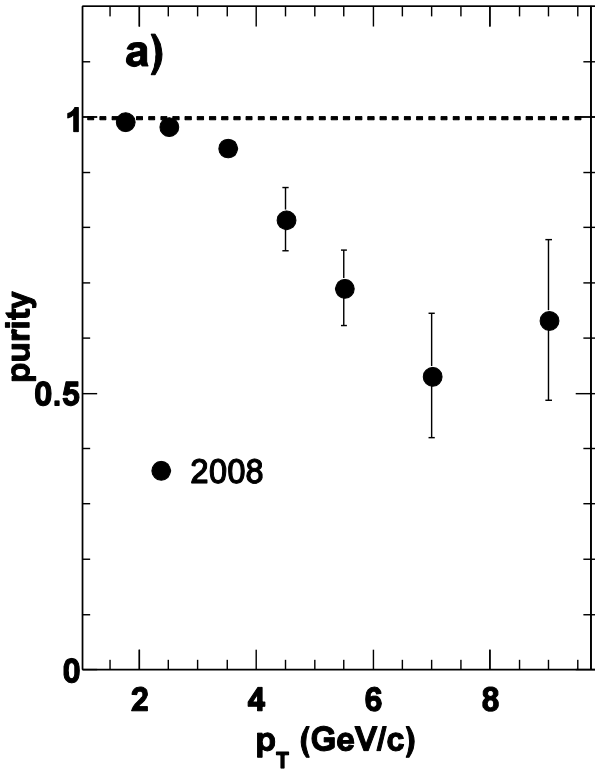

Figure 3.17 Purity vs. p_T with R(TPC 1st)<70cm. The error bars represent one standard deviation.

3.6 Trigger Efficiency Analysis

Trigger efficiency is defined as the fraction of non-photonic electron that have an associated BEMC tower adc value above the trigger threshold. In the analysis, we used data from different high tower triggers which use energy deposition in BEMC towers as trigger threshold. To estimate their trigger efficiency, use the minimum-bias trigger as reference, which counts the total number of events. Then normalize the trigger events properly according to their prescale factor and luminosity.

The first step of analyzing the HT trigger event is to remove the random trigger benefit. When an event fired a HT trigger, it does not mean the trigger is fired by the signal, e.g. electrons, in the events. For example, one event has one electron which is not responsible for firing the trigger, while the trigger circuit noise goes beyond the trigger threshold, or a photon in the same events, or a background event fire the trigger. Then the trigger does not see the electron. We call this electron from random trigger benefit. This electron should be removed to avoid the uncontrollable condition, e.g. dirty beams, etc that make it hard for the systematic error estimation. There are different ways to remove the random benefit. One is to use the trigger simulator which mimic the real online configuration and figure out which tower is the high tower. We also developed a different way to use adc0 to simulate the trigger response. Adc0 is the offline adc value of the most energetic tower in a BTOW cluster and is responsible for firing HT triggers.

The left panel in Figure 3.18 shows the electron adc0 distribution in HT0 trigger events. There are two peaks: the first one is from random trigger benefit and the second one is from electrons firing the trigger. The trigger threshold can be clearly seen as ~193. The right panel shows the comparison between the p_T spectrum from using trigger simulator and from using adc0 > 193 cut. One can see the spectra obtained using this two methods agree with each other very well.

The usual way of estimating the trigger efficiency is to check the HT trigger bit in the minimum-bias events or normalize the minimum-bias event and HT trigger events according to their luminosities and then take the ratio. Since the minimum-bias events luminosity is too small to be used but the HT triggers in *d*+Au and *p+p* production, there is a lot of events from VPD trigger events which may starve of statistics in high p_T. We adopted the strategy of combining the trigger efficiency from both data and simulation.

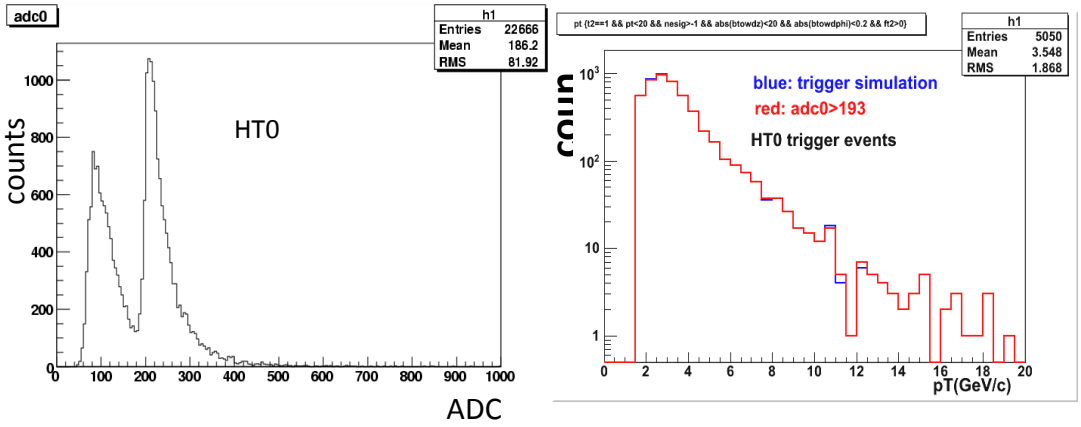

Figure 3.18 left panel: adc0 distribution for electrons from HT0 trigger. See text for detailed explanation. Right panel: comparison on p_T spectrum between using trigger simulator and using adc0 > 193 cut.

Figure 3.19 shows the normalized pT spectrum for HT triggers and minimum-bias trigger. The black histogram in the left panel of Figure 3.20 shows raw electron p_T spectrum and the red histogram shows the same spectrum after adc0>190 cut to mimic the HT0 trigger. The right panel shows the HT0 trigger efficiency calculated as the ratio of red over black histogram. The error bars are calculated using a simply Monte Carlo program analyzing the binomial distribution. The error in high p_T region is large where we rely on the tuned simulation to obtain the efficiency. At low p_T region, the disagreement is large.

We decide to use the efficiency from data at p_T <3.5GeV/c where the uncertainty is the data point statistical errors and using the one from embedding at p_T >3.5GeV/c where the uncertainty is from the turning procedure. The combined results are shown in Figure 3.22. Note that at p_T <2.5GeV/c, the efficiency is smaller than 5% and the result might not be reliable. We will drop the result in this p_T region when calculating the invariant cross section.

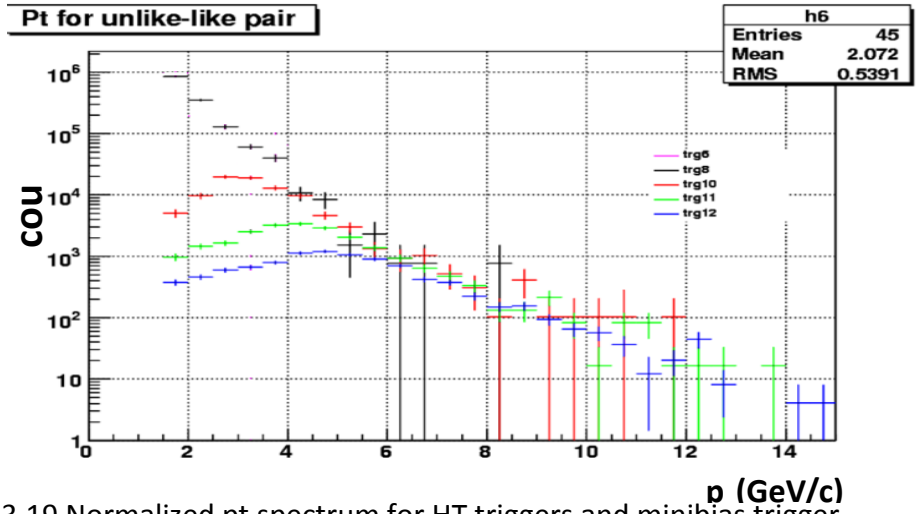

Figure 3.19 Normalized pt spectrum for HT triggers and minibias trigger

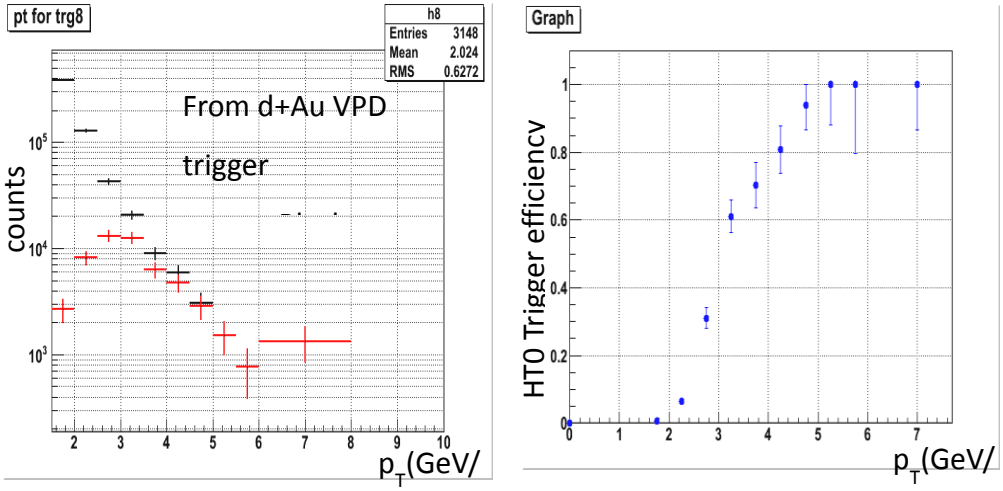

Figure 3.20 left panel: raw electron p_T spectrum from run08 VPD triggers (black) and spectrum after adc0>193 cut (red); right panel: trigger efficiency calculated as the ratio of red over black histogram in the left panel.

Figure 3.21 shows the comparison between efficiency obtained from data and simulation. The data and simulation agree with each other reasonable at p_T >3.5GeV/c.

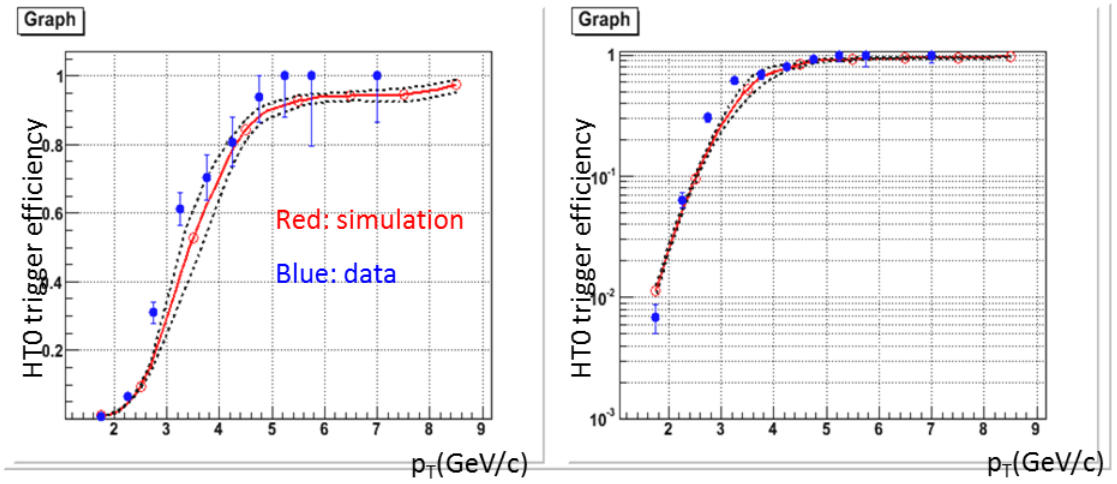

Figure 3.21 comparison between efficiency obtained from data (blue) and simulation (red). The right panel is the same as the left panel except in log scale. The dotted lines are from the uncertainty when tuning the embedding.

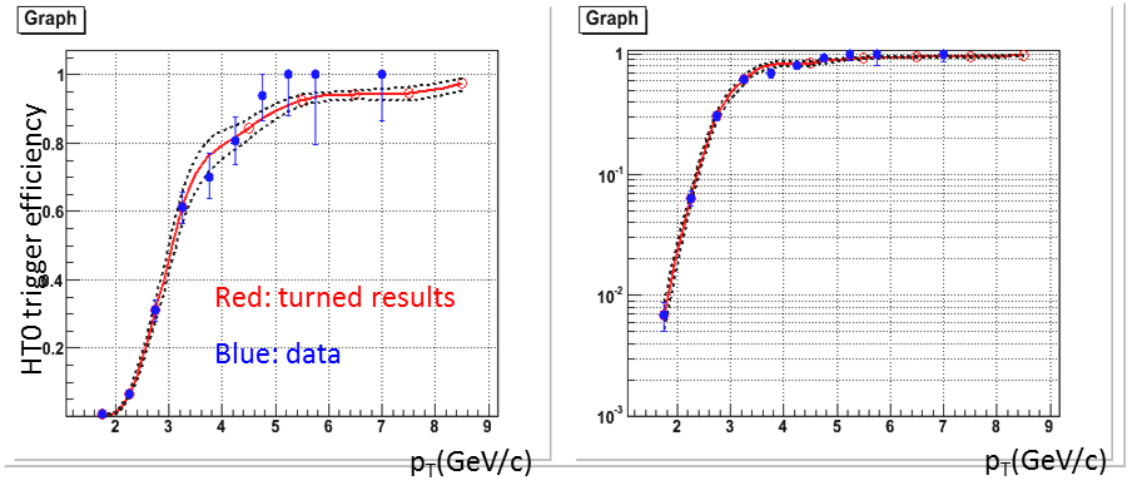

Figure 3.22 final trigger efficiency after combining result obtained from data and embedding. The right panel is the same as the left panel except in log scale. The dotted lines are from the uncertainty when tuning the embedding. Details see text.

3.7 Photonic Electron Reconstruction Efficiency

The photonic reconstruction efficiency is defined as the ratio of photonic electrons with reconstructed partners to the total photonic electrons. Since some photonic electron cannot be reconstructed due to low p_T or being out of TPC acceptance, this efficiency need to be estimated in order to unfold the total photonic electrons including those missing reconstructed partners. It is obtained using single gamma and single pi0 embedding which are the dominant source. To eliminate the low quality tracks causing the large fluctuation, we reject them by applying a cut on the on the radius of the 1^{st} TPC track point. Figure 3.23 shows photonic reconstruction efficiency vs. p_T with p_T(partner) >0.2 and 0.3GeV/c cut before and after rejecting tracks with the 1^{st} TPC point larger than 70cm. There are some differences for the two results. We decide to rely on the results with the 1^{st} TPC point cut since efficiency without this cut is still not very well under control.

One major concern is if the embedding can describe the p_T(partner) distribution from data. Figure 3.24 shows the p_T(partner) distribution from embedding (blue) and run08 *d*+Au VPD trigger events in each of the p_T(prim) bin. The data and embedding are normalized at p_T >0.2GeV/c since we know the tracking in simulation cannot do a good job in low p_T region. The comparison shows the embedding and data agree with each other very well at p_T(partner)>0.2GeV/c.

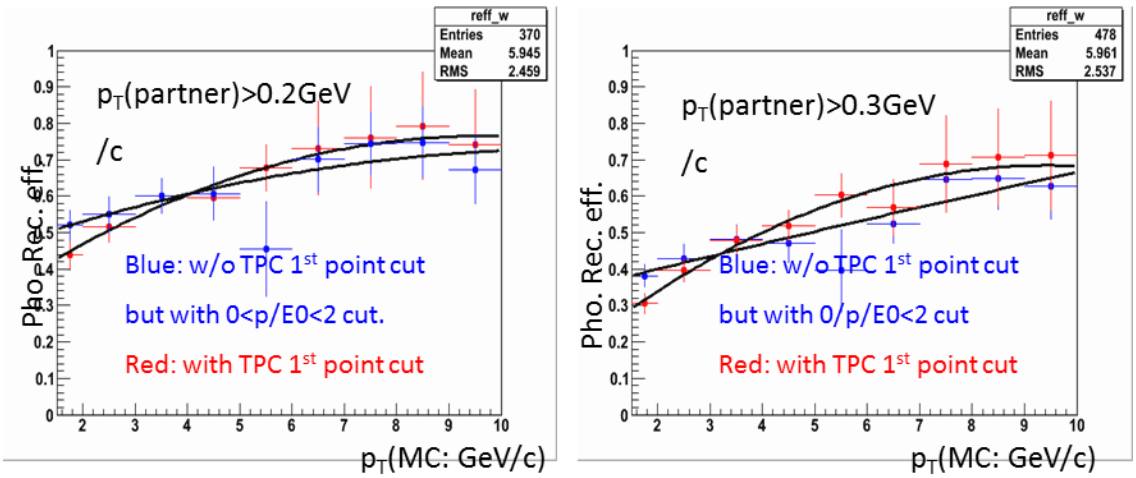

Figure 3.23 photonic reconstruction efficiency vs. p_T for p_T(partner)>0.2GeV/c (left) and 0.3GeV/c (right) with R(TPC 1st)<70cm cut (red) and without the R(TPC 1st) cut (blue). The result without the 1st TPC point has a 0<p/E0<2 cut. Results are weighted and p_T(partner) > 0.1GeV/c.

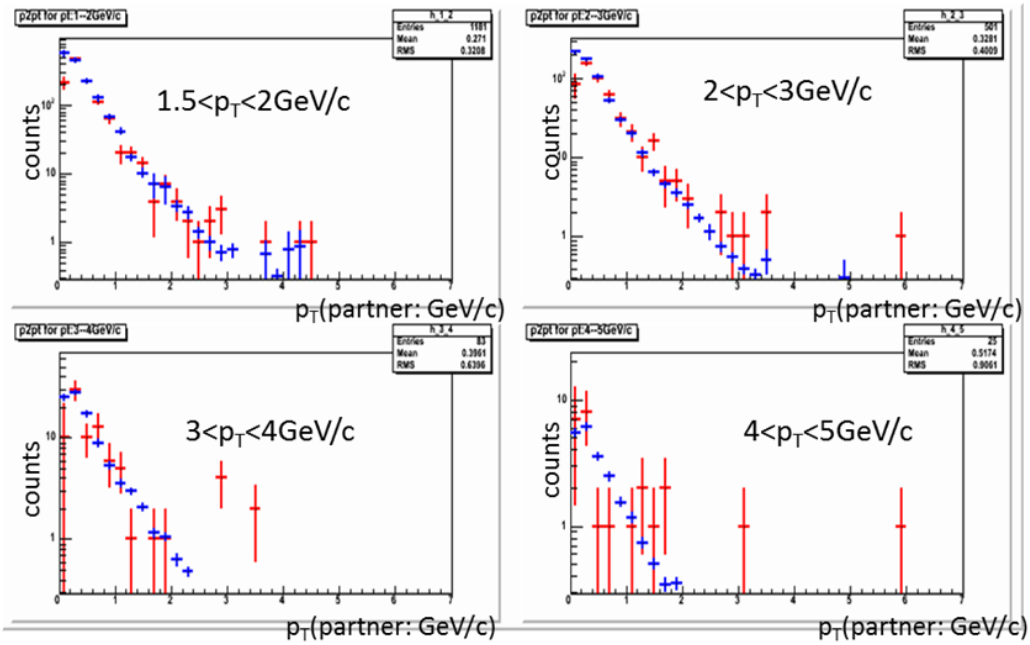

Figure 3.24 p_T(partner) distribution from run08 *d*+Au VPD trigger event (red) and embedding (blue) in different p_T(prim) bin. The embedding and data are normalized at p_T(partner)>0.2GeV/c

Figure 3.25 shows p_T(partner) distribution from embedding and HT trigger in run08 *p+p* collision. In this case, the embedding and data do not agree with each other well. There seems to be a bump in each p_T(prim) bin and is very significant in the low p_T region but gradually disappear in higher p_T region. This is from the trigger bias when two electrons in the same pair are so close that they share the same BTOW cluster. The green histograms are obtained by requiring two electrons in a pair share the same cluster. To do this, we apply the same association window cut for both electrons, i.e. 20cm in beam direction and 0.2 radian in R-phi direction. One can see the bump is dominated by the sharing effect. The red histogram is the distribution after removing the sharing effect. The embedding and the red data point are normalized at p_T >0.2GeV/c and the two seems to agree with each other well as in the comparison with the minimum-bias VPD trigger events.

Figure 3.26 shows the backward cumulative results of the p_T(partner) distribution which are obtained as following:

```
int nnn = h1[i]->GetNbinsX();
for(int ib = 0; ib<nnn; ib++) {
    c_h1[i]->SetBinContent(nnn-ib, h1[i]->Integral(nnn-ib-1, nnn));
}
```

So the first bin is from integral(0, 10GeV) and the last bin is from Integral(9.8, 10GeV/c). The data and embedding are normalized at p_T >0.2GeV/c in the corresponding derivative results. The error is obtained from the ROOT. The cluster sharing is removed. One can see the embedding and data agrees really well

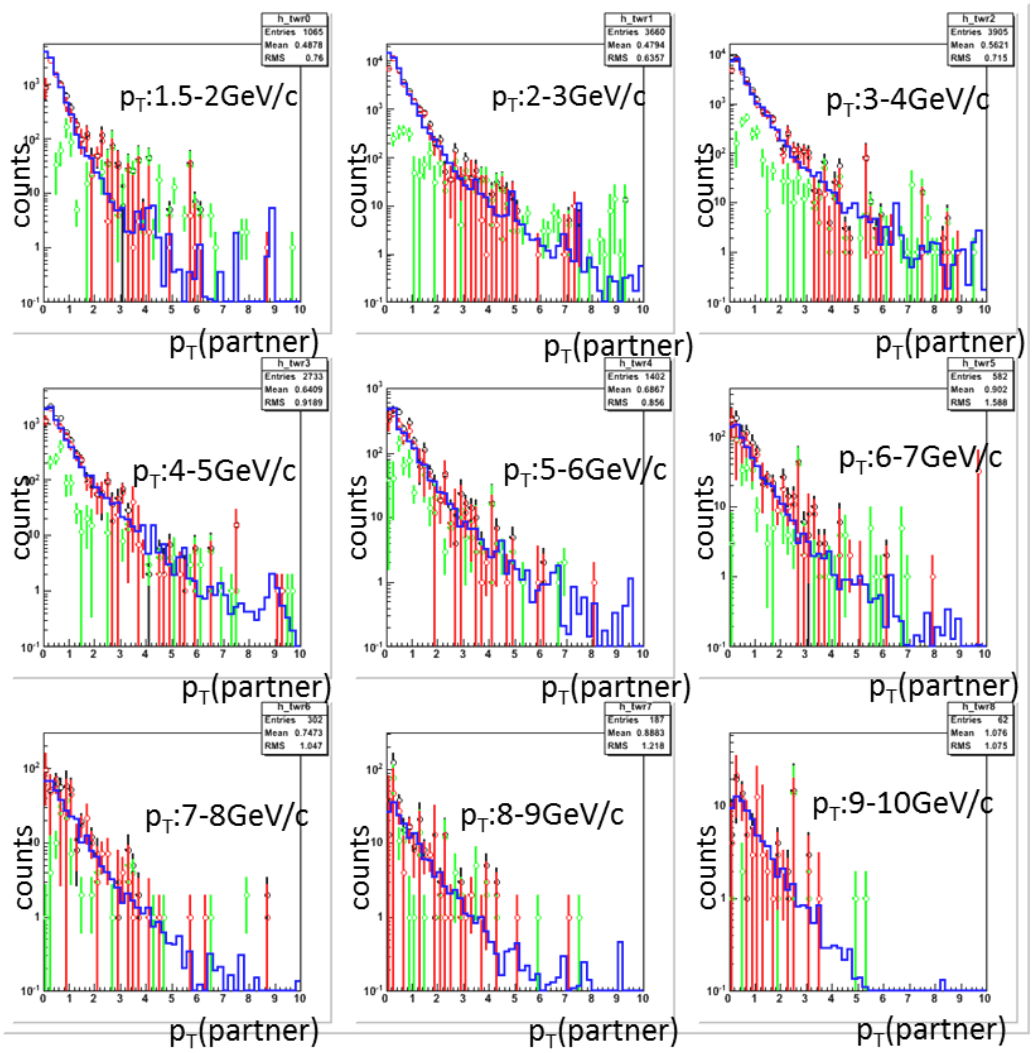

Figure 3.25 p_T(partner) distribution from run08 *p+p* HT trigger event (black) and embedding (blue) in different p_T(prim) bin. Green histogram is obtained by requiring the two electrons in a pair sharing the same cluster. The red histogram is the black histogram subtracting the green histogram. The embedding and red data point are normalized at p_T(partner)>0.2GeV/c.

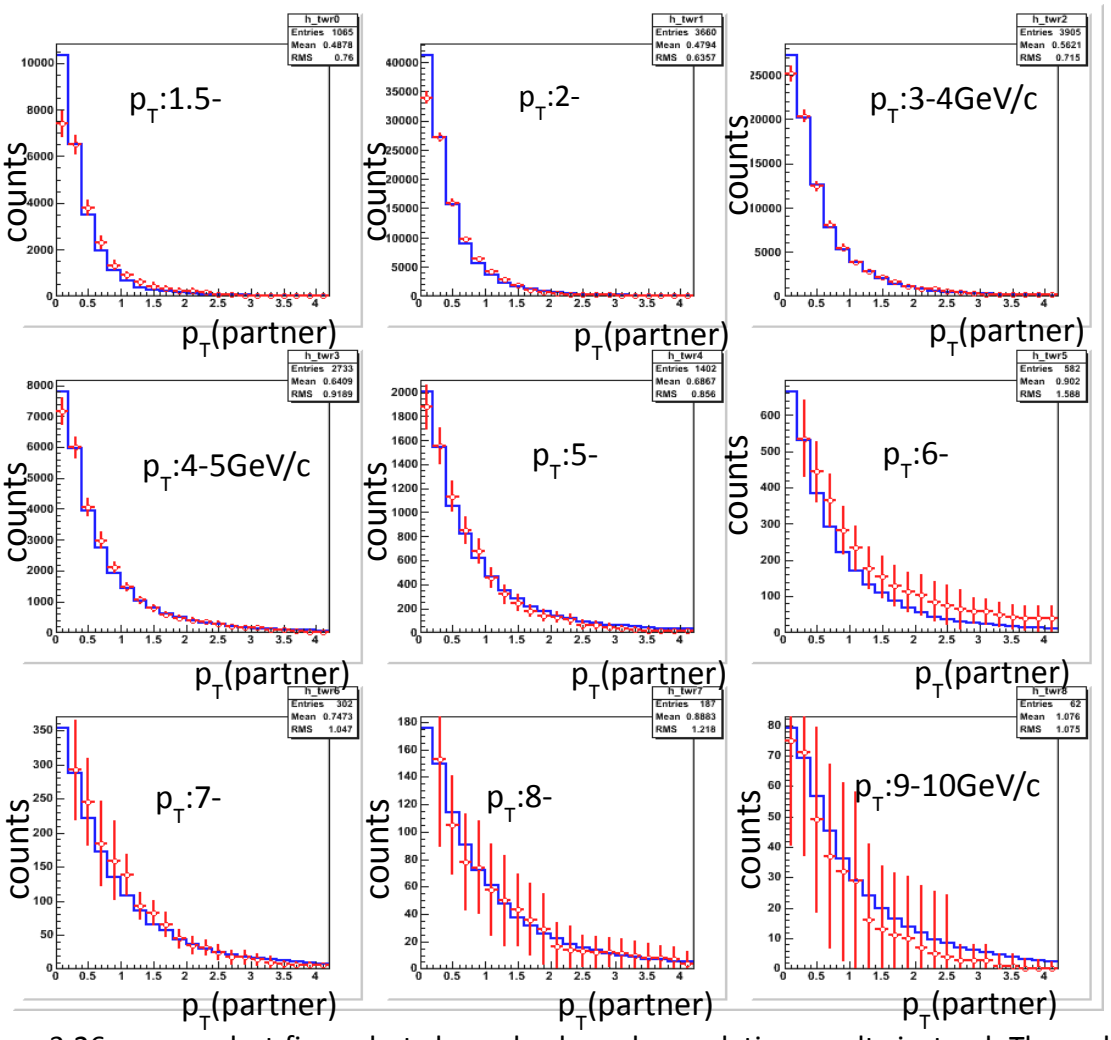

Figure 3.26 same as last figure but shows backward cumulative results instead. The red histogram is after removing the clustering sharing effect. The blue histogram is from run08 embedding. See text for details. The data and embedding are normalized at p_T(partner)>0.2GeV/c in the derivative plots.

The next question is how the clustering sharing will affect the photonic reconstruction efficiency. In one primary electron p_T bin, there are two types of primary electrons sharing with its partner:

Type#1: adc(primary) > adc(partner), i.e. primary electron is mainly responsible for firing the trigger. This is similar to the condition when p_T (primary) > p_T(partner), In this case, the p_T(partner) shape should be the similar as the minimum-bias trigger and the photonic reconstruction efficiency is the same as the minimum-bias result and can be directly calculated from embedding.

Type#2: adc(primary) < adc(partner), i.e. the partner electron is mainly responsible for firing the trigger. This is similar to the condition when p_T (primary) < p_T(partner). In this case, the p_T(partner) shape should present the trigger turn-on behavior. The photonic reconstruction efficiency should be lower than the minimum-bias events because trigger efficiency vs. p_T(partner) is not 100%. We need to take the trigger efficiency into account when calculating the efficiency from embedding.

If above understandings are correct, the following features will show up:

- in low p_T(prim) region, the trigger effect on p_T(partner) distribution is more significant than in high p_T(prim) region.

- When p_T(prim) > p_T(partner), the p_T(partner) shape should be the similar as that from the minimum-bias trigger

- when p_T(prim) < p_T(partner), the p_T(partner) shape should be present the trigger turn-on behavior

All these features are consistent with the result in Figure 3.25. Therefore, in the p_T(partner)<1.5GeV/c, the distribution should not be affected by the trigger since p_T(prim)>1.5GeV/c. By normalizing the p_T(partner) spectrum between embedding and data at p_T =0.2-1.5GeV/c before removing the sharing effect and do backward integral, one can estimate the fraction of type#2 primary electron at a certain p_T(partner) cut as shown in Figure 3.27. One can see, for p_T(partner)>0.2 or 0.3GeV/c, the embedding and data agree well with each other at p_T(prim)>2.0GeV/c. At p_T(prim)<2GeV/c, the data is ~10% higher than embedding and this can translate into a large effect on the cross section since the S/B ratio is small. In the final result, we dropped the data point at p_T <2.5GeV/c, therefore this effect will not affect us. With higher p_T(partner) cut, the difference between data and embedding can become larger since the cut is closer to the trigger bump. With p_T(partner)<0.2GeV/c cut, the embedding and data do not agree and leads to an inaccurate efficiency. Therefore, the p_T(partner)>0.2 or 0.3GeV/c would be

the best cut when reconstructing photonic electron pairs in data. We are not sure what happens in the 6< p_T(prim)<7GeV/c bin where the disagreement is large.

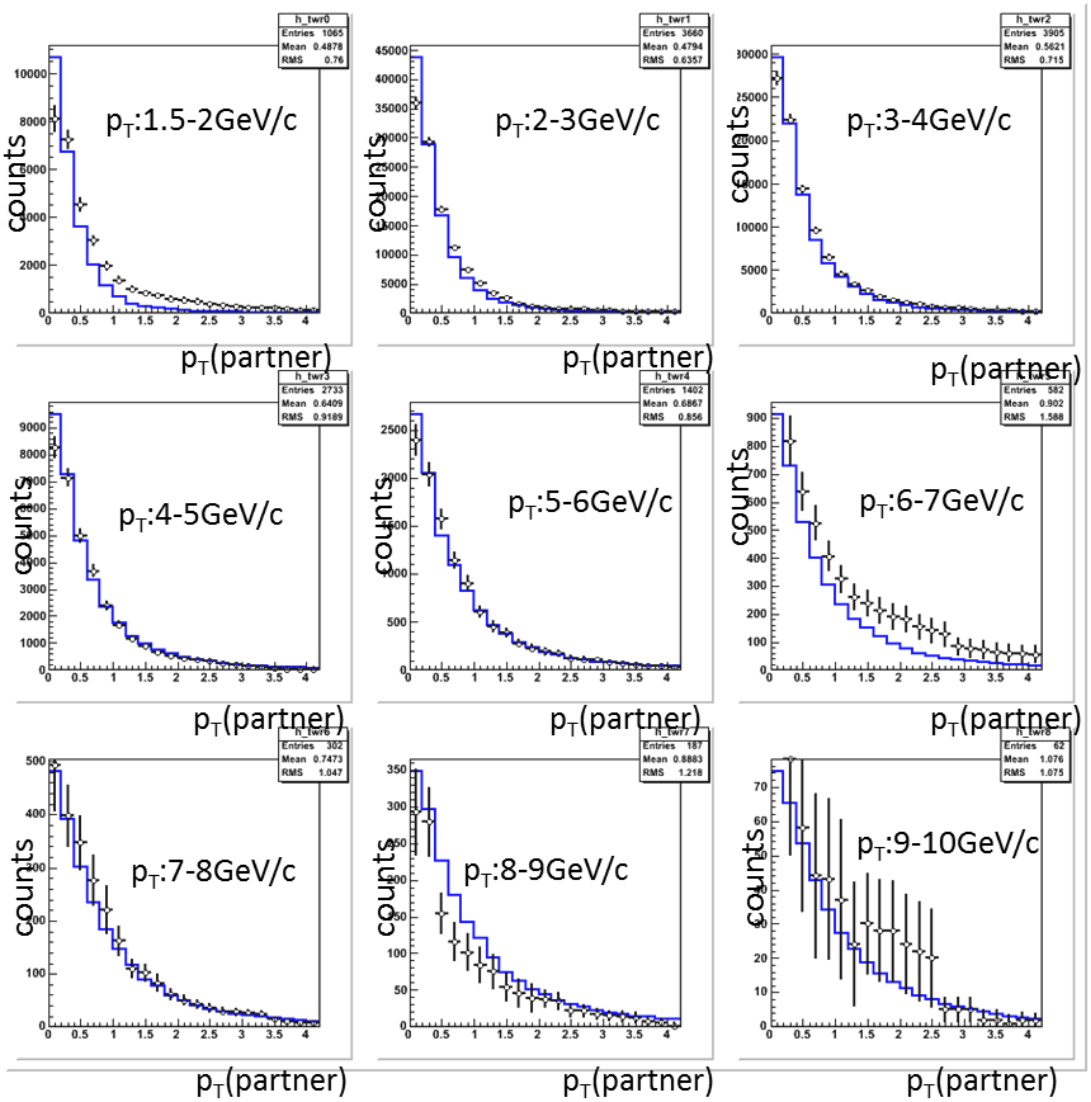

Figure 3.27 same as last figure but the embedding but the data is the one before subtracting the cluster sharing effect. The data and embedding are normalized at p_T =0.2-1.5GeV/c region in the derivative plots. See text for details.

The other cuts beside p_T(partner) that can affect the photonic reconstruction efficiency is the cuts on number of fit point for partner tracks (nfit) and the ratio of nfit over the number of possible point for partner tracks.

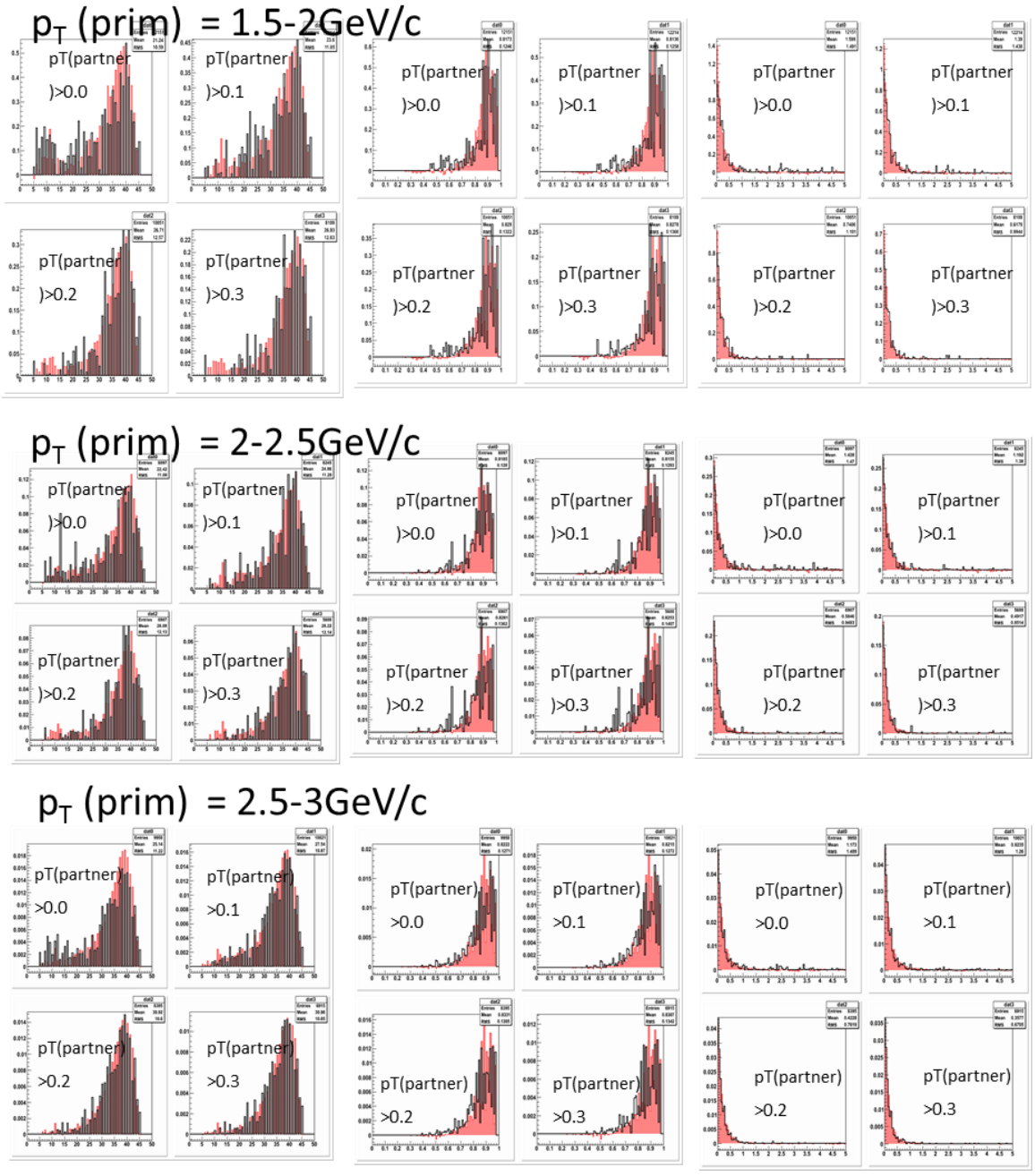

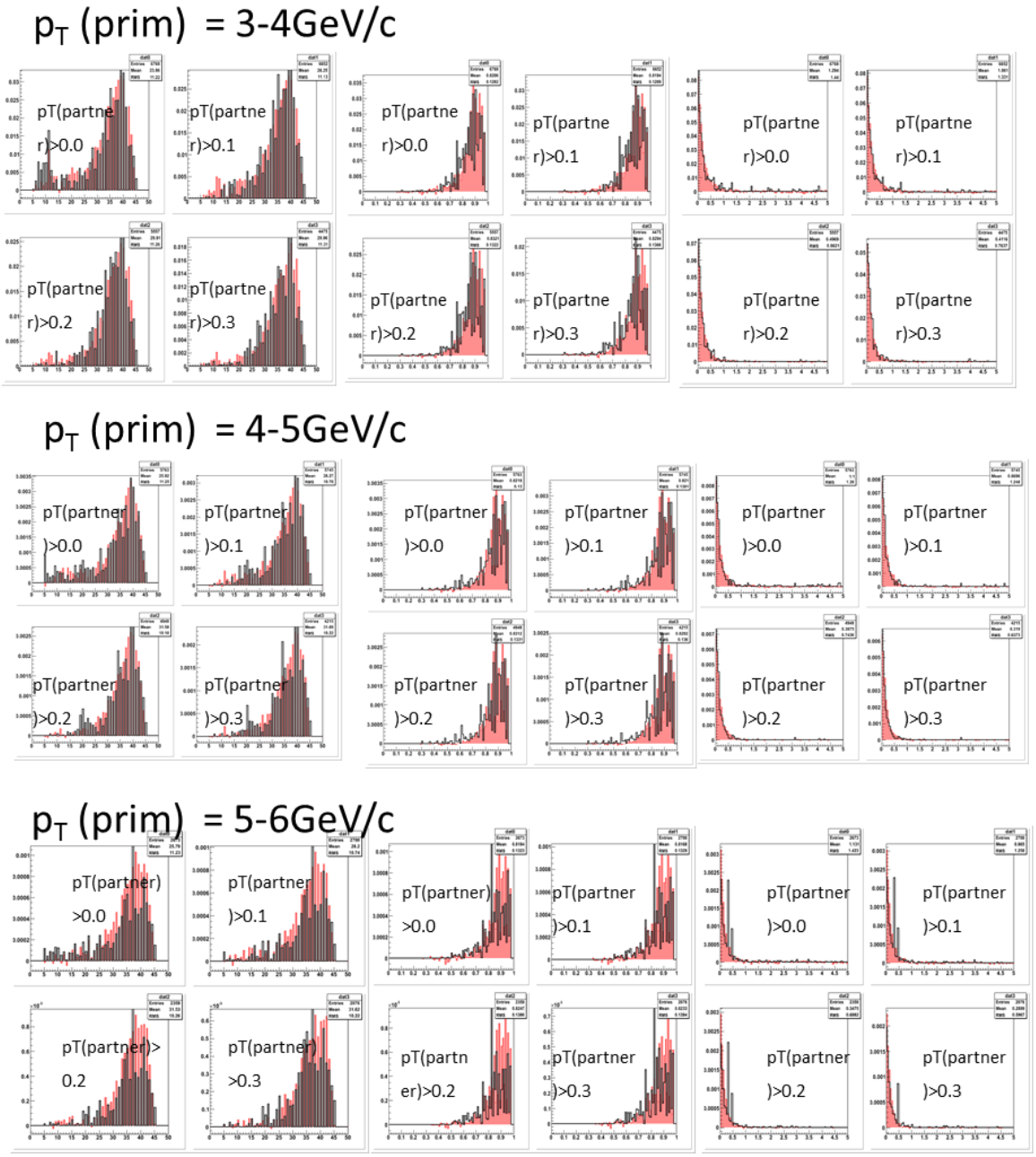

Figure 3.28 Comparison between partner nfit (left), nfit/nmax (middle) and electron pair DCA (right) distribution for each primary electron p_T bin and for different p_T(partner) cut between embedding and data.

Figure 3.28 shows the comparison on partner electron nfit, nfit/nmax and pair DCA distribution between embedding and data with different p_T(partner) cut in different primary electron p_T bin. The data are from pure photonic electron obtained from unlike-likeSign. Overall the embedding can describe the data very well.

Figure 3.29 shows the quantitative comparison on the efficiencies for cuts on partner nfit, nfit/nmax and pair DCA. The efficiency is calculated as the ratio of total counts after these cuts over that before these cuts. One can see the amount of discrepancy between embedding and data depend on the primary electron p_T as well as the p_T(partner) cut. The p_T(partner)>0.3GeV leads to the smallest discrepancy. This difference is used to correct the photonic reconstruction efficiency as shown in Figure 3.30 left panel. The right panel in Figure 3.30 shows the relative change on the raw NPE yield before and after the correction.

Figure 3.31 shows the photonic reconstruction efficiency as a function of p_T. Results from gamma coversion and pi0 Dalitz decay are plotted. The uncertainty due to the limited embedding statistics is estimated in the following. All the data points are moved by 1-sigma up and down together and then the spectrum is fitted with the pol2 function. For each p_T bin, the larger one of the difference between the fitting result on the moved and not-moved data point are used as the uncertainties. The dashed line in the figure shows the fitting curve for the moved data points. Currently this is the main source of uncertainty for photonic reconstruction efficiency.

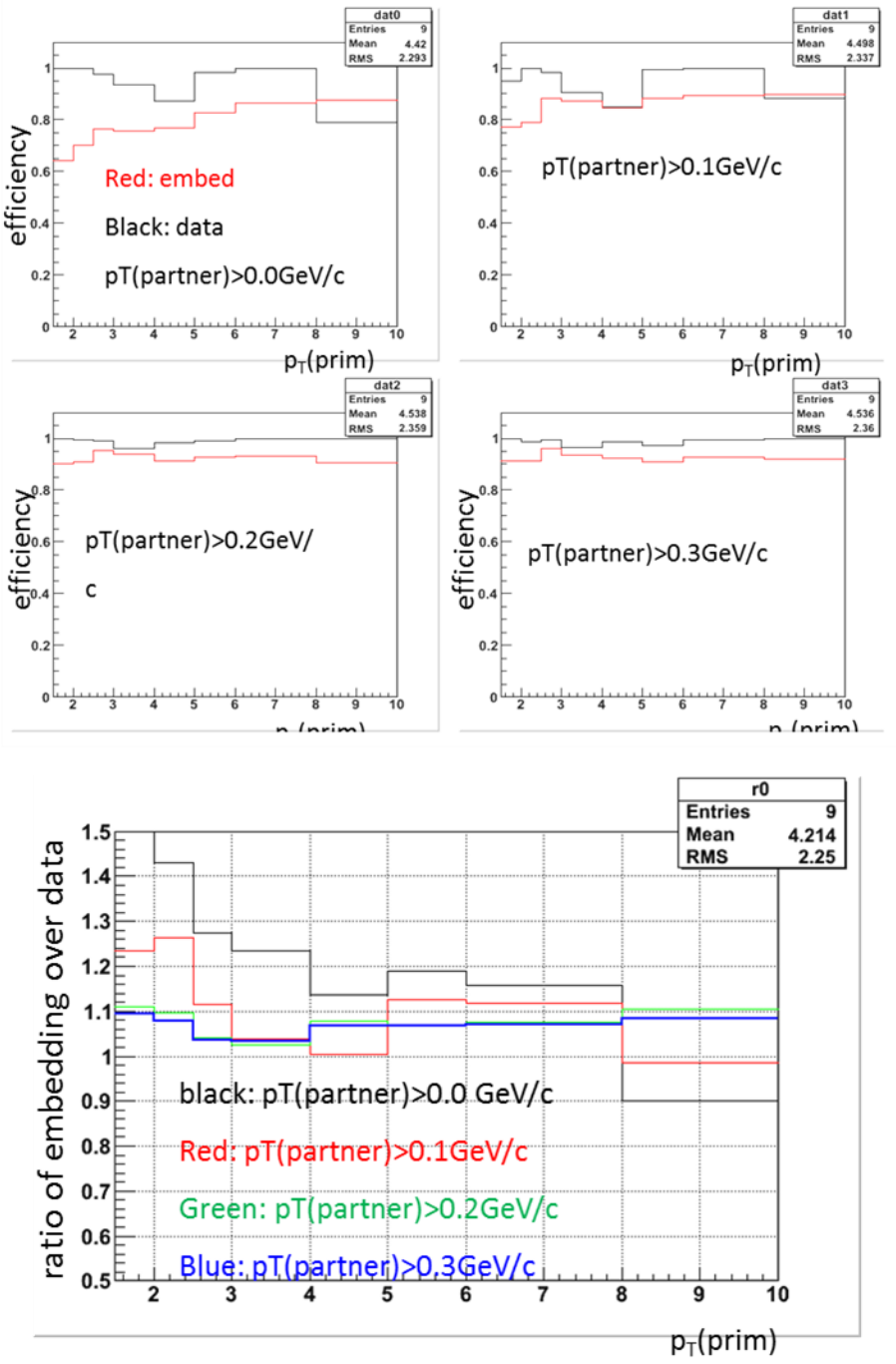

Figure 3.29 upper: Comparison on the efficiencies for cuts on partner nfit and nfit/nmax, pair DCA with different pT(partner) cut as a function of pT(prim) between embedding (red) and data (black); lower: ratio of efficiency from embedding over efficiency from data as a function of pT(prim) with different pT(partner) cuts.

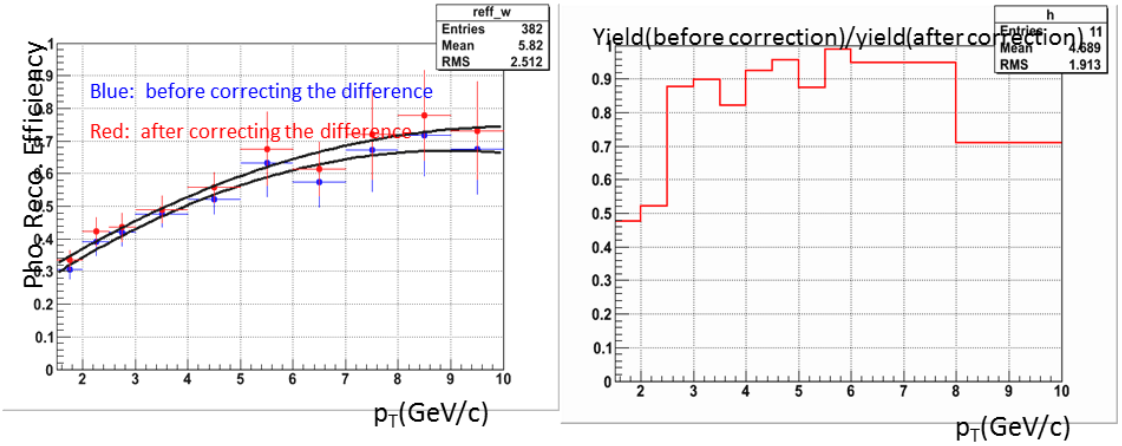

Figure 3.30 left: photonic reconstruction efficiency before and after correcting the different between embedding and data on the partner nfit, nfit/nmax and DCA (pair) distribution. Right: ratio on the raw NPE yield before the correction over that after the correction.

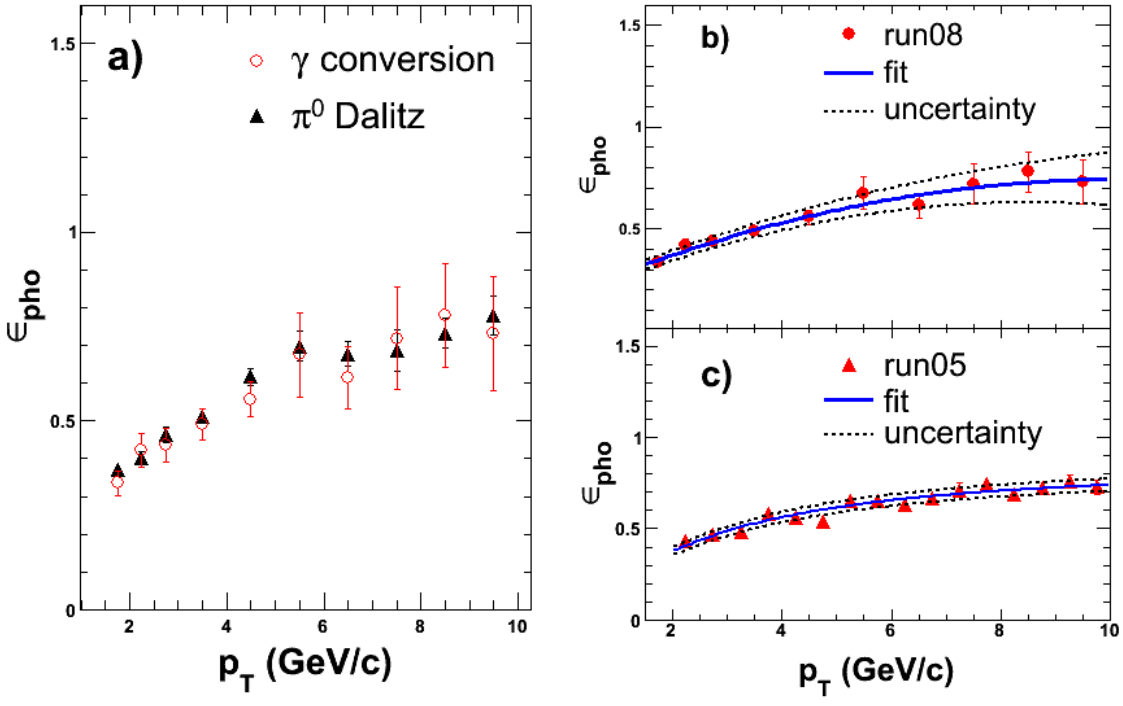

Figure 3.31 pho.reco.efficiency with uncertainties from limited embedding statistics.

3.8 Electron Identification Efficiency Estimation from data

We developed a method to calculate the electron identification efficiency directly from data using pure photonic electron. The efficiency for one cut is calculated by taking the ratio before and after applying the specific cut while all the other electron identification cuts are applied. Note that one needs to subtract the contribution from like-sign pairs to get the pure electron results. There are possible correlations among cuts, for example, the association window cuts for BTOW and p/E0 cut for BTOW. To avoid this, the efficiencies from the all BEMC cuts are calculated together. Figure 3.32 shows the breakdown of the electron identification efficiency vs. p_T. Before reaching the plateau, the efficiency increase at higher p_T mainly due to the inefficiency of BSMD on low p_T electrons. Note that the efficiency is estimated using HT0 trigger only since the combined trigger is essential a HT0 trigger with more statistics at high p_T and some cuts, e.g. p/E0 cut is different for different HT trigger.

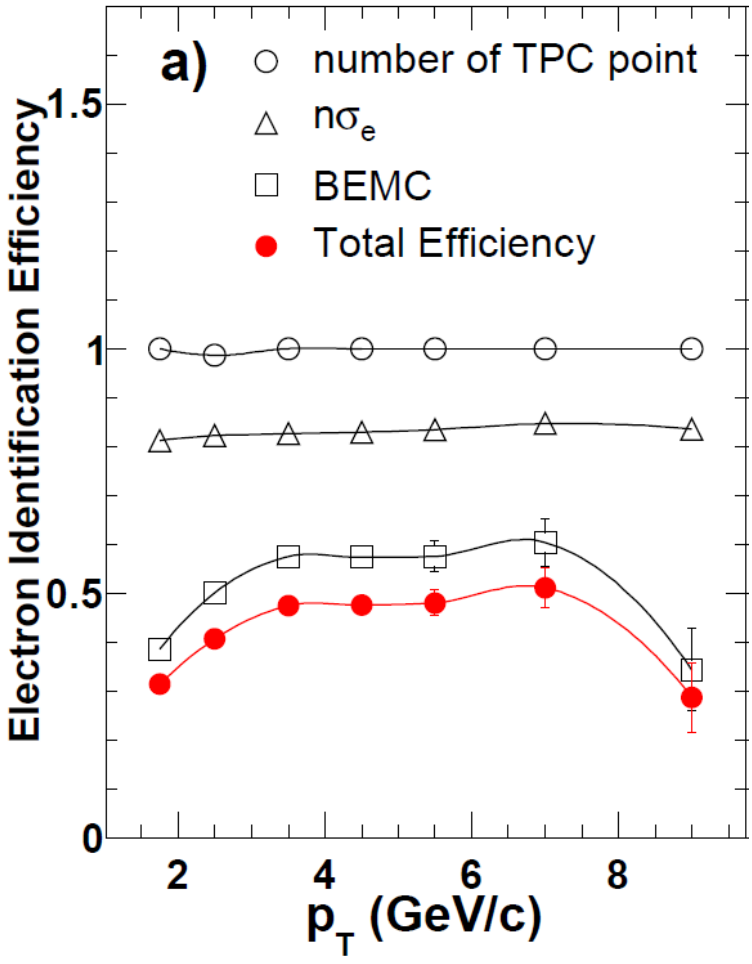

Figure 3.32 Efficiencies of the cuts on number of TPC points (open circles), *nσe* (open triangles) and BEMC (open squares) in Run2008.

3.9 Ratio of Non-photonc over Photonic Electron Yields

Figure 3.33 left panel shows the ratio of non-photonic over photonic electron yield as a function of p_T with p_T(partner)>0.3GeV/c from run08 and UCLA run05 analysis. The large

difference comes from large difference in material budget in front of TPC. The error bar is calculated as the following:

nph/ph = inc_raw*purity/(ph_raw/reff) - 1 = reff*purity/(ph_raw/inc_raw) - 1,

where inc_raw, ph_raw are the raw inclusive and photonic electron yield after combining the 3 high-tower triggers, reff is the photonic reconstruction efficiency.

Therefore,

err(nph/ph) = reff*purity*err_ph_over_inc/pow(ph_raw/inc_raw,2),

where err_ph_over_inc is calculated error of ph_raw/inc_raw that is calculated through monte carlo. Note that ph_raw/inc_rawdo not following binomial distribution since

$$ph\_raw/inc\_raw = \frac{ph(HT0) * ps0 + ph(HT1) * ps1 + ph(HT2) * ps2}{inc(HT0) * ps0 + inc(HT1) * ps1 + inc(HT2) * ps2}$$

Where ph(HT*) is the photonic yield from HT* trigger before being rescaled back, inc(HT*) is the inclusive yield from HT* trigger before being rescaled back. ph(HT*)/inc(HT*) following binomial distribution but ph_raw/inc_raw does not.We obtained distribution of ph_raw/inc_raw through the following MonteCarlo:

Finally fit the distribution with Gaussian and take the sigma as the uncertainty.

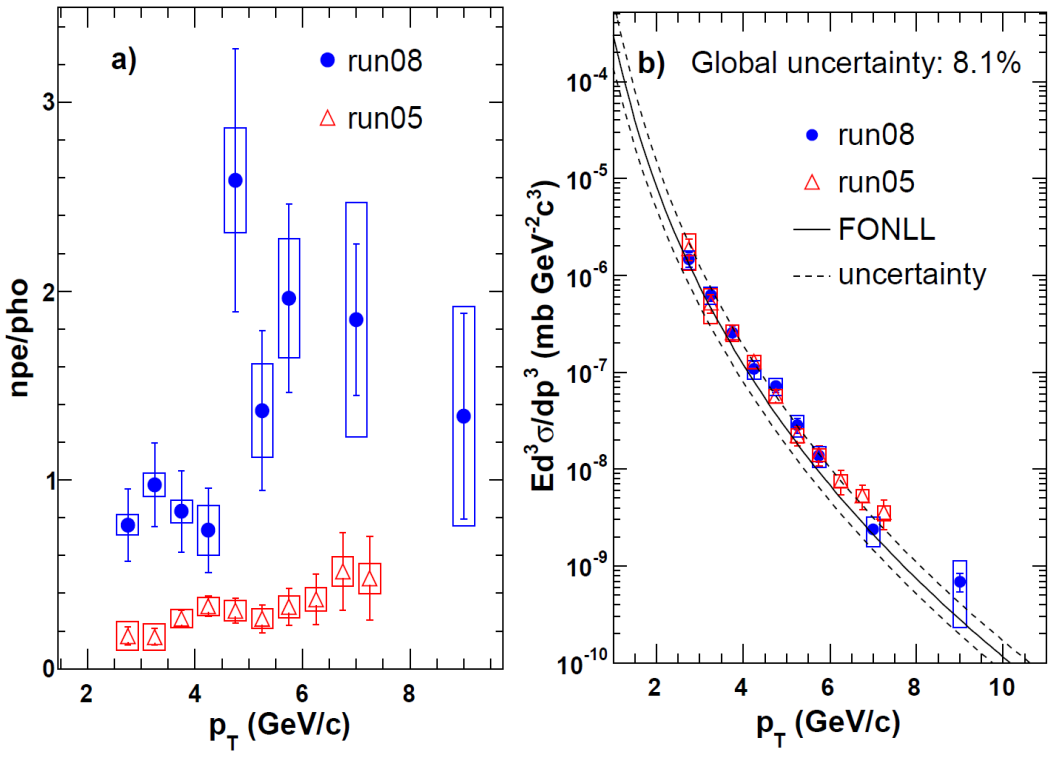

Figure 3.33 (left) Ratio of non-photonic to photonic electron yield from the Run2008 (closed circles) and the Run2005 (open triangles) analyses. The error bars and the boxes represent statistical and systematic uncertainty, respectively. (right) NPE invariant cross section ($\frac{e^+ + e^-}{2}$) from run08 and run05 analysis.

3.10 Invariant Cross Section in *p+p* collisions

The following equation is used to calculate the invariant cross section:

$$B\frac{1}{2\pi P_t}\frac{d\sigma}{dydP_t}\bigg|_{y=0} = 1.49\cdot 10^{-3} mb \cdot \frac{1}{2\pi P_t \cdot \Delta y \cdot \Delta P_t} \cdot \frac{N_e(HT0@|zvtx|<30cm)}{N_{evt}(HT2@|zvtx|<30cm)} \cdot \frac{1}{\varepsilon_{trg}\cdot\varepsilon_{acc}\cdot\varepsilon_{eID}\cdot\varepsilon_{BBC}}$$

, where ε_{trg} and ε_{eID} are trigger and eID efficiency, ε_{accp} = 0.86, independent of p_T, ε_{bbc} = 0.866, 1.49e-03 mb is the HT2 cross section, N_e(HT0@|zvtx|<30cm) is number of HT0

non-photonic at |zvtx|<30cm and N_{evt}(HT2@|zvtx|<30cm) is number of HT2 events at |zvtx|<30cm. To avoid the trigger bias when counting the luminosity at |Zvtx|<30cm, we rely on VPD and found the fraction of collisions at |Zvtx|<30cm is ~43%. Therefore, N_{evt}(HT2@|zvtx|<30cm) = 43%× N_{evt}(HT2 w/o Zvtx cut). The efficiencies not mentioned in the equation are the one from phi cut (78%) and from R(TPC 1^{st}) < 70cm cut (88%) .

The following is the summary of all relative systematic errors:

- <u>bin-by-bin errors.</u>
    A. p_T dependence of single electron acceptance
    B. Bin shift correction
    C. Momentum smearing correction
    D. Purity estimation
    E. trigger efficiency
    F. eID efficiency estimation from data including BSMD status table
    G. Photonic reconstruction efficiency.
    H. Different trigger efficiency between NPE and PHE
    I. Light vector meson decay uncertainty

- <u>scaling error that move all point up and down together (total: 18.5%)</u>
    1. Acceptance : 8%
    2. Cut on TPC 1^{st} point: 2.3%.
    3. HT2 cross section w.r.t. BBC: 2.3%

4. Run-by-run variance for trigger + tracking + acceptance: 15%
5. Error from combining all the triggers: 5%
6. BBC cross section and efficiency uncertainty: +/-14%/sqrt(12)=8.1%.

Figure 3.33 right panel shows the invariant cross section from Run2005 and Run2008 analysis. They are consistent with each other despite the large difference in photonic background. For more precision, we combine the measurements from Run2005 and Run2008 (See 0 for details). Figure 3.34 (a) shows the non-photonic electron invariant cross section ($\frac{e^+ + e^-}{2}$) from this analysis and the published result at RHIC. One can see our new result and PHENIX results are consistent with each other. Note that the 8.1% global scale uncertainty comes from BBC cross section. Figure 3.34 (b) shows the ratio of invariant cross section from different dataset over FONLL prediction. These plots show more clearly the comparison among different datasets.

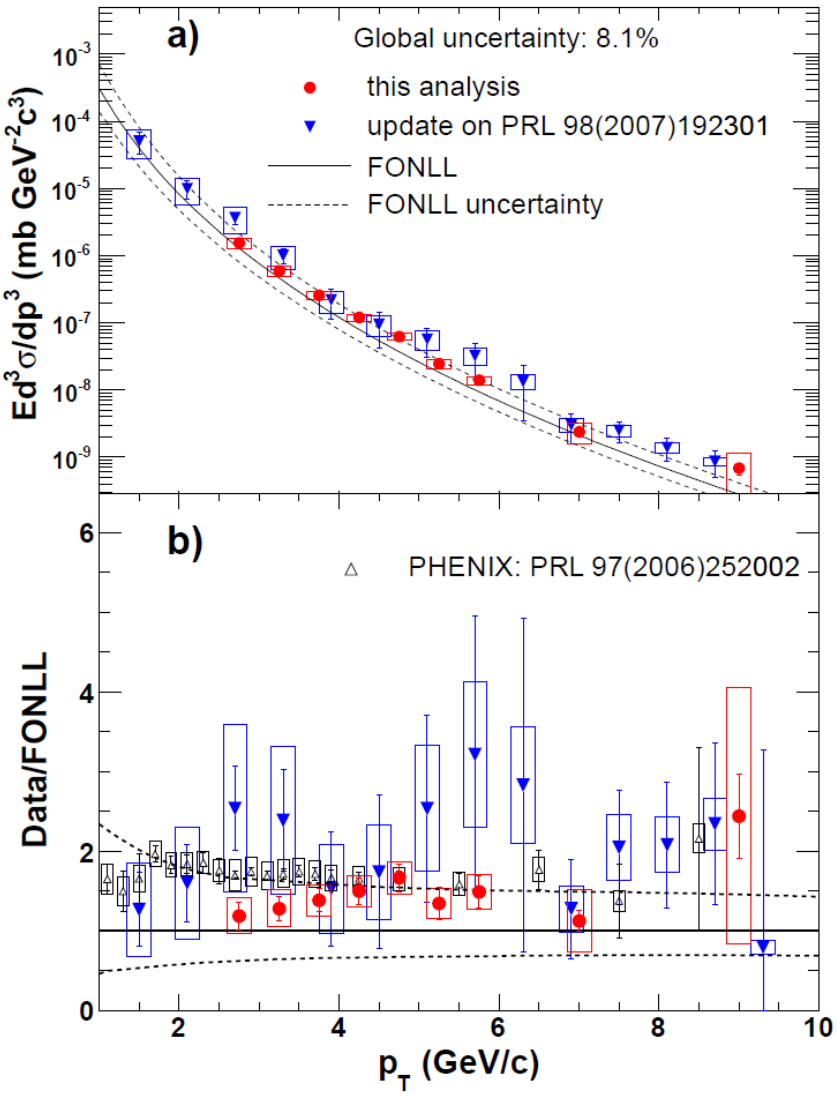

Figure 3.34 (a) Invariant cross section of non-photonic electron production (*e*++2) in *p* + *p* collisions from this analysis (closed circles) after combining results from Run2005 and Run2008. The published STAR re-sult [16] (closed triangles) is also shown. (b) Ratio of dataover FONLL [2] from all measurements at RHIC including PHENIX results [17] (open triangles).

4. HIGH P_T NON-PHOTONIC ELECTRON PRODUCTION IN AU+AU COLLISIONS

In early STAR non-photonic electron analysis in Au+Au collisions, same error as in *p+p* collisions was made. The photonic electron reconstruction efficiency was overestimated by about 10% leading to a factor of two overestimate on the non-photonic electron invariant yield. After correcting the error, we recalculated the R_{AA} as shown in Figure 4.1. Compared to the original result shown in Figure 1.2, the statistical uncertainty is significantly increased mostly due to the fact that the actual signal yield decreased by a factor of two. On the other hand, since the same problem leads to a factor of two error in the invariant yields in both Au+Au and *p+p* collisions, this factor is mostly cancelled out when calculating R_{AA}. The mean value of R_{AA} is thus not significantly changed. Up to this point, the discrepancy between STAR and PHENIX non-photonic electron measurements that had been puzzling the field for years was completely solved.

The non-photonic electron measurements at RHIC have triggered a lot of theoretical efforts. The radiative energy loss models, for example, DGLV and BDMPs [18] models, describe very well the light flavor hadron suppression in the medium. However, as shown in Figure 4.1 the DGLV (model I in the figure) cannot describe the non-photonic RAA measurement. The BDMPS (model II in the figure) predicts a lower RAA value but is

disfavored by the data. It is interesting that prediction (V) which considers only the charm quark contribution can very well describe the experimental results. This illustrates the importance of disentangling the charm and bottom quark contribution in the experimental results. After that people realize the importance of including elastic energy loss in addition to radiative energy loss for heavy flavor particles. In other words, the energy of heavy quarks can be transferred to the surrounding medium constituents via elastic collisions. This is significant for relatively slow moving particles. After including the elastic collision energy loss, DGLV (model III in the figure) predicts a larger suppression factor but is still disfavored by the data. The hadron resonance model based on the relativistic Langevin simulation (model IV in the figure) [19] assumes only elastic energy loss predicts a suppression factor as large as the BDMPS model. Another model [20] which is not shown in the figure assumes the heavy flavor mesons can be formed inside the hot and dense medium, and the observed large suppression of the heavy flavor meson production comes from the dissociation process when the meson interact with the medium constituents. One feature of the model is that the predicted suppression of bottom mesons at high p_T is similar or larger than that of charm mesons.

Therefore disentangling the charm and bottom meson contribution in the experimental results is important for understanding the energy loss mechanism. With the coming STAR upgrade, these measurements become possible.

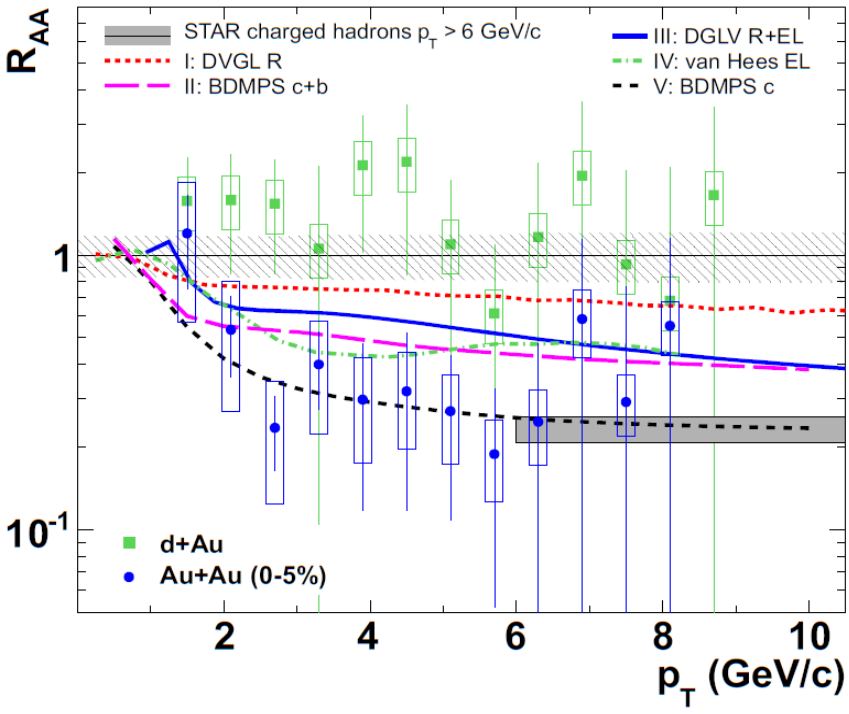

Figure 4.1 STAR measurements of non-photonic electron nuclear modification factor R_{AA} as a function of p_T in *d*+Au (green closed circles) and the most central 5% Au+Au collisions (blue closed circles) at 200 GeV using Run-2003 data after correcting the error. The error bars (boxes) are statistical (systematic) uncertainties. The shaded area at R_{AA}=1 represents the normalization uncertainty common to all data points. The band at R_{AA}~0.2 represents the STAR charged hadron measurement at p_T > 6 GeV/*c*. Various curves represent predictions from various models. Erratum: STAR Collaboration, Phys. Rev. Lett. 106, 159902(E)-1-3 (2011).

5. LOW P_T NON-PHOTONIC ELECTRON ANALYSIS IN *P+P* COLLISIONS

Compared to Run2008, Run2009 has different trigger setup and more importantly most of the STAR MRPC TOF is installed. This provides a good opportunity to measure non-photonic electron spectrum at low p_T region (0.2GeV/c< p_T <2GeV/c) by applying TOF electron identification cut.

5.1 Trigger Setup

Table 4.1.1 shows the trigger setup of Run2009 at 200 GeV *p+p* collisions. It mainly uses VPD as minimum-bias trigger, and three HT triggers (HT0, HT1, HT2) with different online ADC region in different runs. The trigger configuration is Different from Run2008. In order to remove the possible overlapping from different HT triggers during trigger combination, one event is flagged from only one HT trigger. For example, an event with online ADC>18, which can pass both HT1(15<ADC threshold≤ 18) and HT2(ADC threshold >18), it will be flagged as from HT2, since the HT1 setup only accept events passing HT1 and not passing HT2.

Table 5.1 Trigger setup of Run2009

Name	Trigger id	Lum [pb^{-1}]	P^4 L [pb^{-1}]	Nevents [M]	First Run	Last Run
HT0*VPDMB*!HT1		0.066	0.005	1.139	10114041	10125027
HT0*VPDMB*!HT1	240550	0.066	0.005	1.139	10114041	10125027
HT0*VPDMB*!HT2		1.807	0.163	36.137	10125064	10180030
HT0*VPDMB*!HT2	240570	1.807	0.163	36.137	10125064	10180030
HT1*VPDMB		0.092	0.007	0.270	10114041	10125027
HT1*VPDMB	240560	0.092	0.007	0.270	10114041	10125027
HT2*VPDMB		3.179	0.276	3.220	10114071	10180030
HT2*VPDMB	240540	3.179	0.276	3.220	10114071	10180030
HT3		23.141	2.008	7.750	10112099	10180030
HT3	240530	23.141	2.008	7.750	10112099	10180030
VPDMB		0.012	0.001	311.873	10113066	10180030
VPDMB	240020	0.000	0.000	6.718	10113066	10114040
VPDMB	240025	0.012	0.001	305.155	10114041	10180030

5.2 HT triggers Combination

Compared to Run2008, the technique of trigger combination is simplified, since there is no event overlapping. In different runs with different trigger setup, we simply add the spectrum from different minimum-bias and HT triggers together, after normalized according to their prescale factor and online ADC(DSM) threshold. For example, in single electron production:

Combined spectrum = VPDMB (ADC<=11)*ps0 +

HT0*VPDMB*!HT2(11<ADC<=18)*ps1 + HT2*VPDMB(ADC>18)*ps2.

where ps0, ps1 and ps2 are prescale factors for HT0, HT1 and HT2, respectively.

During Run2009, there are three different run configurations with different trigger mixing. The trigger combination algorithm in each of the run configuration is listed in

.

To check the trigger combination algorithm, Figure 5.1 shows the combined HT inclusive and photonic electron spectra. The black histogram is from VPD minimum-bias trigger. The red histogram is from high tower triggers. At the trigger efficiency plateau region (p_T = 4 GeV/c), the two spectra are consistent with each other as expected. As a further check, we apply the trigger threshold on the VPD spectra and obtain the blue histogram. The blue histogram and the red histogram agree with each other very well.

Table 5.2 shows the detailed trigger combination algorithm for different runs.

Run config.	11(2.6GeV)<ADC≤ 15 (3.6GeV)	15(3.6GeV)<ADC ≤18(4.3 GeV)	18(4.3GeV)<ADC	Trigger combine
Low	HT0*VPDMB *!HT1 (t3)	HT1*VPDMB (t4)	HT1*VPDMB (t4)	VPD (ADC<=11)+ t3 + t4
High	None	None	HT2*VPDMB (t2)	VPD (ADC>18)+t2
Single	HT0*VPDMB *!HT2 (t5)	HT0*VPDMB *!HT2(t5)	HT2*VPDMB (t2)	VPD (ADC>11)+t2 +t5

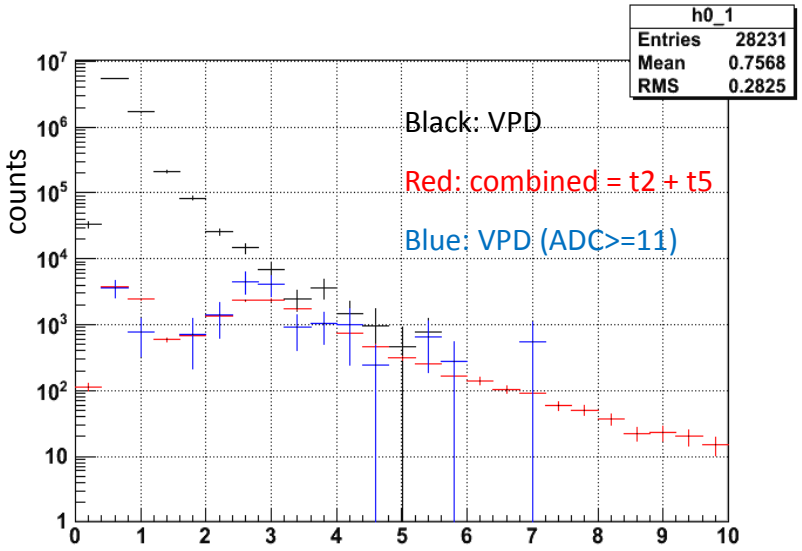

Figure 5.1 combined HT and VPD spectrum for inclusive electrons.

5.3 Electron identification cuts

Track Quality cut:

- Number of hits to fit the track, i.e. nfit>20 && nfit/nmax>0.52 &&
- Global DCA (dcaZ<6cm, dca2D<1cm)

Electron Identification cut:

p_T>2GeV/c:

- 0<p/E<2
- |btowdphi|<0.1 & |btowdz|<20
- |bsmdedphi|<0.15& |bsmdedz|<10
- |bsmdpdphi|<0.1 & |bsmdpdz|<20
- $n\sigma_e$ > -1
- SMD multiplicity cut: nsmde>1 & nsmdp>1
- Remove beta!=-999 cut after UCLA meeting

p_T <=2GeV/c

- TOF cut: |1-1/β |<0.03
- $n\sigma_e$ > -1

Other cut:

- mass3D<0.24GeV
- |pairDCA|<1.0cm, where pairDCA is the DCA between electrons in a pair
- The Global partner of the pair :
  - 3.0e-6<dE/dx<5.0e-6

- p_T >0.3GeV/c
- No other cut including the EMCal association cut.

Generally, at p_T >2GeV/c, Run2009 electron identification applies similar cuts as Run2008, like p/E, BEMC association window (shown in Figure 5.2, Figure 5.3 and Figure 5.4). While at p_T <2GeV/c, since the efficiency of BEMC is too low, we use TOF (|1-1/β |<0.03) and TPC ($n\sigma_e$ > -1) cuts to identify electrons. At such low p_T region, due to the different mass, charged particles can be separated by measuring their velocity (β). Figure 5.5 shows the 1/β vs. p for electron, pion, kaon and proton. Clearly the electron band is around unity and merged with pion and kaon band as p_T increases. Here we apply TOF PID cut, |1-1/Beta|<0.03, to reject slow hadrons in p_T < 2Gev/c region. After that, $n\sigma_e$ and purity estimation will further eliminate fast pion and kaon contamination and achieve pure electron sample.

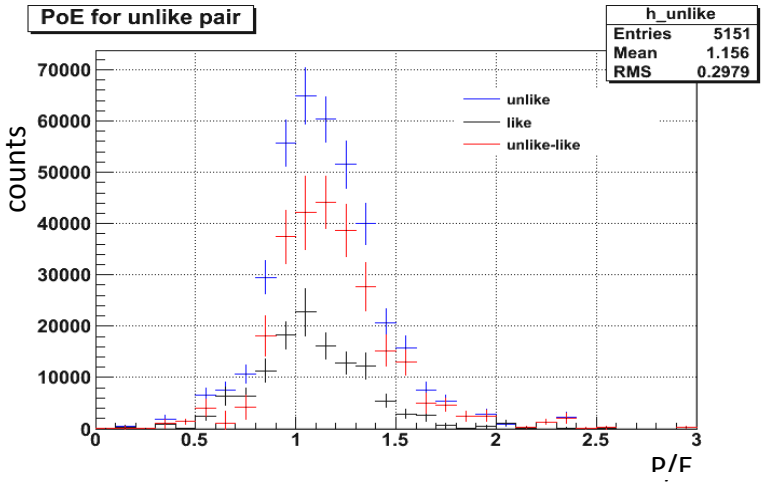

Figure 5.2 Combined p/E spectrum for unlike-like photonic electron. Use 0< P/E < 2 cut in all p_T region. Note here the average value of P/E is above 1 since E is maximum energy deposition in a single BEMC tower

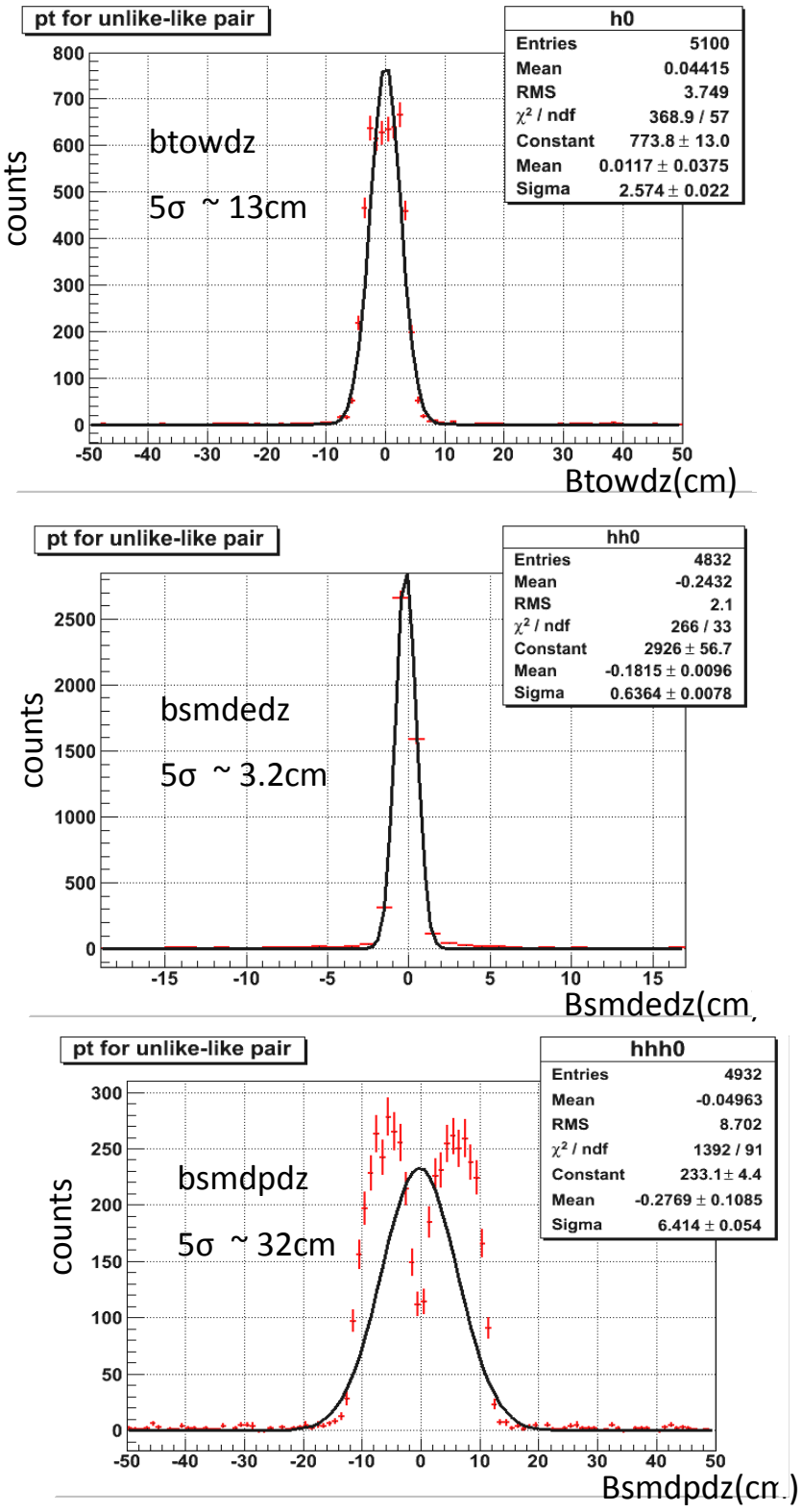

Figure 5.3 BEMC and BSMD association window at z plane.

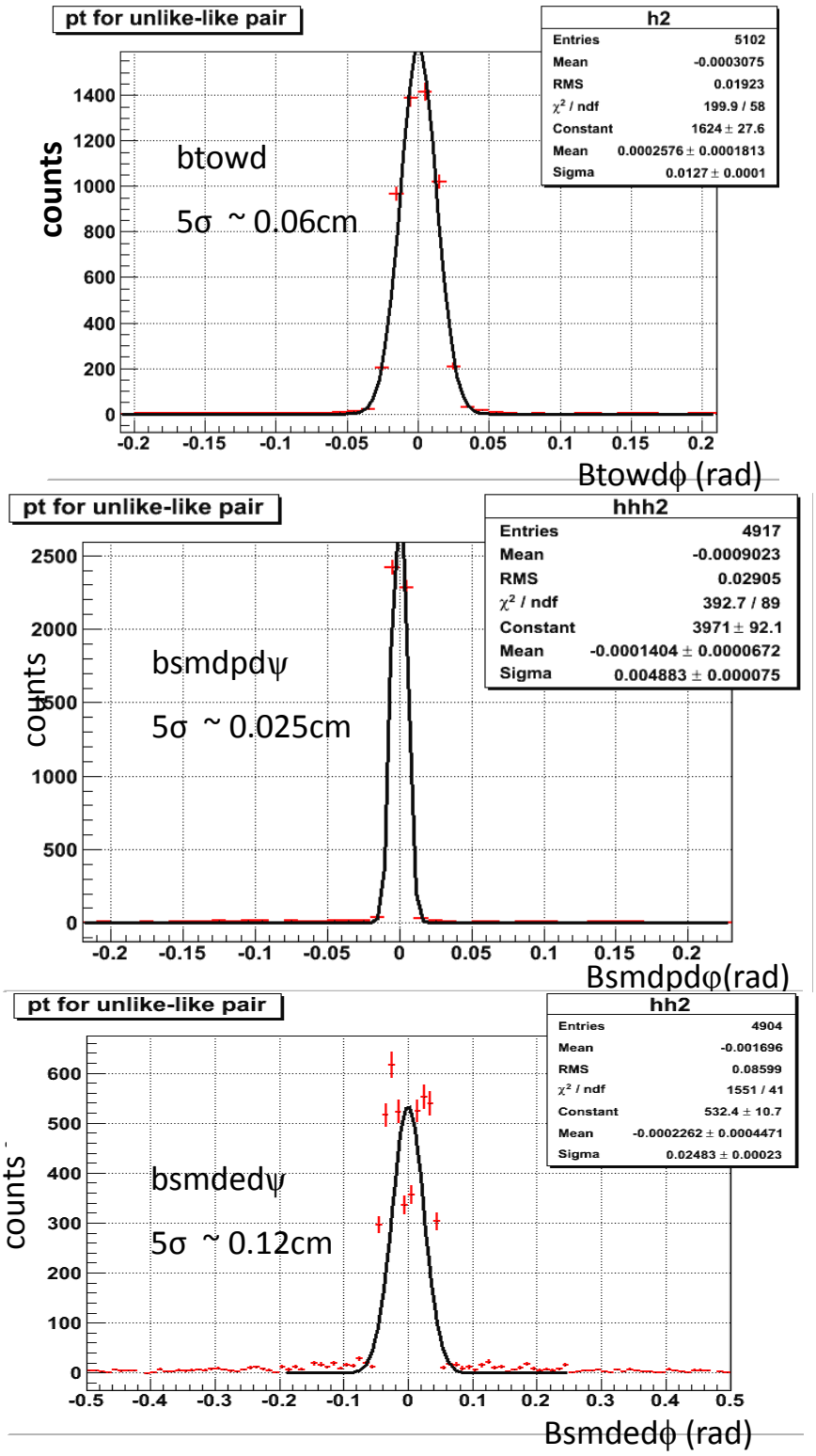

Figure 5.4 BEMC and BSMD association window at R-ϕ plane

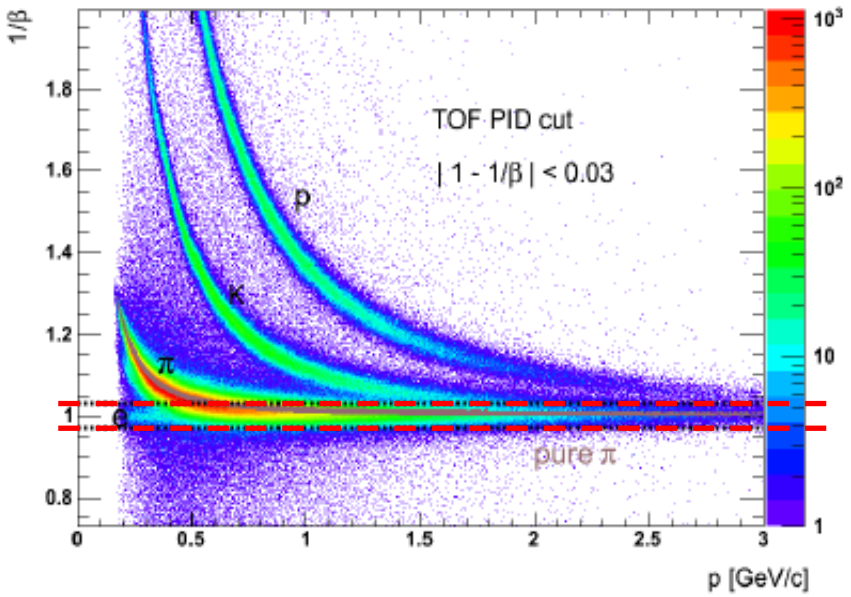

Figure 5.5 Particle velocity measured by TOF vs. transverse momentum

5.4 Purity Estimation for Inclusive Electron Candidate

In order to exclude the hadron contamination in inclusive electron candidates, we applied same method as Run2008 analysis: use the shape of $n\sigma_e$ distribution for pure electron (one gaussian distribution) and pure hadron (two gaussian distributions for pion and kaon) to set up the three-gaussian fit the $n\sigma_e$ (constraint fit) for inclusive electrons to estimate the purity of $n\sigma_e$ cut. To achieve the input parameters of three-gaussian fit, we use Bichsel function to calculate mean value and width of kaon and pion's $n\sigma_e$ distribution per p_T bin. For electron, as shown in Figure 5.6, apply direct

Gaussian fit on pure electron $n\sigma_e$ distribution per p_T bin. then get their mean value and width vs p_T as shown in Figure 5.7.

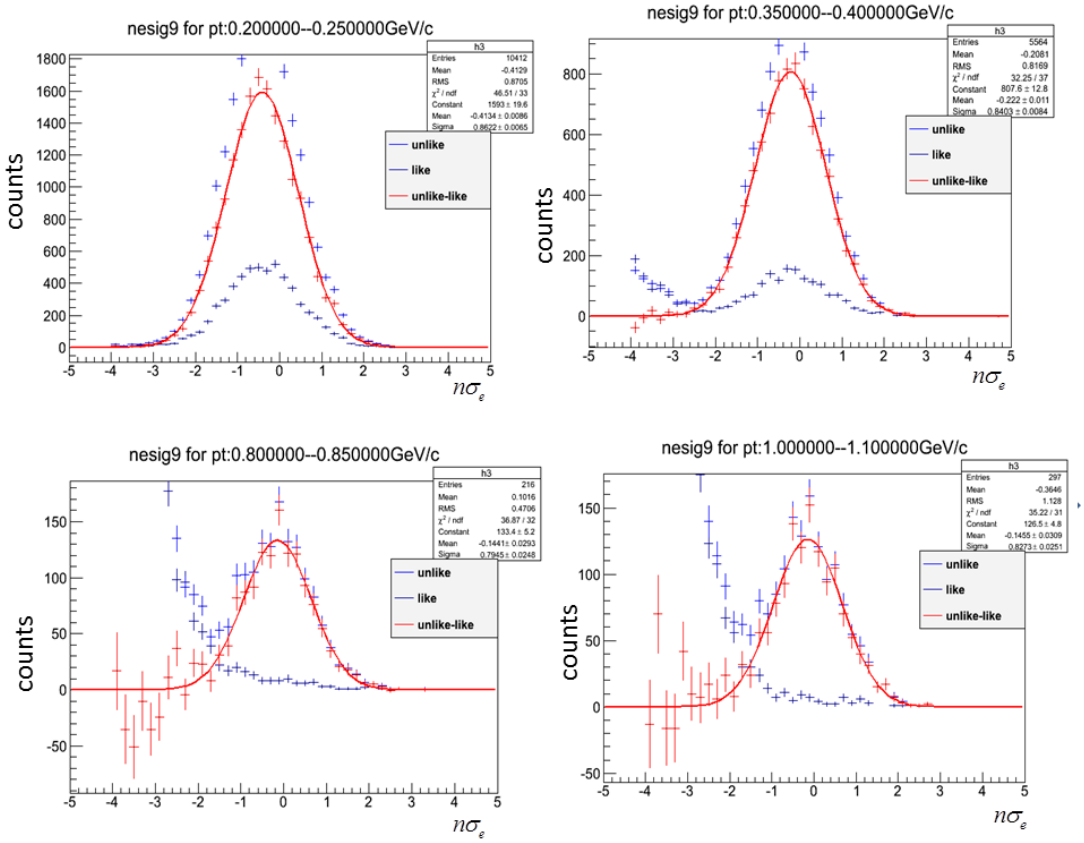

Figure 5.6 pure photonic electron $n\sigma_e$ distribution for different p_T bin

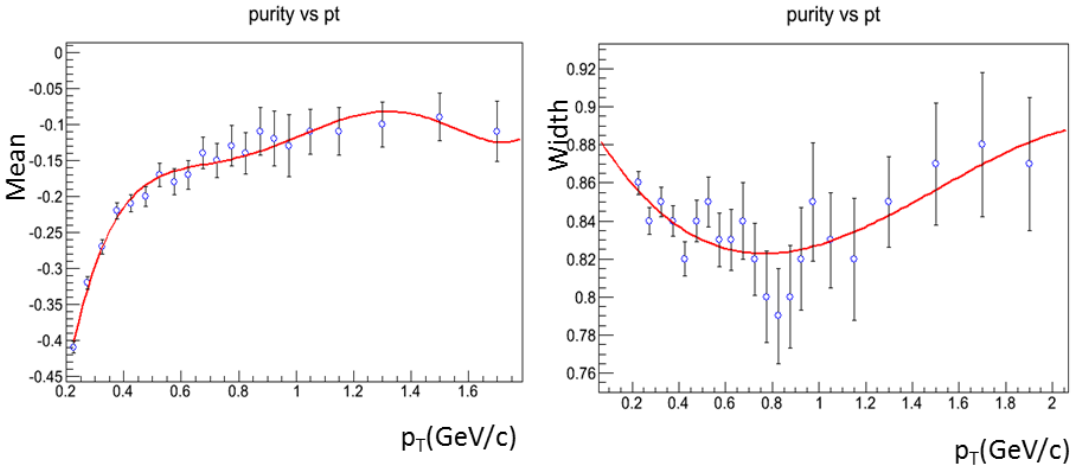

Figure 5.7 photonic electron $n\sigma_e$ distribution mean value and width vs p_T.

Figure 5.8 shows the purity fit at different p_T region. Note that at low p_T, where the kaon contribution is far from electron's and pion's, two gaussian fit is sufficient. And since we applied different electron identification cuts at p_T >2GeV/c and p_T <2GeV/c, their purity vs p_T spectrum should be separately estimated, as shown in Figure 5.9.

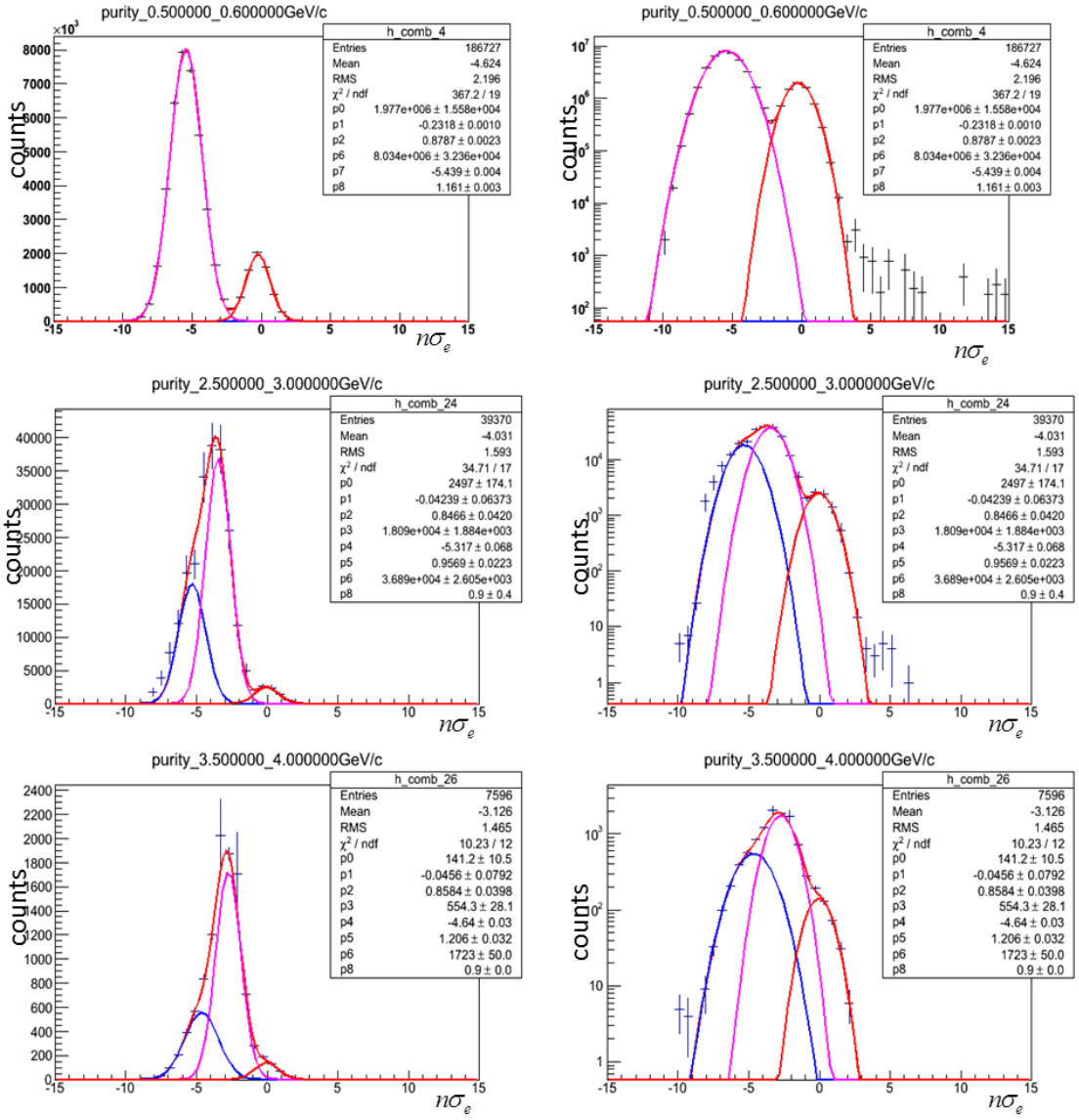

Figure 5.8 purity fit in different p_T region

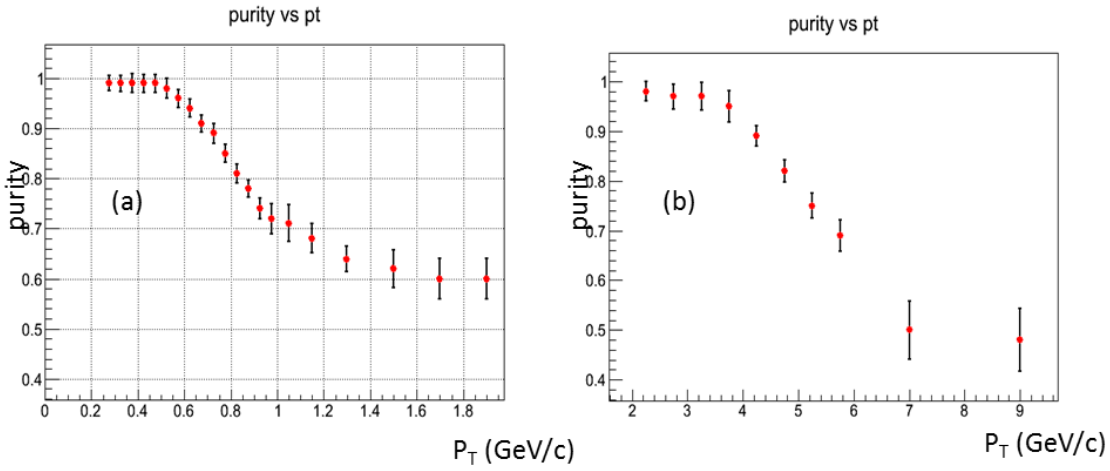

Figure 5.9 (a)purity vs p_T at p_T < 2GeV/c (b)purity vs p_T at different p_T >2GeV/c

5.5 Photonic Electron Reconstruction Efficiency

The photonic reconstruction efficiency is obtained in the same way as high p_T analysis using Run2008 data. To eliminate the low quality tracks causing the large fluctuation, we reject them by applying a cut on the on the radius of the 1st TPC track point < 70cm. Figure 5.10 shows the photonic reconstruction efficiency as a function of p_T. The effect from discrepancy of p_T nfit, nfit/nmax and pair DCA between embedding and real data has been corrected as shown in Figure 5.11

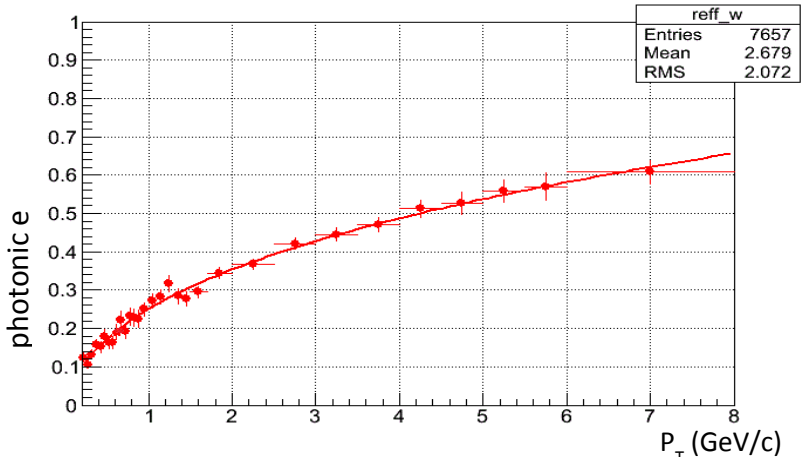

Figure 5.10 photonic reconstruction efficiency vs p_T

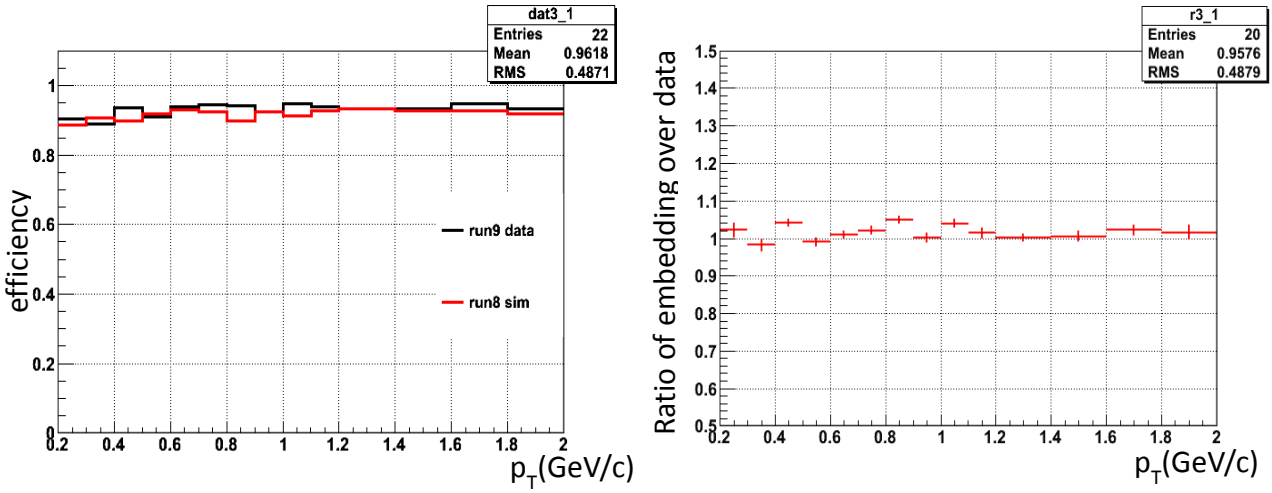

Figure 5.11 (a) efficiencyiy for cuts on partner nfit, nfit/nmax and pair DCA (b) Efficiency difference between embedding and real data

5.6 Electron Identification Efficiency Estimation from data

At p_T >2GeV/c, we calculate the electron identification efficiency at using combined p_T spectrum as we did in Run2008. Figure 5.12 shows Run2009 Electron Identification efficiency at p_T >2GeV/c, including $n\sigma$, p/e and BEMC association window. It agrees well with the same efficiency of Run2008.

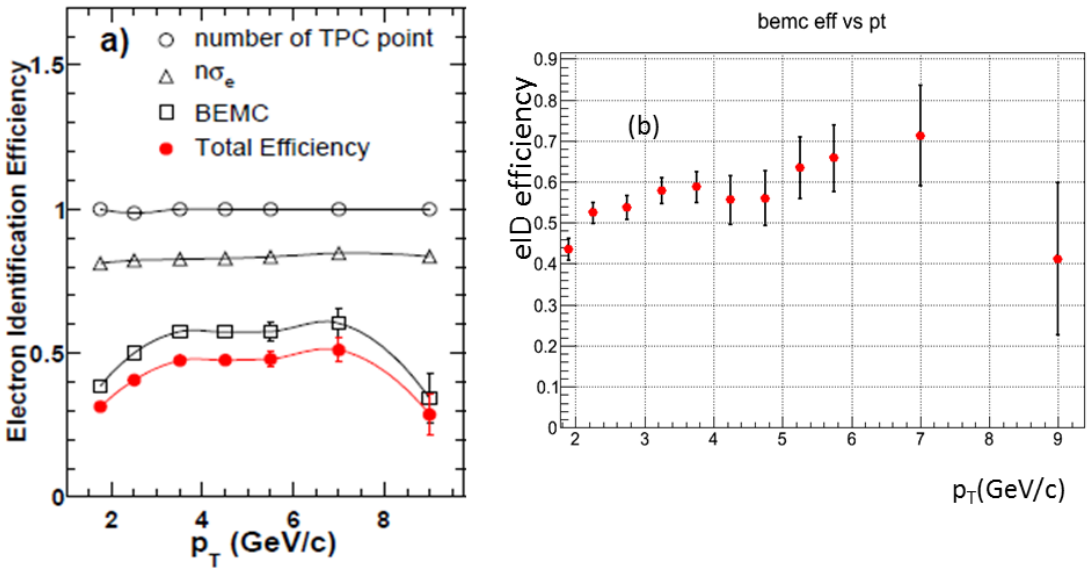

Figure 5.12 (a) BEMC efficiency for Run2008 (b) BEMC efficiency for Run2009

At p_T <2GeV/c, to calculate the TOF efficiency, we use VPD minimum-bias events from pp2pp prod

uction to exclude the pileup effect via function:

TOD cut efficiency = (counts applied $n\sigma$ >-1&|1-1/β |<0.03) / (counts only applied $n\sigma$ >-1). In order to make sure both numerator and denominator are pure electron sample, we avoid the p_T region where $n\sigma$ of electron & hadron overlapping (shown in Figure 5.13 left panel). Another cross check is applying BEMC electron identification cuts on

both numerator and denominator to calculate the TOF efficiency, sacrificing the statistics but ensuring the purity of electron sample. The right panel shows the TOF efficiency w/o BEMC cuts, these two agree with each other, and almost independent of p_T.

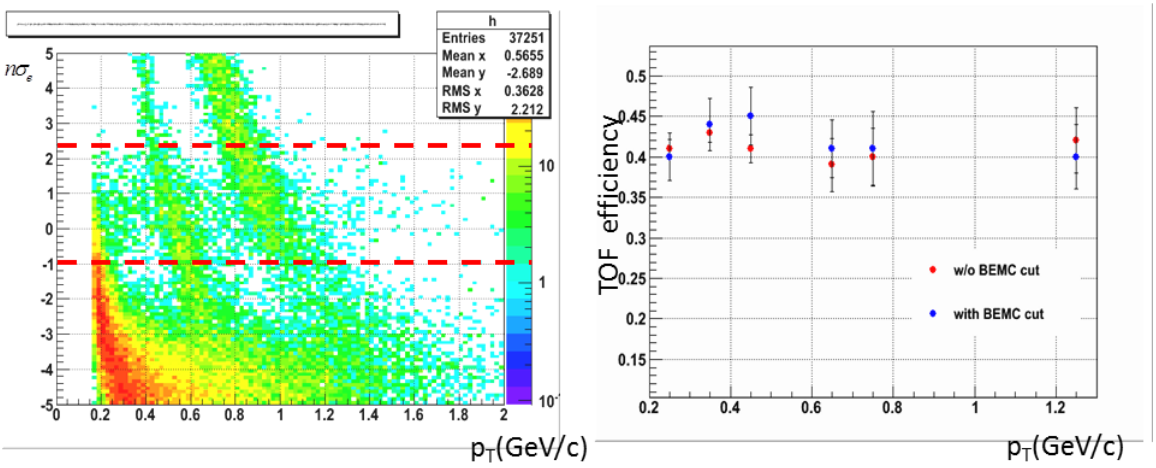

Figure 5.13 (left) $n\sigma$ vs p_T for e, π and K. (right) TOF efficiency without BEMC cuts

5.7 VPD Efficiency estimation with PYTHIA Simulations

With VPD as minimum-bias trigger in Run2009, to obtain the cross section of real non-single diffractive events, it is necessary to estimate the VPD efficiency dependent on NPE p_T for charm and bottom events. The trigger and vertex bias correction was studied by simulating the PYTHIA events, similarly processed via the full GEANT detector response and offline reconstruction. We start with the PYTHIA generator v6.410,

generate 200K events generated for both charm and bottom events to separately estimate the VPD efficiency. If one event can fire both east and west VPD, it is regarded as a VPD event.

Figure 5.14 shows the general simulation process. VPD efficiency for B meson is different from D meson as shown in Figure 5.15. But since the amount of B meson is much smaller than D meson at p_T <2GeV, only use D meson VPD efficiency to estimate the correction factor.

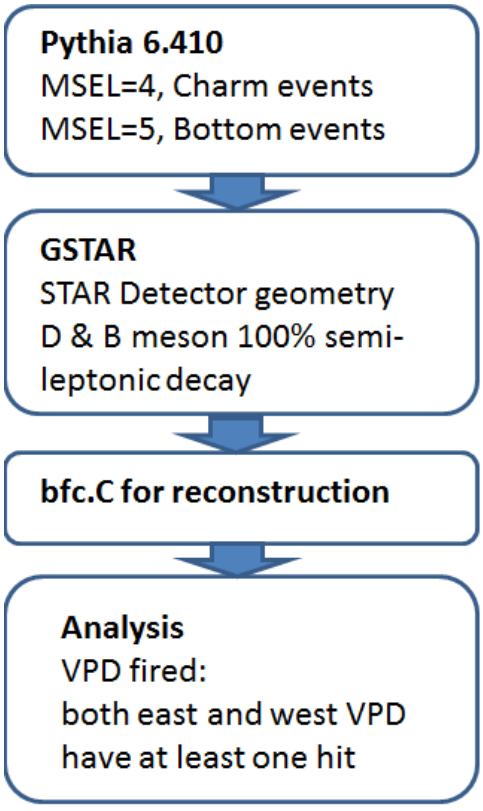

Figure 5.14 general simulation process to estimate the VPD efficiency

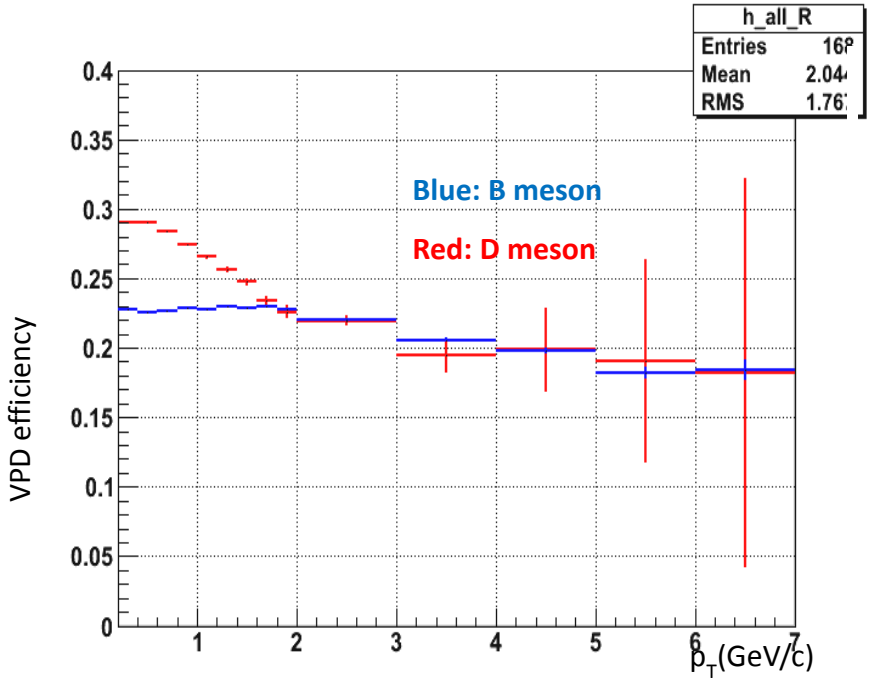

Figure 5.15 VPD efficiency vs p_T for B meson and D meson

5.8 Ratio of Non-photonc over Photonic Electron Yields and Invariant Cross Section Calculation

The following equation is used to calculate the invariant cross section:

$$E\frac{d^3\sigma}{dp^3} = \sigma_{NSD}\frac{1}{2\pi p_T}\frac{N_e(|zvtx| < 30cm)}{N_{evt}(|Zvtx| < 30cm)}\frac{1}{\varepsilon_{acc}\varepsilon_{eID}\varepsilon_{VPD}}$$

where NSD cross section is σ_{NSD} = 30$\pm$2.4 mb, ε_{eID} is eID efficiency, including: ε (BEMC), ε(TOF), ε(nsigmaE)~0.83, ε(track quality) ~0.99. ε_{accp} = 0.86, which is TPC acceptance independent of p_T . ε_{VPD} , the VPD efficiency mentioned in Chapter 4.7. N_e(|zvtx|<30cm):

yield of non-photonic at |zvtx|<30cm. N_{evt}(|zvtx|<30cm): yield of minimum-bias events at |zvtx|<30cm, ~ 188M (evts) x 268(avg_ps).

Figure 5.16 shows Run2009 non-photonic invariant cross section for all p_T. It agrees with Run2008 result at p_T >2GeV/c. The systematic error analysis is ongoing and not shown on the plot. The comparison with FONLL shows pQCD can describe heavy quark production for all p_T at RHIC.

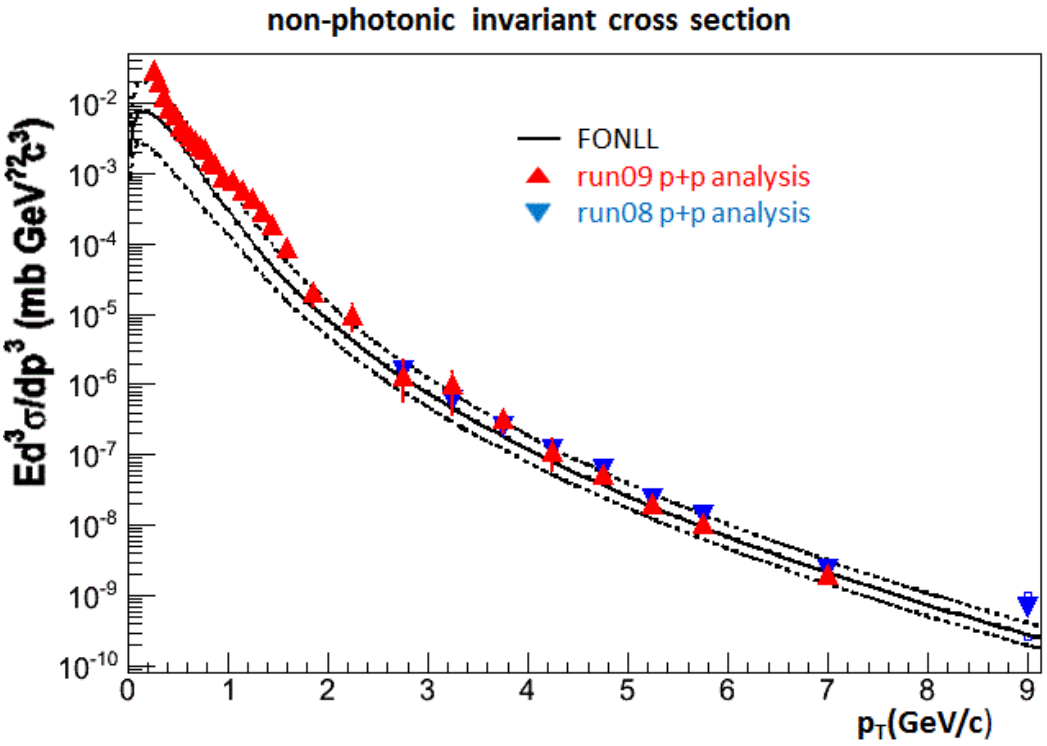

Figure 5.16 Non-photonic invariant cross section. red data points represent the result of this analysis, blue represent the published result from Run2008. FONLL prediction and its uncertainties are represented by lines.

6. SUMMARIES AND PERSPECTIVE

This thesis work resolved the long standing puzzle of the RHIC non-photonic electron production in the Quark-Gluon plasma produced at RHIC in Au+Au collisions and firmly established the experimental evidence that heavy quark production in the hot and dense medium is suppressed. In the meantime, this work proves that heavy quark production can be described by pQCD at RHIC energy in *p+p* collisions.

However, more differential measurements, especially the separate measurements of charm and bottom quark productions, are needed to further understand the energy loss mechanism of particles traversing the hot and dense medium. STAR is expected to install the Heavy Flavor Tracker (HFT) in Run2014. HFT can precisely measure the secondary vertices of decay particles and allow separating charm and bottom quark contribution to experimental observables.

BIBLIOGRAPHY

[1] http://www.bnl.gov/rhic/.

[2] http://www.bnl.gov/discover/winter_06/perfect_1.asp.

[3] S. S. Adler et al. (PHENIX Collaboration), Phys. Rev. Lett. 96, 032301 (2006); B.I. Abelev et al. (STAR Collaboration), Phys. Rev. Lett. 98, 192301 (2007).

[4] M. Cacciari, P. Nason and R. Vogt, Phys. Rev. Lett. 95, 122001 (2005); R. Vogt, private communication.

[5] M. Asakawa et al., Phys. Rev. Lett. 92 012001 (2004); Datta S et al., Phys. Rev. D 69 094507 (2004).

[6] T. Matsui, and H. Satz, Phys. Lett. B 178, 416 (1986).

[7] J. Bouchet for the STAR Collaboration, Nucl. Phys. A830, 636c-637c (2009); J. Kapitan for the STAR Collaboration, Eur. Phys. J. C 62, 217-221 (2009).

[8] K. Adcox et al. (PHENIX Collaboration), Phys. Rev. Lett. 88, 022301 (2001).

[9] D. Kharzeev et al., Phys. Lett. B 561, 93 (2003).

[10] M. Djordjevic et al., Phys. Lett. B 632, 81 (2006).

[11] H. Agakishiev et al. (STAR Collaboration), Phys. Rev. D 83, 052006 (2011).

[12] B. I. Abelev et al. (STAR Collaboration), Phys. Rev. Lett. 106, 159902(E) (2011).

[13] M. Anderson, et al., Nucl. Instr. and Meth. A 499, 655 (2003).

[14] M. Beddo et al., Nucl. Instrum. Meth. A 499, 725 (2003).

[15] http://www.star.bnl.gov/public/tof/.

[16] J. Kiryluk (STAR Collaboration), 16th International Spin Physics Symposium Proc., 718 (2005).

[17] W.J. Llope et al., Nucl. Instr. Meth. A522, 252 (2004).

[18] N. Armesto et al., Phys.Lett. B 637 362 (2006).

[19] H. van Hees, V. Greco and R. Rapp, Phys. Rev. C 73, 034913 (2006) and private communication.

[20] R. Sharma et al., Phys. Rev. C 80, 054902 (2009).

[21] Review of Particle Physic, Phys. Letts B 667, 1-5 (2008).

[22] L. Lyons et al., Nucl. Instr. Meth A 270, 110 (1988); A. Valassi, Nucl. Instr. Meth A500, 391(2003); L. Demortier et al., FERMILAB-TM-2084.

Appendix A: Combining Run2008 and Run2005 Measurements

A1. Method for Combining Two Measurements

There are at least two methods combining multiple measurements of the same quantities. The so called "PDG" method is the standard weighing method that is described in the section of "average and fits" in every PDG publication [21]. The other one is the "Best Linear Unbiased Estimate" (BLUE) method [22]. The "BLUE" method is more general and is able to breakdown statistical error from systematic errors and different component of systematic errors as well.

A1.1 **"PDG " way of Combining two Measurements**

A1.1.1 Two measurements are independent

Two measurements are $x_1 \pm \sigma_1$ and $x_2 \pm \sigma_2$, where σ_1 and σ_2 are total errors, i.e.

$$\sigma_i = \sqrt{(\sigma_i^{stat})^2 + \left(\sigma_i^{syst}\right)^2}$$

Assuming there is no correlation between σ_1 and σ_2, the combined result is $\langle x \rangle \pm \sigma$

$$\langle x \rangle = \frac{x_1/\sigma_1^2 + x_1/\sigma_2^2}{1/\sigma_1^2 + 1/\sigma_2^2} \quad \text{..... (1)}$$

$$\sigma = \frac{1}{\sqrt{1/\sigma_1^2 + 1/\sigma_2^2}} \quad \text{.....(2)}$$

A1.1.2 **Two measurements have common systematic uncertainties**

Assuming two measurements have a common systematic error Δ, one can rewrite the systematic error for each measurements as

$$\sigma_i = \sqrt{(\sigma_i^{uc})^2 + (\sigma_i^{uc} \cdot \Delta)^2 \sum_{j=1}^{2} \frac{1}{\left(\sigma_j^{uc}\right)^2}} \text{ ..... (3)}$$

, where σ_i^{uc} include the statistical error and uncorrelated systematic error. One can then use eq.(1) and (2) to calculate the combined measurements and combined total uncertainties, and the equation are

$$\langle x \rangle = \frac{x_1(\sigma_2^{uc})^2 + x_2(\sigma_1^{uc})^2}{(\sigma_2^{uc})^2 + (\sigma_1^{uc})^2} \text{.....(4)}$$

$$\sigma = \sqrt{\frac{\sigma_1^2\sigma_2^2 - \Delta^4}{\sigma_1^2 + \sigma_2^2 - 2\Delta^2}} \text{.....(5).}$$

Details of derivation of eq.(4) and (5) can be found on Appendix A.

A1.2 **"BLUE" way of Combining two Measurements**

The following are mostly from ref. [22]. The weights ω_1 and ω_2 for calculating combined result, i.e. $\langle x\rangle = \omega_1 x_1 + \omega_2 x_2$, are obtained my minimizing the χ^2 with respect to $\langle x\rangle$, namely $\chi^2 = Q^t E^{-1} Q$, where

$$Q = \begin{pmatrix} \langle x\rangle - x_1 \\ \langle x\rangle - x_2 \end{pmatrix}$$

, and E is the covariance matrix

$$E = \begin{pmatrix} \sigma_1^2 & \rho\sigma_1\sigma_2 \\ \rho\sigma_1\sigma_2 & \sigma_2^2 \end{pmatrix}$$

$$E^{-1} = \frac{1}{\sigma_1^2\sigma_2^2(1-p^2)} \begin{pmatrix} \sigma_2^2 & -\rho\sigma_1\sigma_2 \\ -\rho\sigma_1\sigma_2 & \sigma_1^2 \end{pmatrix}$$

Therefore,

$$\chi^2 = \frac{\Delta x_1^2\sigma_2^2 + \Delta x_2^2\sigma_1^2 - 2\rho\sigma_1\sigma_2\Delta x_1\Delta x_2}{\sigma_1^2\sigma_2^2(1-\rho^2)} \text{.....(6)}$$

, where $\Delta x_1 = \langle x\rangle - x_1$ and $\Delta x_2 = \langle x\rangle - x_2$

Minimizing χ2 with respect to $\langle x\rangle$, one obtain

$$\omega_1 = \frac{\sigma_2(\sigma_2 - \rho\sigma_1)}{\sigma_1^2 + \sigma_2^2 - 2\rho\sigma_1\sigma_2} \text{.....(7)}$$

$$\omega_2 = \frac{\sigma_1(\sigma_1 - \rho\sigma_2)}{\sigma_1^2 + \sigma_2^2 - 2\rho\sigma_1\sigma_2} \text{.....(8)}$$

The combined result is

$$\langle x \rangle = \frac{\sigma_2(\sigma_2-\rho\sigma_1)x_1+\sigma_1(\sigma_1-\rho\sigma_2)x_2}{\sigma_1^2+\sigma_2^2-2\rho\sigma_1\sigma_2} \text{.....(9)}$$

The total uncertainty is

$$\sigma = \sqrt{\frac{\sigma_1^2\sigma_2^2(1-\rho^2)}{\sigma_1^2+\sigma_2^2-2\rho\sigma_1\sigma_2}} \text{.....(10)}$$

The combined statistical error is

$$\sigma^{stat} = \sqrt{\omega_1^2(\sigma_1^{stat})^2 + \omega_2^2(\sigma_2^{stat})^2}$$

$$= \frac{\sqrt{(\sigma_2(\sigma_2-\rho\sigma_1))^2\left(\sigma_1^{stat}\right)^2+(\sigma_1(\sigma_1-\rho\sigma_2))^2\left(\sigma_2^{stat}\right)^2}}{\sigma_1^2+\sigma_2^2-2\rho\sigma_1\sigma_2} \text{.....(11)}$$

, where σ_i^{stat} is the statistical error of each measurements.

The combined total systematic error is

$$\sigma^{syst} = \sqrt{\sigma^2 - (\sigma^{stat})^2} \text{.....(12)}$$

A1.3 **How to calculate correlation coefficient (ρ)**

The equation to calculate the correlation coefficient is

$$\rho = \frac{\sum_{i=1}^{N} \rho_i \sigma_{1,i}^{syst} \sigma_{2,i}^{syst}}{\sigma_1 \sigma_2} \text{.....(13)}$$

, where $\sigma_{1,i}^{syst}$ and $\sigma_{2,i}^{syst}$ are the breakdown of systematic error for the first and second measurement, respectively. ρ_i is the correlation coefficient for the ith systematic error between the two measurements. To accurately calculate the ρ_i one need to know the P.D.F. of each systematic error. Since this is practically hard to do, we assign either $\rho_i = 0 \; or \; \rho_i$ =1 which means.

- ρ=0 when two measurements are independent,
- ρ=1 when two measurement are fully correlated
- ρ= -1 when two measurements are fully anticorrelated.

See chapter A2 for detailed assignment for different category of systematic errors.

A1.4 **Breakdown the combined systematic errors**

The advantage of "BLUE" method is that it allows the breakdown of different types of systematic errors, e.g. point to point and scaling errors. For the ith systematic error

$$\sigma_i^{syst} = \sqrt{(\omega_1 \;\; \omega_2) \begin{pmatrix} \left(\sigma_{1,i}^{syst}\right)^2 & \rho_i \sigma_{1,i}^{syst} \sigma_{2,i}^{syst} \\ \rho_i \sigma_{1,i}^{syst} \sigma_{2,i}^{syst} & \left(\sigma_{2,i}^{syst}\right)^2 \end{pmatrix} \begin{pmatrix} \omega_1 \\ \omega_2 \end{pmatrix}}$$

$$= \sqrt{\left(\omega_1 \sigma_{1,i}^{syst}\right)^2 + \left(\omega_2 \sigma_{2,i}^{syst}\right)^2 + 2\omega_1 \omega_2 \rho_i \sigma_{1,i}^{syst} \sigma_{2,i}^{syst}}, \ldots\ldots\ldots\ldots\ldots\ldots\ldots (14)$$

where σ_i^{syst} is the *i*th systematic error, $\sigma_{1,i}^{syst}$ is the *i*th systematic error of the first measurements and $\sigma_{2,i}^{syst}$ is the *i*th systematic error of the second measurement.

A1.5 **χ2 test to quantify the consistency between two measurement**

The χ^2 obtained from eq.(6) are for two measurements of the same observable. To compare if two p_T spectra are consistent with each other, one can treat different p_T bin as different observable. Assuming there is no correlation among different p_T bins, the total χ^2 can be calculated as the following

$$\chi^2 = \sum_{i=1}^{N} \chi_i^2 \ldots\ldots\ldots\ldots\ldots\ldots\ldots\ldots\ldots (15)$$

, where N is the number of p_T bins, χ_i^2 is the number for each p_T bin as calculated from eq. (6). If all individual error are Gaussian, the value calculate from eq. (15) should follow χ^2 distribution of N degree of freedom.

A1.6 **Relation between "PDG" and "BLUE" method**

When two measurements are totally independent, ρ=0, then eq.(7) and (8) become eq.(1), (2). In the case that two measurement are correlated, if we take $\Delta^2 = \rho\sigma_1\sigma_2$, then equation (7) and (8) become eq.(4) and (5).

A2. List of Systematic Errors for Run5 and Run8

1. Bin-by-bin errors
   A. Uncorrelated error. The details for run5 and run8 are listed below. The total uncorrelated error is the square root of the sum of each individual uncertainty square. The correlation coefficient for this total uncertainty between run05 and run08 is assigned as $\rho = 0$.
      a. In run8, it includes the following errors
         - Momentum smearing correction.
            - Same as in run05 but Run5 convolute this in the eID efficiency estimation.
         - Purity estimation
            - Run5 has a lot more photonic electrons.
         - trigger efficiency
            - Different method from run5
         - eID efficiency estimation
            - run8 from data and run5 from embedding
         - Photonic reconstruction efficiency
            - Different effect from pi0 dalitz.

      b. In run5, it includes the following errors
         - Trigger efficiency
            - Different method from run08
         - Combining HT1 and HT2 trigger
            - Different from run08.
         - Purity estimation
            - Much higher photonic electron.
         - eID efficiency estimation
            - run05 from embedding. Run08 from data.
         - photonic e reconstruction eff
            - Different pi0 dalitz effect from run08

   B. Correlated errors between run5 and run8 are listed below. The total uncorrelated error is the square root of the sum of each individual uncertainty square. The correlation coefficient for this total uncertainty between run05 and run08 is assigned as $\rho = 1$, i.e. we assume they are fully correlated between run05 and run08.

      a. In run8, it includes the following errors
         - p_T dependence of single electron acceptance.

- Bin shift correction
- Different trigger efficiency between NPE and PHE
- contribution from vector mesons.

b. In run5, it include the following errors
   - Bin shift correction
   - p_T dependence of single electron acceptance
   - contribution from vector mesons

2. Scaling errors
   A. Uncorrelated errors. The total uncorrelated error is the square root of the sum of each individual uncertainty square. The correlation coefficient for this total uncertainty between run05 and run08 is assigned as $\rho = 0$.

- In run08, it includes
  - Cut on TPC 1st point: 2.3%.
    - Not exist in run05
  - HT2 cross section w.r.t. BBC: 2.3%
    - Not exist in run05
  - Run-by-run variance for trigger + tracking + acceptance: 15%
    - Different run conditions
  - Error from combining all the triggers: 5%
    - Different method from run05.

- In run5, it includes the following errors
  - Run-by-run variation.
    - Different run condition from run08

   B. Correlated. The total uncorrelated error is the square root of the sum of each individual uncertainty square. The correlation coefficient for this total uncertainty between run05 and run08 is assigned as $\rho = 1$, i.e. we assume they are fully correlated between run05 and run08.

a. In run08, it includes
   - the ratio of embedding and data on acceptance :

b. In run05, it includes
   - the ratio of embedding and data on acceptance

3. Normalization error. This should belong to the correlated scaling error. I leave it alone since it's the same for all p_T bins while the combined correlated scaling error is only up to p_T =6GeV/c.
   - BBC cross section and efficiency uncertainty: 14%/sqrt(2).

A3. Derivation of eq.(4) and (5).

From eq.(1) and (3), one obtain

$$\langle x \rangle = \frac{[(\sigma_1^{uc})^2 x_2 + (\sigma_2^{uc})^2 x_1] \cdot \left[1 + \Delta^2 \left(\frac{1}{\sigma_1^2} + \frac{1}{\sigma_2^2}\right)\right]}{[(\sigma_1^{uc})^2 + (\sigma_2^{uc})^2] \cdot \left[1 + \Delta^2 \left(\frac{1}{\sigma_1^2} + \frac{1}{\sigma_2^2}\right)\right]}$$

This is eq.(4).

From eq.(2) and (3), one obtain

$$\sigma = \frac{\sigma_1^{uc}\sigma_2^{uc}\left[1 + \Delta^2 \left(\frac{1}{(\sigma_1^{uc})^2} + \frac{1}{(\sigma_2^{uc})^2}\right)\right]}{\sqrt{[(\sigma_1^{uc})^2 + (\sigma_2^{uc})^2] \cdot \left[1 + \Delta^2 \left(\frac{1}{\sigma_1^2} + \frac{1}{\sigma_2^2}\right)\right]}}$$

$$= \sqrt{\frac{(\sigma_1^{uc})^2(\sigma_2^{uc})^2 + (\sigma_2^{uc})^2\Delta + (\sigma_1^{uc})^2\Delta}{(\sigma_1^{uc})^2 + (\sigma_2^{uc})^2}}$$

$$= \sqrt{\frac{((\sigma_1^{uc})^2 + \Delta^2)((\sigma_2^{uc})^2 + \Delta^2) - \Delta^4}{(\sigma_1^{uc})^2 + \Delta^2 + (\sigma_2^{uc})^2 + \Delta^2 - 2\Delta^2}}$$

$$= \sqrt{\frac{\sigma_1^2\sigma_2^2 - \Delta^4}{\sigma_1^2 + \sigma_2^2 - 2\Delta^2}}$$

This is eq.(5).

Appendix B: Answers to the Questions from the Advisory Committee

B1. How the Ncoll and centrality is determined?

In STAR we use the Glauber model to estimate the number of nucleon-nucleon collisions (Ncoll). The Glauber Model views the collision of two nuclei in terms of the individual interactions of the constituent nucleons. The model assumes that these nucleons will be essentially not deflected as the nuclei pass through each other at sufficiently high energies. This makes it possible to develop simple analytic expressions for the nucleus-nucleus interaction cross section and for the number of interacting nucleons and the number of nucleon-nucleon collisions in terms of the basic nucleon-nucleon cross section and correlate the impact parameter, number of participating nucleons, Ncoll and charged multiplicity. The centrality is determined by comparing the measured charged multiplicity for $|\eta| < 0.5$ to the simulation results in each centrality bin where the corresponding Ncoll can be calculated. A centrality bin corresponds to the degree of overlaps between two collider nuclei. In STAR, we slice the charged particle multiplicity as shown in the following figures to define different centrality bins.

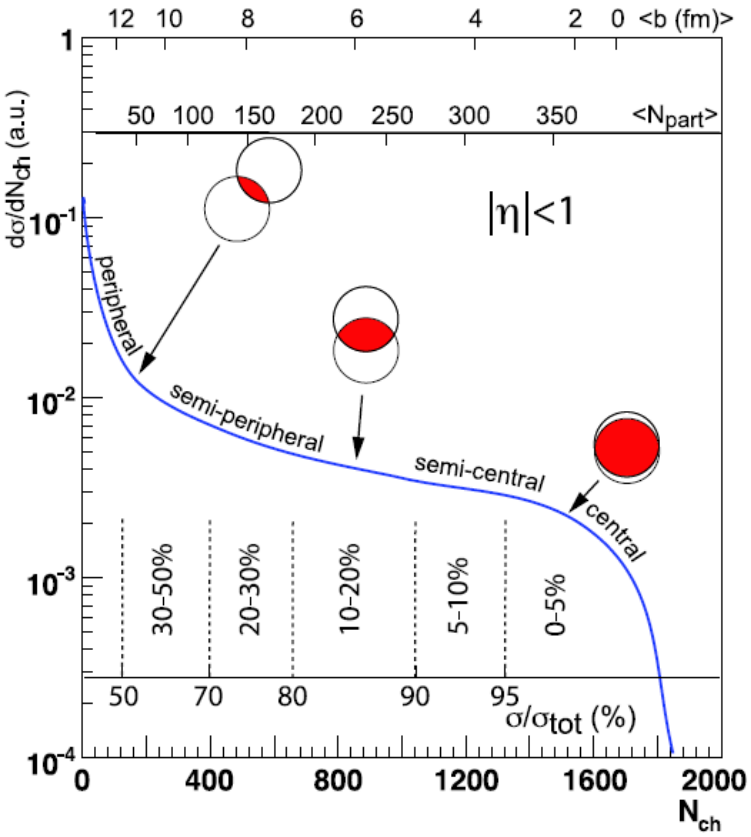

B2. What is the evidence of thermalization?

There are two major evidences of thermalization: a) observed large elliptic flow can be described by hydrodynamic models. b) measurement of particle ratios can be described by thermal statistical model.

Hydrodynamic models require the system to be thermalized. In the past, there has always been large discrepancies between the hydrodynamic model prediction and

experimental data in various low energy heavy-ion experiments. This situation persists until the results from RHIC came out. The model and RHIC data agree with each other very well. In addition, strong radial flow also provides the related evidence for thermalization. The thermal statistical models need inputs on the system temperature (T), the baryon-chemical potential μB, the strangeness chemical potential μS. Once these parameters are fixed, thermal model can predict the yield of different particle species. In reality, we fit the model to the experimental results on particle ratios. It turns out the model predictions can describe the experimental results very well most of the particle species using a single sets of temperature and chemical potential as shown in the following figure.

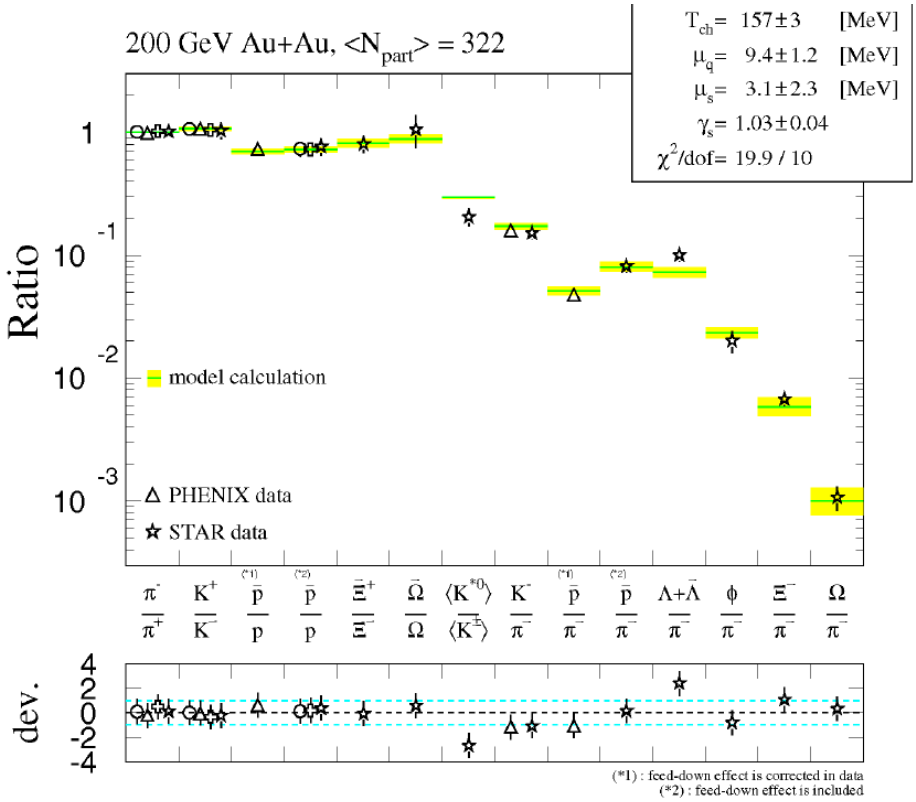

B3. How radiation length is defined and how the probability of $7/9*X_0$ is derived.

The high-energy electrons predominantly lose energy in medium through bremsstrahlung radiation and electron-positron pair production. The characteristic amount of matter traversed for these related interactions is called the radiation length X_0. It is both the mean distance over which a high-energy electron loses all but 1/e of its energy by bremsstrahlung, and 7/9 of the mean free path for pair production by a high-energy photon. It is also the appropriate scale length for describing high-energy electromagnetic cascades. X_0 has been calculated and tabulated by Y.S. Tsai [Rev. Mod. Phys. 46, 815 (1974)]. We removed SVT in Run2008 at STAR experiment leading to a significant reduction of material. The probability for electron bremsstrahlung should be $P = 1 - e^{\{-x/X_0\}}$. The probability for photon conversion is $P = 1 - e^{\{-x/(9/7*X_0)}$. Since x is small compared to X_0, the latter one can be written as $P \approx 1 - (1-7/9*x/X_0) = 7/9*x/X_0$. Note that as I mentioned during my presentation, X_0 is the percentage of radiation length, which is x/X_0 here.

B4. Provide one possible reason why R_{AA} can be larger than 1.0?

R_{AA} is defined as $R_{AA} = \frac{Yield\ (Au+Au)}{Ncoll \cdot yield(p+p)}$, where yield(Au+Au) and yield (*p+p*) is the yield in Au+Au and *p+p* collisions, respectively; Ncoll is the number of nucleon -nucleon collisions in a single Au+Au collisions.

We can find four possible reasons: a) radial flow push particles from low-p_T to intermediate p_T, resulting in $R_{AA} > 1$ at intermediate p_T; b) coalescence/recombination enhanced particle yield at intermediate p_T range, resulting in $R_{AA} > 1$ at intermediate p_T. c) The initial multiple scattering (so-called Cronin effect); d) jet quenching. Jet quenching at high p_T will enhance particle yield from low to intermediate p_T. Since jet yield is quite small, this effect is neglected. Cronin effect broadens the p_T spectrum via multiple scattering which leads to $R_{AA} > 1$.

B5. Explain more clearly why a small mistake in photonic reconstruction efficiency can leads to large error on NPE yield?

Because there is a dominant photonic electron background, NPE/PHE ratio is very low before SVT removal. NPE = inclusive E – PHE/ε. A small difference in photonic reconstruction efficiency, i.e. ε, will lead to a huge difference in PHE background subtraction. For example, the NPE/PHE ~0.2 – 0.4 depend on pT. Assuming ε~0.5, if ε is overestimated by 10% in absolute value which corresponds to 20% relative error, the according to above equation the relative change in NPE yield is

$$\frac{\Delta NPE}{NPE} = \frac{1}{NPE/PHE}\left(1 - \frac{1}{1.2}\right)$$ ~ 40% - 90%, i.e. a large change.

B6. Why don't we see muon in the 1/β vs. p and dE/dx vs. p plot

The muon mass and pion mass are close to each other. Mass (muon) = 105.7 MeV and mass (pion) = 139.6 MeV. Therefore in the 1/beta vs. p plot, the muon and pion band are very close to each other. The muon band can be identified right blow the pion band by a careful look at the left panel of the following figures within the circled area. The electron mass is only 0.51 MeV. Therefore the electron speed is essentially the same as speed of light. In the dE/dx vs. p plot, after p > 0.1GeV, muon and charged hadron band are merged together. So the band below electron band on the right hand of the figure is a mixture of charged particles and muon but dominated by charged pions.

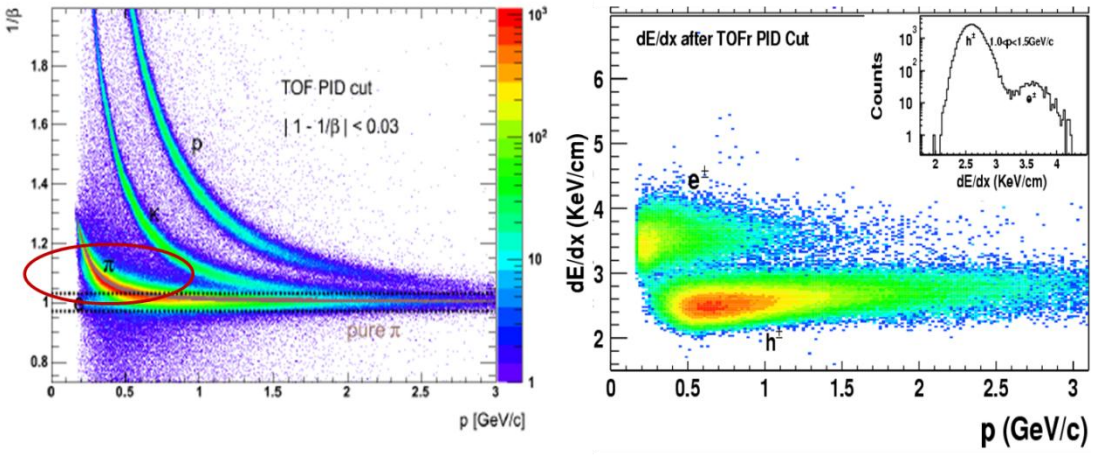

B7. Please Provide the List of Acronym

BBC Beam-Beam Counter

BEMC Barrel Electromagnetic Calorimeter

BLUE Best Linear Unbiased Estimate

BNL Brookhaven National Lab

BSMD Barrel Shower Maximum Detector

BTOW Barrel Tower

DAQ Data Acquisition

DCA Distance of the Closest Approach

EMCal Electromagnet Calorimeter

FONLL Fixed-Order Next-to-Leading Logarithm

SVT Silicon Vertex Tracker

HFT Heavy Flavor Tracker

HT High-tower Trigger

MRPC Multi-gap Resistive Plate Chamber

NPE Non-Photonic Electron

NSD Non-single Diffraction

PHE Photonic electron

PQCD Perturbative QCD

QCD Quantum Chromo-dynamics

QGP Quark Gluon Plasma

RHIC Relativistic Heavy Ion Collider

STAR Solenoid Tracker at RHIC

TOF Time of Flight detector

TPC Time Projection Chamber

VPD Vertex Position Detector

VITA

NAME: Xin Li

SEX: Male

ADDRESS: Department of Physics, Purdue University, 525 Northwestern Ave., West Lafayette, IN 47907

TELEPHONE: (765)494-4600

E-MAIL: li124@purdue.edu

EDUCATION:

09/2000-06/2004 University of Science & Technology of China(USTC), Department of Modern Physics, Bachelor of Science (Major in Applied Physics)

08/2004-06/2006 University of Science & Technology of China (USTC), Department of Modern Physics, Master of Science (06/2006, Major in Physics)

08/2006-Present Purdue University, Department of Physics, study for PhD,

Computer simulation on STAR HFT PIXEL detector

High pt non-photonic electron analysis in RICH-STAR

EXPERIENCE:

02/2005-07/2005 Department of Modern Physics, USTC

Teaching Assistant in Mechanics and Thermodynamics

Gathered and graded students' exercises and test papers

09/2005-06/2006 Department of Modern Physics, USTC

Research Assistant for Professor Hongfang Chen

Participated in seminars and academic conferences

Participated in experiments in lab.

Helped undergraduate complete thesis for bachelor's degree

08/2006-05/2008 Department 0f Physics, Purdue University,

Teaching Assistant in Quantum Mechanics

Graded students' homework and worked in help center

08/2008-present Department 0f Physics, Purdue University,

Research Assistant for Professor Wei Xie:

Computer simulation on STAR HFT PIXEL detector

High pt non-photonic electron analysis in RICH-STAR Run2008 & Run2009

ACADEMIC RESEARCH WORK:

02/2000-present Department of Modern Physics, USTC

Monte Carlo Simulation of BESIII End-Cap TOF

Beam Test of the Time Resolution of the BESIII End-cap TOF

Test of Performance of PMT and Scintillator

Data analysis of multi-gap resistive plate chamber (MRPC) for STAR-TOF at BNL

Manufacture and test of MRPC

SPECIAL SKILLS:

Computer:

C++, LINUX, AUTOCAD, and professional software such as

ROOT, GEANT4, Magboltz, Garfield

LANGUAGES:

Native Language: Chinese Foreign Language: English

PUBLICATIONS

1. H. Agakishiev et al. (STAR Collaboration), Phys. Rev. D 83, 052006 (2011).
2. B. I. Abelev et al. (STAR Collaboration), Phys. Rev. Lett. 106, 159902(E) (2011).
3. LI Xin, WU Chong, AN Shaohui et.al., Monte Carlo Simulation of BESIII End-Cap TOF ,High Energy Physics and Nuclear Physics, Vol.29,No.6 (2005)
4. LI Xin , TANG Zebo, CHENG Hongfang, et.al., Effect of Light Transmission Characteristic of Scintillator on the Intrinsic Time Resolution of ETOF, High Energy Physics and Nuclear Physics, Vol.30,No.10 (2006)
5. LI Xin, SHAO Ming, LI Cheng, et.al, Correlation between Particle Ionization Energy Loss in MRPC and Its Signal Amplitude, High Energy Physics and Nuclear Physics, Vol.31,No.4 (2007)